UPDATED OPTICAL READ/WRITE MEMORY SYSTEM COMPONENTS

FINAL TECHNICAL REPORT

PREPARED FOR

GEORGE C. MARSHALL SPACE FLIGHT CENTER

MARSHALL SPACE FLIGHT CENTER, ALABAMA 35812

CONTRACT NO. NAS 8-26672

By

ELECTRO-OPTICS OPERATION

AUGUST 1973

UPDATED OPTICAL READ/WRITE MEMORY SYSTEM COMPONENTS

FINAL TECHNICAL REPORT

PREPARED FOR

GEORGE C. MARSHALL SPACE FLIGHT CENTER
MARSHALL SPACE FLIGHT CENTER, ALABAMA 35812

CONTRACT NO. NAS 8-26672

By

ELECTRO-OPTICS OPERATION

AUGUST 1973

i

FOREWORD

RADIATION

TABLE OF CONTENTS

RADIATION

A DIVISION OF HARRIS INTERTYPE CORPORATION

TABLE OF CONTENTS (Continued)

LIST OF ILLUSTRATIONS

RADIATION

A DIVISION OF HARRIS INTERTYPE CORPORATION

LIST OF ILLUSTRATIONS (Continued)

LIST OF ILLUSTRATIONS (Continued)

RADIATION
A DIVISION OF HARRIS INTERTYPE CORPORATION

LIST OF ILLUSTRATIONS (Continued)

SECTION I

INTRODUCTION AND SUMMARY

1.1 Objectives of the Contract

The Electro-Optics Center, under Contract NAS 8-26360, has designed and fabricated the optical components of a breadboard holographic read/write memory system and has specified the parameters of the major system components: 1) a laser system, 2) an x-y beam deflector, 3) a block data composer, 4) the read/write memory material, 5) an output detector array, and 6) the electronics to drive, synchronize, and control all system components.

Under Contract NAS 8-26672 we supplied and fabricated major components according to the previously established specifications, prepared computer programs to simulate the entire holographic memory system so that a designer can balance the requirements on the various components, and conducted a development program to optimize the combined recording and reconstruction process of the high density holographic memory system.

Under the present phase of Contract NAS 8-26672 we have fabricated an updated block data composer and holographic storage array. These devices have increased performance parameters and are adaptable to the existing testbed system. We have also investigated system configuration that will increase the memory capacity.

1.2 Summary of the Work Performed During the Contract

During this Contract we performed analyses of several optical system configurations that will increase the memory capacity without increasing the optical complexity. We studied one, two, and three-lens optical systems and found that the two and three-lens Gaussian systems gave the largest capacity combined with system compactness. The three-lens solution is useful when magnification is required to match the block data composer geometry to that of the photodetector array.

No significant reduction in optical complexity was found, however, From a Gaussian design viewpoint, the aperture ratios of the lenses still are the most significant parameter that influences the memory capacity. As the number of lenses increase, some reduction in the aperture ratio of each lens can be obtained, but this is equivalent to distributing the power of a single lens along the axis.

After the Gaussian design, we did a ray-trace analysis of specific optical systems. A controlled-aberration design was completed for a 0.25 (10^8) bit capacity memory, including a tool-fitting analysis and tolerance data. This design activity, along with the Gaussian system considerations, is reported in Section 2.

We have solved many of the fabrication problems associated with PLZT block data composers. We have fabricated several 32 x 32 element arrays and some 128 x 128 element arrays, using chrome-gold and indium tin oxide electrode structures. Breakage of the ceramics has been reduced to a minimum, but the performance of the devices still fall short of expectations. We believe the primary cause of poor performance in the quality of the PLZT ceramic wafers obtained from vendors. The results of our work on block data composers is summarized in Section 3.

In Section 4 we report our work on photoplastic arrays. We have fabricated a 20 strip array that is compatible with the 20 x 20 element lenslet array in the existing breadboard. Significant improvements have been made in charging techniques, heating and erasure times, lifetimes, signal-to-noise ratios and diffraction efficiency.

We also fabricated a holographic optical element in a thick material to demonstrate the feasibility of the technique. This element was designed to replace the 20 x 20 element lenslet array; it cannot be used in the present breadboard, however, because the offset angles are not corrected for the shrinkage of the material. We also completed our modeling of thick materials for use in a general memory design program package. This activity is discussed in Section 5, together with a summary of the results of a thick materials program performed by Battelle Columbus.

SECTION II
SYSTEM CONSIDERATIONS
2.1 Introduction

Under Contract NAS8-26672, the Harris Electro-Optics Center of Radiation previously designed, fabricated and delivered a holographic memory system. The objectives of this contract were an improvement in the capacity and speed of the existing system as well as a study of alternative system configurations for increasing the holographic memory capacity to 10^8 bits fully populated.

We have also considered 10^8 to 10^{12} bit mass memory capacities during the study. The maximum capacity is ultimately dependent upon the memory plane area and the data bit density. As an interim system, prior to the refinement of thick phase memories, we have implemented these planar memories using thermoplastic materials. If we select an average data bit density for the memory material of 10^4 data bits/mm^2, a 10^{12} bit mass memory would require a planar storage area of 100 square meters. An area of this size could be configured as a large billboard, a cylinder, a disc or possibly a spool of 105 mm film having a 1000 meter length. Most of the configurations would be difficult to access, requiring a long access time. However, a 10^8 bit mass memory requires a planar storage area of 0.01 square meter which is only a factor of ten greater in area than the present planar arrays being fabricated. During the present contract, we have designed an optical system for a 0.25×10^8 bit memory on a 50 mm x 50 mm hologram plane. We could place four of the arrays adjacent to each other on a slide and mechanically index the system to a selected array. Microseconds access times can be designed within an array and milliseconds access time obtained between arrays.

The planar memory size, considering the complexity and access time, can be expected, therefore, to fall between 10^8 and 10^{12} bits; the system parameters being dependent upon the application. Considering these parameters, we investigated system components, including the lens system, the deflection system, and the photodetector array, which could be multiplexed to obtain the desired configurations and sizes. We considered alternative system

RADIATION

configurations which conform to the available BDC, PDA, and hologram array devices. We designed signal path optical configurations for the present test-bed devices, as well as for a 10^8 bit capacity system.

In the following section we first evaluate the parameter independence for imaging and nonimaging systems, evaluating the equations for magnification M, lens aperture ratio R, hologram size d, system capacity Q^2, and hologram packing density ρ. We examine configurations utilizing the present test-bed devices and calculate the lens requirements for typical systems, including 6.55×10^6, 10^8, and 0.25×10^8 bit capacities.

In the next section we describe and carry out the lens design for a 6.55×10^6 bit and a 0.25×10^8 bit memory. Following sections consider deflection systems, the photodetector arrays, and finally, modifications to the present breadboard.

2.2 Transform Optics

We re-examine optical configurations for obtaining the near Fourier block data composer transform at the hologram plane and the image of the reconstructed hologram at the photodetector plane. The analysis of two lens systems considered practical for the holographic memory system test-bed was reported previously by the Electro-Optics Center.[1] We determined that the two Fourier optical system configurations are compatible with the optical memory system test-bed and have considered these systems in greater detail. The configurations are shown in Figure 2-1. The first system (see Figure 2-1a) is a one-lens imaging system where a single lens forms the Fourier transform and also images the block data composer plane into the photodetector plane. The present optical system test-bed was fabricated using a special two-lens case of the imaging system (Figure 2-1b). The system is designed with infinite magnification and a second identical lens is added to the system to provide an overall magnification of unity. This special two-lens case allows smaller aperture lenses to be fabricated versus a larger single imaging lens configuration; however, it can be most easily designed for unity magnification.

TRANSFORM AND
IMAGING LENS

HOLOGRAM
ARRAY

BDC

PDA

A. SINGLE IMAGING LENS SYSTEM

TRANSFORM
LENS

HOLOGRAM
ARRAY

IMAGING
LENS

BDC

PDA

B. SINGLE IMAGING LENS SYSTEM FOR $M = -\infty$ AND $M_s = -1$

BDC TRANSFORM
LENS

HOLOGRAM
ARRAY

IMAGING
LENS

PDA

C. TWO IMAGING LENS SYSTEM

IMAGING
LENS

BDC TRANSFORM
LENS

HOLOGRAM
ARRAY

IMAGING
LENS

PDA

D. TWO IMAGING LENS SYSTEM FOR $M = -\infty$ $M_s = -1$
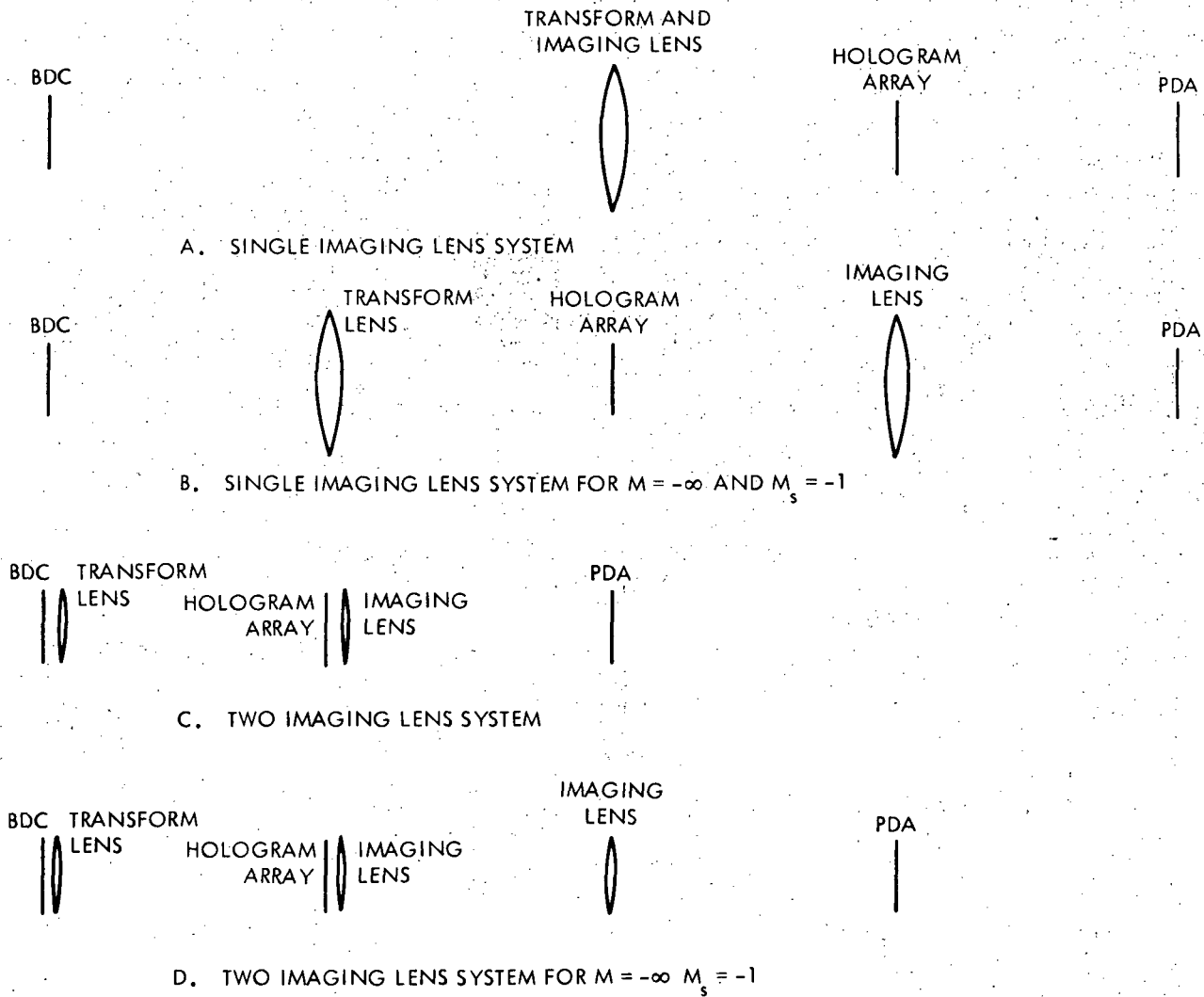
Figure 2-1. Signal Optics Configurations

RADIATION

The second system, a nonimaging system with respect to the transform lens, is a two-lens imaging system with a block data composer placed in contact with the transform lens (Figure 2-1c). The second lens, in contact with the hologram array, images the reconstructed holograms into the photodetector plane. A special three-lens case exists for this configuration (Figure 2-1d) where the front lens system is designed for a magnification of infinity and a third lens is added to provide an overall magnification of unity. The three lenses can be made identical with the same focal length and aperture.

The one-lens system has an advantage over the two-lens system when considering the lens design and fabrication required. The special two-lens, unity magnification system used on the present test-bed also has an advantage when we consider that the lens design and test plate fabrication are identical for both.

The two-lens optic system requires smaller aperture lenses for the same system data capacity which offsets the two different lens designs and fabrication complexity, particularly for large lens designs. The special three-lens, unity magnification system also has the advantage of a single lens design.

2.2.1 <u>Single Lens Imaging System Derivation.</u> - The analysis of the capacity of the single lens imaging system follows and is referenced to Figure 2-2.

a. We first calculate the magnification, M, of the system

$$M = \frac{-\left(\ell_2 - \frac{1}{K}\right)}{\frac{1}{K}}$$

$$\ell_2 = \frac{1 - M}{K} \tag{1}$$

where M = magnification

ℓ_2 = lens to image distance

K = power of lens
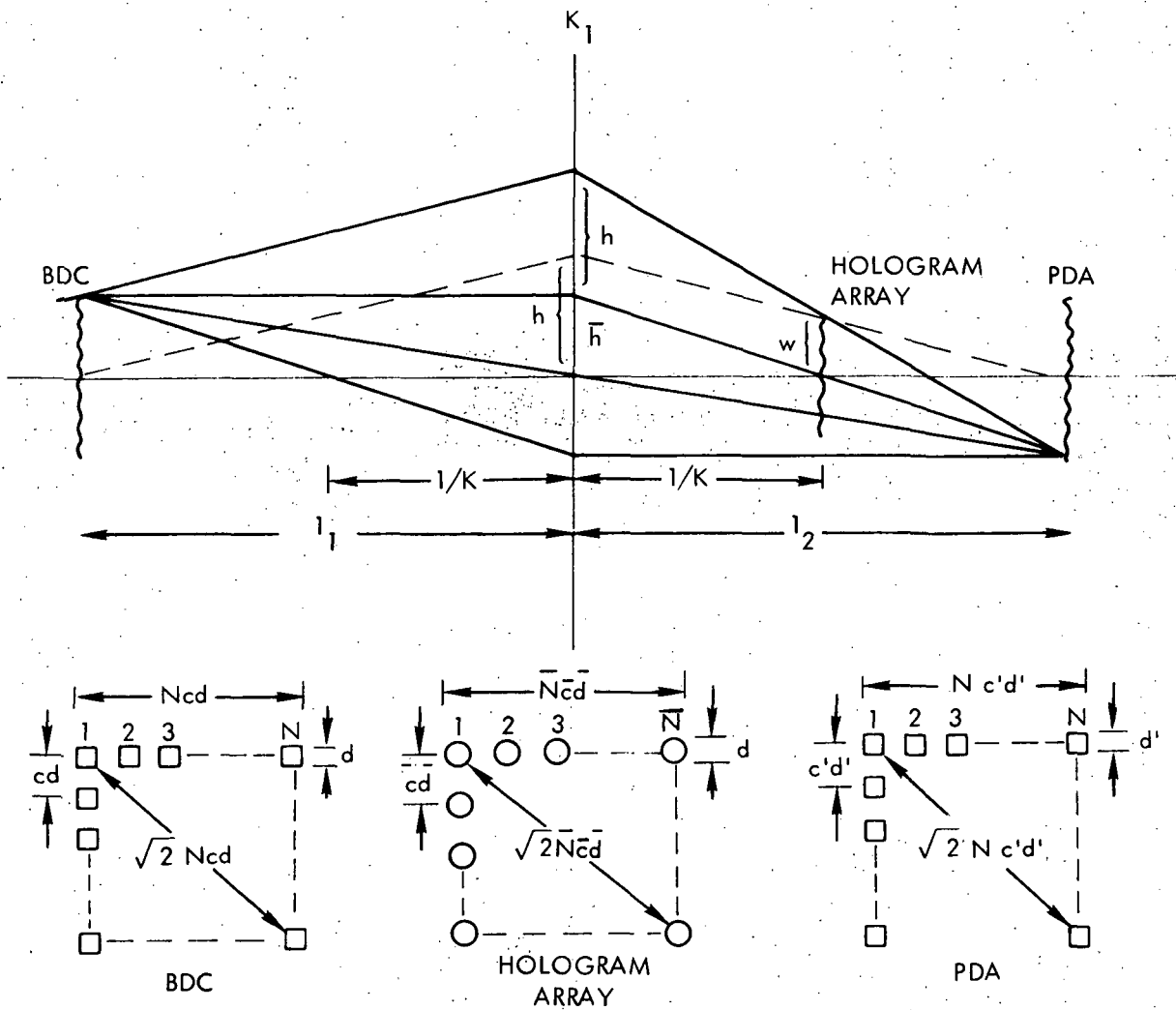
Figure 2-2. Single Imaging Lens System

RADIATION
A DIVISION OF HARRIS INTERTYPE CORPORATION

$$M = - \frac{\frac{1}{K}}{\left(\ell_1 - \frac{1}{K}\right)}$$

$$\ell_1 = \frac{M-1}{MK} \tag{2}$$

where ℓ_1 = object to lens distance.

b. The lens aperture ratio, R, is determined by the diagonal of the block data composer and is given by,

$$R = 2\sqrt{2}\,[|h| + |\bar{h}|]\,K \tag{3}$$

where R = aperture ratio lens

h = intersection principle marginal ray at lens

$\bar{h}$ = intersection principle pupil ray at lens

$$\bar{h} = \frac{cdN}{2} \tag{4}$$

where 2h = width of the BDC

c = bit spacing/bit diameter for the BDC

d = bit diameter for the BDC

N = bits/row in BDC

$$\omega = \frac{\bar{c}\bar{d}\bar{N}}{2} \tag{5}$$

where 2ω = width of the hologram array

$\bar{c}$ = hologram spacing/hologram diameter

$\bar{d}$ = hologram diameter

$\bar{N}$ = holograms/row

From Figure 2.2 we obtain

$$h = \frac{\omega \ell_2}{\ell_2 - \frac{1}{K}} \tag{6}$$

Upon substituting (1) and (5) into (6), we obtain

$$h = \frac{-\overline{cdN}\,(1 - M)}{2M}$$

(7)

Finally, substituting (4) and (7) into (3), we find

$$R = \sqrt{2}\,K\left[\overline{cdN}\left(\frac{1 - M}{M}\right) + cdN\right]$$

(8)

c. The hologram size, $\overline{d}$, is defined as the main lobe width of the Fraunhofer diffraction pattern for a square aperture of cd on a side, and is given as,

$$\overline{d} = \frac{2\lambda}{cdK}$$

(9)

(Note: This is the definition of double Rayleigh Resolution)
where λ is the wavelength of the illumination.

d. The one-dimensional system data capacity, Q, is given by

$$Q = N\overline{N},$$

(10)

where Q is the one-dimensional system data capacity.

Combining (8) and (10), we obtain

$$Q = N\left(\frac{R}{\sqrt{2}K} - cdN\right)\left(\frac{M}{1 - M}\right)\left(\frac{1}{\overline{cd}}\right)$$

(11)

To maximize the system capacity we find

$$\frac{\partial Q}{\partial N} = \left(\frac{M}{1 - M}\right)\left(\frac{1}{\overline{cd}}\right)\left(\frac{R}{\sqrt{2}K} - 2\,cdN\right)$$

(12)

We determine the maximum capacity with respect to N by letting

$$\frac{\partial Q}{\partial N} = 0$$

(13)

we obtain, by combining (12) and (13), the N associated with a maximum capacity system of

$$N = \frac{R}{2\sqrt{2}\,cdK.}$$

(14)

By substituting (9) and (14) into (11), we obtain

$$Q_{max_{(N)}} = \frac{R^2}{16\,\lambda\,\bar{e}K}\left|\frac{M}{1-M}\right|$$ (15)

e. The hologram data density, ρ , is determined from Figure 2-3 as

$$\rho = \frac{N}{d}$$ (16)

By combining (9) and (14) into (16), we determine

$$\rho = \frac{R}{4\sqrt{2}\lambda}$$ (17)

f. For the maximum capacity system design we will show that the lens aperture is twice the diagonal of the block data composer. Upon combining (4) and (7), we have

$$\left|\frac{\bar{h}}{h}\right| = \frac{cdN}{\overline{cdN}}\left|\frac{M}{1-M}\right|$$ (18)

By substituting (10) into (18), we get

$$\left|\frac{\bar{h}}{h}\right| = \frac{cdN^2}{\overline{cd}Q}\cdot\left|\frac{M}{1-M}\right|,$$ (19)

and by substituting (14), (15), and (9) into (19), we get for $Q_{max_{(N)}}$

$$\left|\bar{h}\right| = \left|h\right|$$ (20)

$$\therefore \frac{cdN}{2} = \frac{\overline{cdN}}{2}\left|\frac{1-M}{M}\right| \text{ for max } Q$$

max Q also occurs for $M = \infty$

$$\therefore cdN = \overline{cdN} \text{ for max } Q.$$
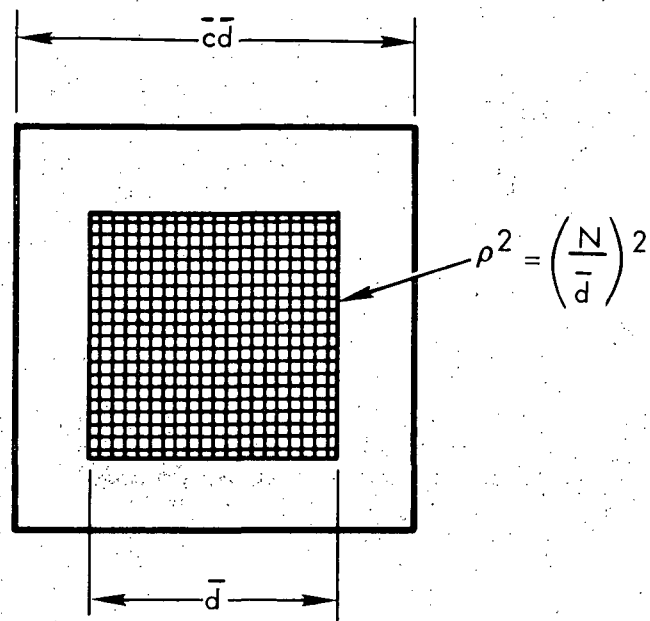
Figure 2-3. Hologram Packing Density

$$\rho^2 = \left(\frac{N}{\bar{d}}\right)^2$$
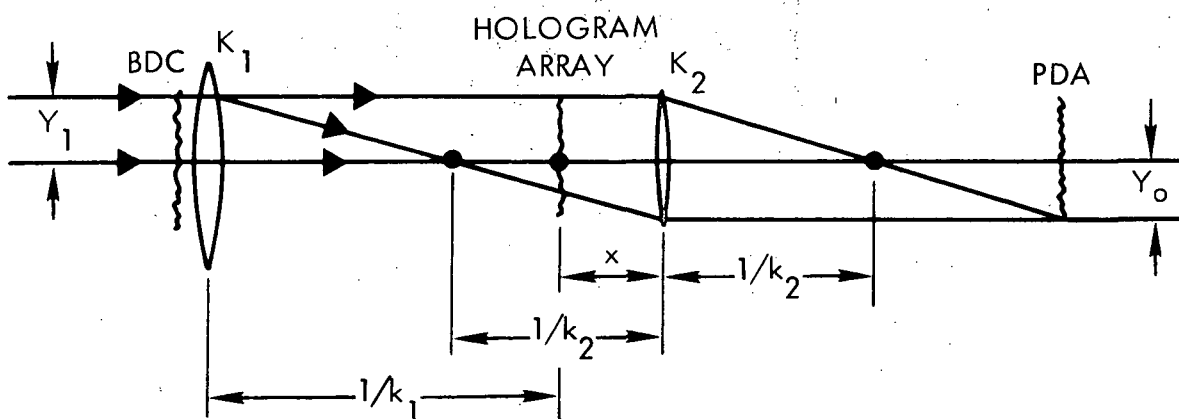
Figure 2-4. Two Imaging Lens System

RADIATION
A DIVISION OF HARRIS INTERTYPE CORPORATION

Finally, combining (4) and (20) into (3), we have for $Q_{max_{(N)}}$

$$R = 2\sqrt{2}\,cdNK \qquad\qquad (21)$$

$$\text{also } R = 2\sqrt{2}\,\overline{cdN}K \left| \frac{1-M}{M} \right|$$

$$D = 2\sqrt{2}\,cdN \text{ lens aperture}$$

for $Q_{max_{(N+M)}}$

$$cdN = \overline{cdN}$$

$$Q_{max_{(N+M)}} = \frac{R^2}{16\lambda \bar{c}K}$$

We summarize the system equations derived for the single lens imaging system in Table 2-1.

2.2.2   Two Lens Imaging Systems Derivation. - We next analyze the capacity of the two-lens imaging system.   The system is shown in Figure 2-4.

a.   We first calculate the magnification, M, of the system.

$$M = \frac{-Y_o}{Y_I}$$

where M is the magnification, $2Y_o$ is the object width, and $2Y_I$ is the image width, so that

$$M = -\frac{\dfrac{1}{K_2}}{\dfrac{1}{K_1} - \dfrac{1}{K_2} + x}$$

where K_1 is the power of the first lens, K_2 is the power of the second lens, and x is the distance from the hologram array to the second lens.

TABLE 2-1

Single Lens Imaging

$$\rho = \frac{R}{4\sqrt{2}\lambda}$$

$$K = \frac{R}{2\sqrt{2}\,Ncd}$$

$$\bar{d} = \frac{2\lambda}{cd\bar{K}}$$

$$\bar{N} = \frac{Q}{N}$$

$$Q_{maxN} = \frac{R^2}{16\lambda\bar{c}\bar{K}}\left(\frac{M}{1-M}\right)$$

$$Q = \frac{N}{\bar{cd}}\left(\frac{R}{\sqrt{2\bar{K}}} - cdN\right)\left(\frac{M}{1-M}\right)$$

$$\text{for } Ncd = \overline{Ncd}\left(\frac{1-M}{M}\right)$$

$$Q_{max\,(N\&M)} = \frac{R^2}{16\lambda\bar{c}\bar{K}}$$

$$\text{for } Ncd = \overline{Ncd} \text{ and } M = -\infty$$

Two Lens Imaging

$$\rho = \frac{R_1}{2\sqrt{2}\lambda}$$

$$K_1 = \frac{R_1}{\sqrt{2}\,Ncd}$$

$$K_2 = \left(\frac{M-1}{M}\right)K_1$$

$$\text{also, } K_2 = \frac{R_2}{2\,\overline{Ncd}}$$

$$\bar{d} = \frac{2\lambda}{cd\bar{K_1}}$$

$$Q = \frac{R_1 R_2}{4\lambda\bar{c}\,K_2}, \text{ for } Q_{max}\; R_1 = R_2$$

$$\bar{N} = \frac{Q}{N}$$

$$D_1 = \frac{R_1}{K_1} = \sqrt{2}\,Ncd$$

RADIATION
A DIVISION OF HARRIS INTERTYPE CORPORATION

If we place the hologram array in the plane of lens K_2, then $x = 0$ and we obtain,

$$\frac{K_2}{K_1} = \left| \frac{M-1}{M} \right|.$$ (22)

b. The lens aperture ratio, R_1, is determined by

$$D_1 = \sqrt{2}\ cdN,$$

where D_1 is the aperture of the first lens and cdN is the width of the block data composer so that

$$R_1 = \sqrt{2}\ cdNK_1.$$ (23)

c. The lens aperture ratio, R_2, is determined by,

$$D_2 = \sqrt{2}\ \overline{cdN}$$

where D_2 = aperture of the second lens, and $\overline{cdN}$ = width hologram array so that

$$R_2 = 2\ \overline{cdN}\ K_2$$ (24)

d. The hologram size, $\bar{d}$, is defined as the main lobe width of the Fraunhofer diffraction pattern for a square aperture of cd on a side and is given by

$$\bar{d} = \frac{2\lambda}{cdK_1}$$ (25)

where λ = wavelength of the illumination.

e. The one-dimensional system data capacity, Q, is given by

$$Q = N\overline{N}$$ (26)

By substituting (23), (24), and (25) into (26), we obtain

$$Q = \frac{R_1 R_2}{4\lambda\bar{c}K_2}$$ (27)

f.   We next derive the maximum capacity, Q_M, of the system with respect to N and show the aperture ratio of the two lenses are equal for maximum capacity. By combining (23) and (24), we obtain

$$R_1 + R_2 = \sqrt{2}\,cdNK_1 + \sqrt{2}\,\overline{cd}\overline{N}K_2$$

by substituting (25) and (26), we derive

$$Q = \frac{[R_1 + R_2 - \sqrt{2}\,cdNK_1]\,cdNK_1}{2\sqrt{2}\,\bar{c}\,K_2} \tag{28}$$

To maximize the system capacity we find

$$\frac{\partial Q}{\partial N} = \frac{[R_1 + R_2]\,cdK_1}{2\sqrt{2}\,\bar{c}\lambda K_2} - \frac{\sqrt{2}\,c^2 d^2 K_1^{\,2} N}{\sqrt{2}\,\lambda\bar{c}K_2}$$

We determine the maximum capacity, Q_M, with respect to N by letting

$$\frac{\partial Q}{\partial N} = 0$$

and we obtain

$$R_1 + R_2 = 2\sqrt{2}\,cdK_1 N \tag{29}$$

Substituting (28) into (29) we have

$$Q_{max} = \frac{(R_1 + R_2)^2}{16\lambda\,\bar{c}K_2} \tag{30}$$

also, we know that to make $Q = Q_{max}$, we must have that

$$\frac{R_1 R_2}{4\lambda\bar{c}K_2} = \frac{(R_1 + R_2)^2}{16\lambda\bar{c}K_2}$$

RADIATION

A DIVISION OF HARRIS INTERTYPE CORPORATION

or

$$(R_1 + R_2)^2 = 4R_1 R_2$$

$$(R_1 - R_2)^2 = 0$$

$$R_1 = R_2 \tag{31}$$

We conclude that for maximum capacity that the aperture ratios are equal. Finally, from (31) and (30), we find that

$$Q_{max} = \frac{R_1^{\,2}}{4\lambda c K_2} . \tag{32}$$

g. The hologram data packing density, ρ, is determined from Figure 2-3 as

$$\rho = \frac{N}{d}$$

By combining (25) and (29), we determine

$$\rho = \frac{R_1}{2\sqrt{2}\,\lambda} \tag{33}$$

We summarize the system equations derived for the two lens imaging system in Table 2-1.

2.2.3 <u>Optical System Comparisons Utilizing Present Devices.</u> - We have derived sets of equations (see Table 2-1) to describe the parameter relationships of the two optic systems. Each parameter has certain physical constraints which must be considered for a practical design. We will consider examples utilizing the present BDC, hologram array and PDA designs of the present test-bed system and the lenses required for optimizing the system. Two configurations are considered for each of the two optic systems, a direct magnification of minus one and the use of an auxilliary lens to convert a magnification of minus infinity to a system magnification of minus one.

Single Lens Case $M = -\infty$ With Second Lens for $M_s = -1$. - We first consider a single

lens imaging configuration with a magnification of minus infinity. We add an auxiliary

lens identical in design to the transform lens to provide a system magnification of minus one.

a. The data bit storage density is limited by the hologram storage material. A

density of $\rho^2 \leq 2.25 \times 10^6$ bits/cm^2 is practical for thermoplastics. We require

that,

$$\rho \leq 150 \text{ bits/mm}$$

for the single lens imaging system

$$\rho = \frac{R}{4\sqrt{2}\,\lambda}$$

$$\therefore \frac{R}{4\sqrt{2}\,\lambda} \leq 150 \text{ bits/mm}$$

where λ = wavelength in μm

$$R \leq .846 \times 10^6 \lambda$$

for $\lambda = .6471$ μm, krypton line

$$R \leq .55$$

for $\lambda = .6328$ μm, He-Ne line

$$R \leq .54$$

for $\lambda = .488$ μm, argon line

$$R \leq .42$$

If we examine the equation for $Q_{max} = \frac{R^2}{16\lambda cK} \left| \frac{M}{1-M} \right|$, we observe that

R should be as large as practical to maximize Q.

We conclude that a lens aperture ratio of R = .5 satisfies the storage density

equation for the krypton and He-Ne lines but may be borderline for the argon

line.

b. The focal length of the lens, with R now fixed, will be determined by the width
of the block data composer, Ncd, and the magnification of the single lens con-
figuration, M. The block data composer designed for the present test-bed is
32.5 mm wide. We select a single lens magnification of $M = -\infty$. The photo-
detector array layout is identical to the block data composer, i.e., $N = N'$,
$d = d'$, and $c = c'$. We image the BDC onto the PDA through a system magnifica-
tion of one. A system magnification of $M_S = -1$ is obtained as previously noted
by adding a second identical lens.

The lens power is given by

$$K = \frac{R}{2\sqrt{2}\,Ncd}$$

Let R = .5

Ncd = 32.5 mm width BDC

$$\therefore \quad K = \frac{.5}{2\sqrt{2} \times 32.5 \text{ mm}}$$

$$= \frac{1}{184 \text{ mm}} \quad \text{lens power}$$

Also, we determine the lens diameter from

$$D = \frac{R}{K}$$

$$D = .5 \times 184 \text{ mm}$$

$$= 92 \text{ mm diameter lens}$$

c. We next calculate the hologram diameter, $\bar{d}$, which is inversely proportional to
the input data bit spacing, cd. We select N at this time having fixed the block
data composer width, Ncd, in the previous step. The present system is designed
for N = 128, therefore, the data bit spacing is:

$$cd = \frac{32.5 \text{ mm}}{128}$$

$$= .254 \text{ mm}$$

We are now free to choose the bit spacing ratio, c. For the present BDC we have selected c = 1.5, therefore d = .169 mm.

We now calculate the hologram diameter from,

$$\bar{d} = \frac{2\lambda}{cdK}$$

Let $\lambda = .6328$ m

$K = 1/184$ mm

$$\bar{d} = \frac{2 \times .6328 \times 10^{-6} \times 184 \times 10^{-3}}{.254 \times 10^{-3}}$$

$$= .915 \text{ mm}$$

d. We now choose the hologram spacing ratio, $\bar{c}$. In the present system we have selected $\bar{c} = 1.64$ which provides a hologram spacing, $\bar{c}\bar{d}$, of 1.5 mm.

e. The system capacity can now be determined and is calculated from

$$Q_{max} = \frac{R^2}{16\lambda\bar{c}K} \left| \frac{M}{1-M} \right|$$

Let $R = .5$

$\lambda = .6328$ μm

$\bar{c} = 1.64$

$M = -\infty$

$$Q_{max} = 2.76 \times 10^{-3} \text{ bits}$$

f. We calculate the holograms required per row to obtain the system capacity from,

$$\overline{N} = \frac{Q}{N}$$

$$= \frac{2.76 \times 10^{-3}}{128}$$

$$= 20.8$$

We let $\overline{N} = 20$ the next lowest integer which will slightly modify the maximum capacity calculated in step e.

$$Q = 20 \times 128$$

$$= 2.56 \times 10^3 \text{ bits}$$

and the total two dimensional system capacity is,

$$Q^2 = 6.55 \times 10^{-6} \text{ bits}$$

Two Lens Case, m = -1. - We consider next a double lens imaging configuration with a direct magnification of minus one.

a. The data bit storage density is limited by the hologram storage material as in the previous case but the system cannot support as large an aperture ratio for the transform lens. We require the hologram density, ρ, to be

$$\rho \leq 150 \text{ bits/mm}$$

The relationship for the two lens case is

$$\rho = \frac{R_1}{2\sqrt{2}\lambda}$$

where λ = wavelength in μm.

$$R_1 \leq .423 \times 10^6 \lambda$$

for $\lambda = .6471$ μm, the krypton line, we find

$$R_1 \leq .274$$

for $\lambda = .6328$ μm, the He-Ne line, we find

$$R_1 \leq .266$$

for $\lambda = .488$ μm, the argon line, we find

$$R_1 \leq .21$$

We examine the equation for $Q = R_1 R_2/4\lambda \bar{c} K_2$ and observe that R_1 should be as large as practical to maximize Q. We therefore select the lens aperture ratio, $R_1 = .25$ as satisfying the Krypton and He-Ne wavelength relationship.

b. The focal length of the transform lens, with R_1 selected, is now determined by the size of the block data composer.

$$K_1 = \frac{R_1}{\sqrt{2}\,Ncd}$$

$R_1 = .25$ and a block data composer width, Ncd, of 32.5 mm, we find

$$K_1 = \frac{.25}{\sqrt{2}\,32.5\text{ mm}}$$

$$= \frac{1}{184\text{ mm}} \quad \text{lens power}$$

also, we determine the lens diameter from

$$D_1 = \frac{R_1}{K_1}$$

$$= .25 \times 184$$

$$= 46\text{ mm diameter lens}$$

RADIATION
A DIVISION OF HARRIS INTERTYPE CORPORATION

c. The hologram diameter, $\overline{d}$, is calculated next. The solution is identical to the single lens case. Therefore, an identical calculation for the two lens system yields for the input data bit spacing, cd, and the hologram diameter $\overline{d}$

$$cd = .254 \text{ mm}$$

$$\overline{d} = .915 \text{ mm}$$

d. We now select the hologram spacing ratio, $\overline{c}$, which in the present system is

$$\overline{c} = 1.64$$

e. For the two lens imaging configuration the second lens diameter is also a factor in determining the system capacity. The ratio of the lens power is determined by the system magnification desired. For the present system we calculate,

$$K_2 = \left| \frac{M-1}{M} \right| K_1$$

let M = -1

$$\therefore K_2 = 2K_1$$

$$= \frac{1}{92} \text{ mm lens power}$$

f. The system capacity can now be determined. We maximize Q by choosing the largest practical lens aperture ratio for R_2.

$$Q = \frac{R_1 R_2}{4 \lambda \overline{c} K_2}$$

let $R_1 = .25$

$$R_2 = .5$$

$$\lambda = .6328 \text{ μm}$$

$$\bar{c} = 1.64$$

$$K_2 = 1/92 \text{ mm}$$

$$Q = 2.76 \times 10^3 \text{ bits}$$

g. We calculate the holograms required per row to obtain the system capacity from,

$$\bar{N} = \frac{Q}{N}$$

$$= \frac{2.76 \times 10^3}{128}$$

$$= 20.8$$

We let $\bar{N} = 20$ the next lowest integer which decreases the system capacity slightly from the maximum calculated in Step f. For system capacity we now have

$$Q = 20 \times 128$$

$$= 2.56 \times 10^3 \text{ bits}$$

and the total two-dimensional system capacity is,

$$Q^2 = 6.55 \times 10^6 \text{ bits}$$

<u>Two-Lens Case, $M = -\infty$, With Third Lens for $M_s = -1$.</u> – A similar special case exists for the two-lens system where the two-lens magnification is designed to be minus infinity, $M = -\infty$, and a third auxiliary lens is used to produce an overall system magnification of minus one, $M_s = -1$. The calculations are identical to the $M = -1$ case except for the second lens parameters and the system capacity calculation which now become

$$K_2 = \left| \frac{M-1}{M} \right| K_1$$

let $M = -\infty$

$$K_2 = K_1$$

$$K_2 = \frac{1}{184 \text{ mm}} \text{ lens power}$$

RADIATION

A DIVISION OF HARRIS INTERTYPE CORPORATION

We set the system capacity identical to the previous calculation, i.e., $Q = 2.76 \times 10^3$ bits, by preserving the ratio R_2/K_2 in the calculation.

$$Q = \frac{R_1 R_2}{4\lambda \bar{c} K_2}$$

In the previous calculation $R_2 = .5$ and $K_2 = 1/92$ mm, now $K_2 = 1/184$ mm so we let $R_2 = .25$. The second lens now becomes identical to the first lens. Finally, a third identical lens is required to convert the $M = -\infty$ of the first pair to a $M_s = -1$ for the system. The three lenses are, therefore, identical, a lens design advantage.

We note that selecting R_2 to be .5 doubles the system capacity. This solution is not compatible as it requires an increase in the hologram array width to match the larger lens diameter, D_2, along with an increase in the signal beam deflection angles.

Single Lens Case, M = -1. - We can carry out a system design for the one-lens configuration using a magnification of $M = -1$ which would require the use of only one lens. For $M = -1$ we must satisfy $Ncd = \overline{Ncd} \left| \frac{1 - M}{M} \right|$, therefore, the hologram array size would be 1/2 of the BDC size. The calculation shows the lens has a focal length of 368 mm and a hologram diameter, $\bar{d}$, of 1.83 mm. The present hologram array is designed with a $\overline{cd}$ of 1.5 mm. If we desire to remain compatible with this array, $\bar{c}$ must be ≤ 1 mm. Therefore, the single lens configuration does not have a compatible solution for the present test-bed system devices.

Summary. - We have considered four configurations for an optical system utilizing the present test-bed devices. We summarize the results below.

For the parameters

$$\left. \begin{array}{l} \rho = 150 \text{ bits/mm} \\ c = c' = 1.5 \\ d = d' = .169 \text{ mm} \\ N = N' = 128 \end{array} \right\} \quad Ncd = N'c'd' = 32.5 \text{ mm}$$

$$\left. \begin{array}{l} \bar{c} = 1.64 \\ \bar{d} = .915 \text{ mm} \\ \bar{N} = 20 \end{array} \right\} \quad \overline{Ncd} = 30 \text{ mm}$$

$$Q^2 = 6.55 \times 10^6 \text{ bits}$$

$$M_s = -1$$

The following lenses are required:

System	M	M_s	First Lens Transform	Second Lens Imaging	Third Lens Imaging
Single Lens	-1	-1	Solution not Compatible	-	-
Single Lens	-∞	-1	FL = 184 mm Diam. = 92 mm	FL = 184 mm Diam. = 92 mm	-
Double Lens	-1	-1	FL = 184 mm Diam. = 46 mm	FL = 92 mm Diam. = 46 mm	-
Double Lens	-∞	-1	FL = 184 mm Diam. = 46 mm	FL = 184 mm Diam. = 46 mm	FL = 184 mm Diam. = 46 mm

The three acceptable system designs are shown in Figure 2-5. The second system requires smaller diameter lenses with half the system length. The lens pair is not identical but we expect the designing and fabricating of two small lenses is less difficult than a single lens of twice the diameter. The third system requires three identical lenses of the smaller diameter.

2.2.4 10^8 System Capacity, Two Imaging Lens Design. – We developed several sets of lenses and device parameters for a two-imaging lens system design with a system capacity, Q^2 of 10^8. We anticipate from the following Gaussian optics design that a large lens system will be required. The previous section derives the basic equations which are referred to in the following calculations.

a. Size of the hologram array. The data packing density is given by

$$\rho \geq \frac{R_1}{2\sqrt{2}\lambda} \qquad (34)$$

$$R_1 \leq 2\sqrt{2}\lambda\rho \qquad (35)$$

Figure 2-5. Optical Systems
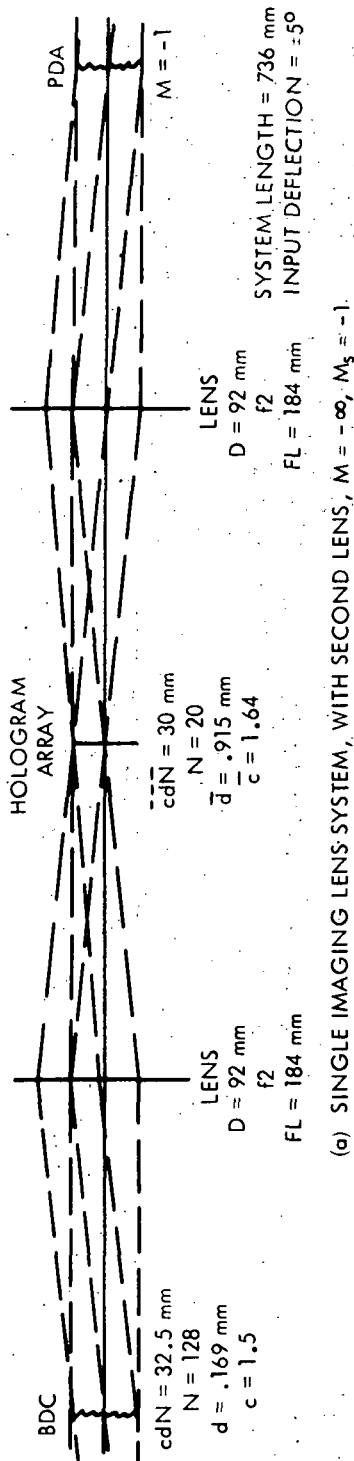
(a) SINGLE IMAGING LENS SYSTEM, WITH SECOND LENS, $M = -\infty$, $M_s = -1$
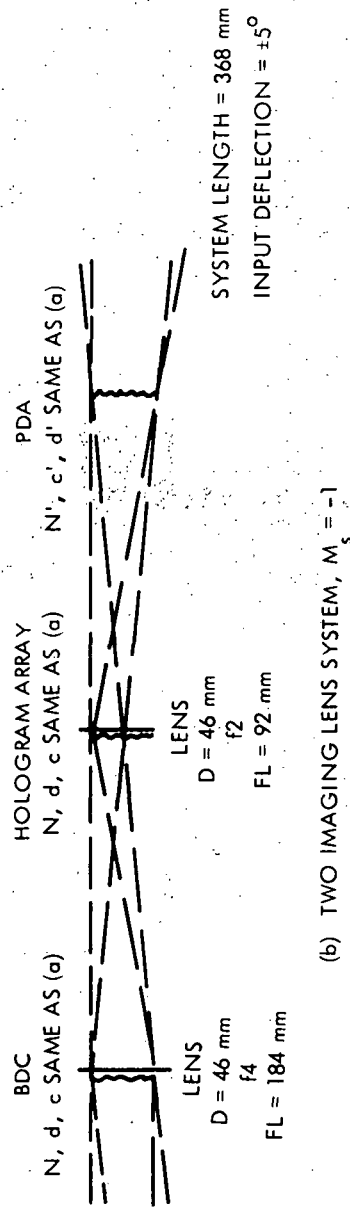
(b) TWO IMAGING LENS SYSTEM, $M_s = -1$
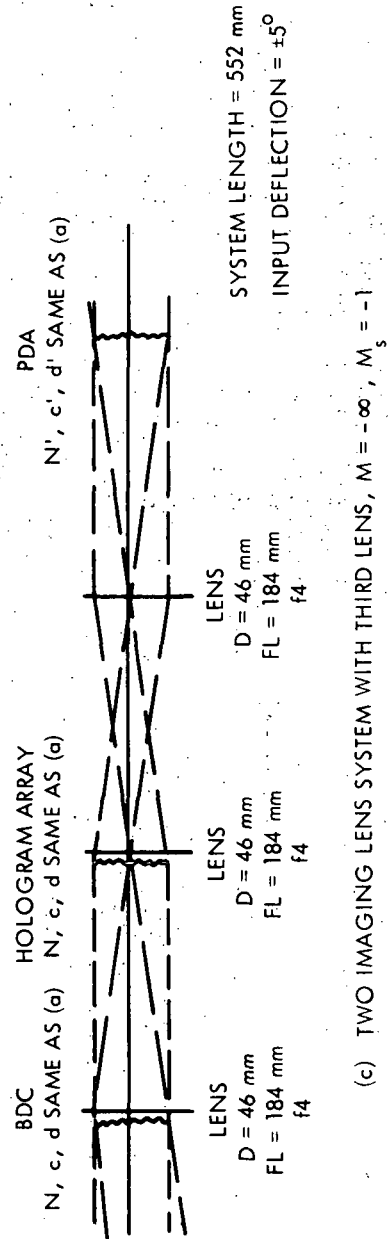
(c) TWO IMAGING LENS SYSTEM WITH THIRD LENS, $M = -\infty$, $M_s = -1$

The system capacity, Q, is given by

$$Q = \frac{R_1 R_2}{4 \lambda \bar{c} K_2} \tag{36}$$

$$\frac{R_2}{K_2} = \frac{4Q\lambda\bar{c}}{R_1} \tag{37}$$

The hologram array width, $\overline{Ncd}$, is given by

$$\overline{Ncd} = \frac{D_2}{\sqrt{2}} \tag{38}$$

and

$$\overline{Ncd} = \frac{R_2}{\sqrt{2}\,K_2} \tag{39}$$

Combining (35), (37), and (39) we obtain

$$\overline{Ncd} = \frac{Q\bar{c}}{\rho} \tag{40}$$

The one-dimensional system capacity, Q, has been chosen as 10^4 bits, the maximum data packing density, ρ, is 150 bits/mm and the hologram spacing ratio $\bar{c}$, will be approximately 1.5, we then find

$$\overline{Ncd} = \frac{10^4 \times 1.5}{150 \times 10^{-3}}$$

$$\overline{Ncd} = 100 \text{ mm}$$

b. Bits/Row in the block data composer. The hologram size, $\bar{d}$ is defined by

$$\bar{d} = \frac{2}{cdK_1} \tag{41}$$

$$K_1 = \frac{2\lambda}{cd\bar{d}} \tag{42}$$

RADIATION

A DIVISION OF HARRIS INTERTYPE CORPORATION

The block data composer width, Ncd, is given by

$$Ncd = \frac{D_1}{\sqrt{2}}$$ (43)

$$Ncd = \frac{R_1}{\sqrt{2}K_1}$$ (44)

Combining (34), (41), and (43) we have

$$Ncd = \rho cd\bar{d}$$ (45)

$$N = \rho\bar{d}$$ (46)

We note that selection of the hologram size will now determine the bits/row in the block data composer. We select $\bar{d}$ to be approximately .5 to 1 mm, a reasonable size for reconstruction. We select $\bar{d}$ to be .96 mm and obtain

$$N = 150 \times 10^3 \times .96 \times 10^{-3}$$

$$N = 144$$

c. Bits/Row in the hologram array. We determine $\bar{N}$ from the system capacity and the bits/row in the BDC and select the next highest integer.

$$\bar{N} = \frac{Q}{N}$$ (47)

$$= \frac{10^4}{144}$$

$$\bar{N} \cong 70$$

d. Lens parameters. From (35), assuming $\lambda = .5145$ µm, we determine

$$R_1 \leq 2\sqrt{2} \times .5145 \times 10^{-6} \times 150 \times 10^3$$

$$R_1 \leq .2$$

Rearranging (38), we obtain

$$D_2 = \sqrt{2}\ \overline{Ncd} \tag{48}$$

and we find

$$D_2 = \sqrt{2}\ 100\ mm$$

$$= 141\ mm$$

also

$$\frac{R_2}{K_2} = \sqrt{2}\ \overline{Ncd} \tag{49}$$

$$\frac{R_2}{K_2} = 141\ mm$$

We can now select constant ratios of R_2 and K_2, i.e.,

$$R_2 = .5\ \text{for}\ K_2 = 1/282\ mm$$

$$R_2 = .25\ \text{for}\ K_2 = 1/564\ mm$$

$$R_2 = .125\ \text{for}\ K_2 = 1/1128\ mm$$

We consider an R_2 equal to or smaller than .5, for lens design convenience and a K_2 equal to or larger than 1/1128 mm, for convenience in physical system length.

The ratio of the power of the two lenses is given as

$$\frac{K_1}{K_2} = \left| \frac{M}{M-1} \right| \tag{50}$$

Combining (44) and (50) we obtain

$$Ncd = \frac{R_1}{\sqrt{2}\ K_2} \left| \frac{M-1}{M} \right| \tag{51}$$

We can now select a system magnification M to satisfy $M = c'd'/cd$. We table several combinations of parameters determined by (49), (50) and (51).

| Set* | $D_2 = 141$ mm | | M | M_s | $R_1 = .2$ | | |
	R_2	$1/K_2$ mm			$1/K_1$ mm	D_1 mm	Ncd mm
a.	.5	282	$-\infty$	-1 ⎫ 3rd	282	56.4	40
	.25	564	$-\infty$	-1 ⎪ lens reqd	564	112.8	80
c.	.2	705	$-\infty$	-1 ⎬ $D_3 = D_2$	705	141.0	100
	.125	1128	$-\infty$	-1 ⎭ $K_3 = K_2$	1128	225.6	160
b.	.5	282	-1	-1	564	112.8	80
	.25	564	-1	-1	1128	225.6	160
	.5	282	$-1/4$	$-1/4$	1110	222.0	157

* We complete the design by selecting several sets of systems as follows:

a. The smallest BDC is required by the following 3-lens system:

$$Q = 10^4$$
$$N = 144$$
$$\bar{N} = 70$$
$$\overline{Ncd} = 100 \text{ mm}, \quad \bar{d} = .96 \text{ mm}, \quad \bar{c} = 1.5$$
$$Ncd = 40 \text{ mm}, \quad d = .185 \text{ mm}, \quad c = 1.5$$
$$M_s = -1$$

Lens 1; 56.4 mm diam., 282 mm f.1.

Lens 2 and 3; 141 mm diam., 282 mm f.1.

b. The smallest BDC for a 2-lens design is:

$$Q = 10^4$$

$$N = 144$$

$$\bar{N} = 70$$

$$\overline{Ncd} = 100 \text{ mm}, \quad \bar{d} = .96 \text{ mm}, \quad \bar{c} = 1.5$$

$$Ncd = 80 \text{ mm}, \quad d = .37 \text{ mm}, \quad c = 1.5$$

$$M_s = -1$$

Lens 1; 112.8 mm diam., 564 mm f.l.

Lens 2; 141 mm diam., 282 mm f.l.

c. The design with three identical lenses is:

$$Q = 10^4$$

$$N = 144$$

$$\bar{N} = 70$$

$$\overline{Ncd} = 100 \text{ mm}, \quad \bar{d} = .96 \text{ mm}, \quad \bar{c} = 1.5$$

$$Ncd = 100 \text{ mm}, \quad d = .46 \text{ mm}, \quad c = 1.5$$

$$M_s = -1$$

Lens 1, 2, 3; 141 mm diam., 705 mm f.l.

2.2.5 <u>Gaussian Design Conclusion</u>. - Some basic relationships between system capacity and Gaussian properties of the transform optics were derived in the preceding sections for one- and two-lens systems. These relationships were then used to produce Gaussian layouts for 6.55×10^6 and 10^8 bit capacity systems. While these layouts provide comparative examples of size and complexity, they cannot be interpreted literally. The disposition and powers of the components are not free parameters, but have restrictions arising out of considerations of system capacity, mechanical considerations, and the requirement that the lens diameters must not be too great compared to focal length.

In practice, three important classes of considerations prevail:

1. As before, the system capacity should be maximized (or nearly so) and this produces relationships concerning various parameters of the block data composer (BDC), hologram array (HA), and photodetector array (PDA), and involving the focal length and effective F-number of the optics;

2. The position and size of the optical elements must be such that they do not interfere with or obstruct the operation of the system as a whole, of particular significance being the maintenance of a sufficient clearance before the HA to allow entry of the reference beam;

3. Any bit shifting that occurs on readout is directly attributable to the aberrations of the optics, so that these aberrations must be kept sufficiently small that the resulting bit shift does not give rise to error.

When these three considerations are combined, we found that the third item can only be satisfied if the freedom to determine the number of components and dispose of them on purely Gaussian grounds is largely sacrificed. As discussed below, the stringency of the aberrational requirements demands the incorporation of at least one component of negative power, and also strongly influences the relative positions of the positive elements.

The way in which the optical aberrations give rise to bit shifting on readout is as follows. Of course, the BDC is never directly imaged onto the PDA; the page is recorded in hologram form at the HA, and, subsequently, reconstructed at the PDA by a reference beam incident on the appropriate hologram. However, if we assume that the holographic reconstruction process is perfect, then the aberrations of the reconstructed image at the PDA are simply those that would have been obtained if the BDC had been imaged directly onto the PDA with the appropriate hologram replaced by a small aperture stop of the same size and position. Figure 2-6 shows the on-axis bit being imaged via a near-axial hologram and an edge hologram. The optical system is assumed to have zero aberration, and the position of the reconstructed bit is independent of which hologram has been used (or which small aperture stop has been used, as far as the optical design problem is concerned).
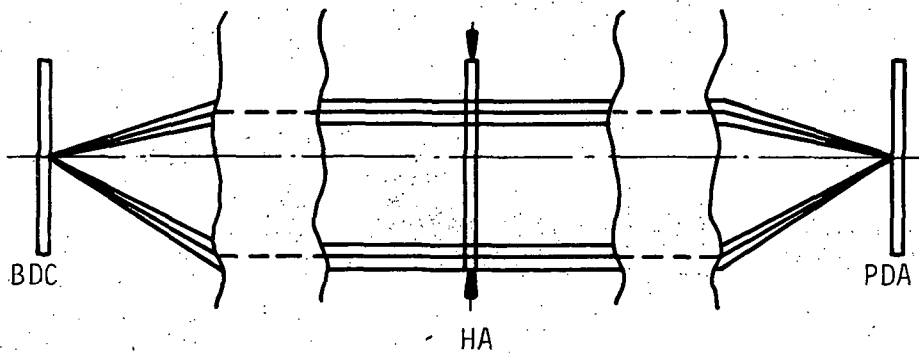
a) No Aberrations
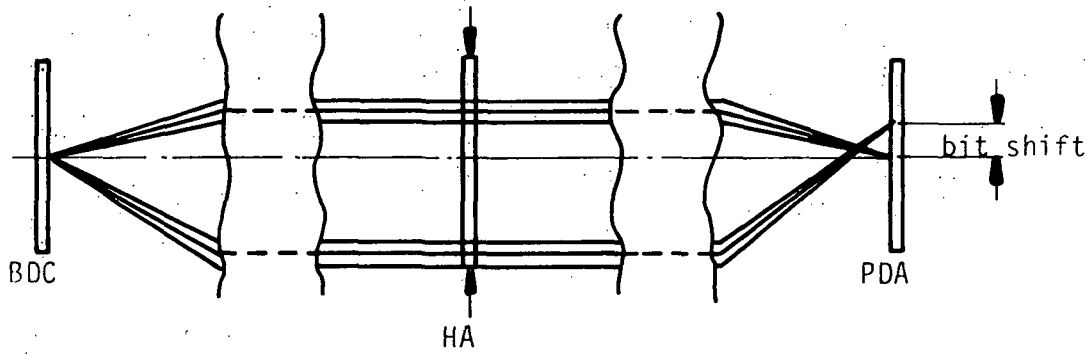
b) Spherical Aberrations Causing Bit Shift

Figure 2-6. Simple Bit Shifting

RADIATION

If this is true for all possible hologram positions, then we see that replacing the whole HA by a single large centered aperture stop at the same location and of the same diameter, would result in a point at the BDC being geometrically imaged perfectly as a point at the PDA. If this condition of perfect geometric point imagery does not prevail for the whole aperture, then bit shifting occurs to a greater or less degree, as shown in Figure 2-6b. Here, undercorrected spherical aberrations has produced the shift. This change of emphasis from the consideration of a small decentered stop in one of many positions to the consideration of a large centered stop is of great use in the optical design process, and allows us to formulate the aberrational requirements of the optical system from this viewpoint.

For zero bit shift we require perfectly stigmatic imagery over the whole PDA plane, with zero distortion. So that all the light from every possible hologram position reaches the PDA, we require zero vignetting. So that every hologram receives the superimposed light from every bit of the BDC, we require that the first part of the optical system (between the BDC and HA) has well-corrected pupil aberrations, and that it satisfies the Optical Sine Condition.* The last of these three requirements is considerably relaxed if we use a diffuser-type illumination behind the BDC, but, of course, the diffuser wastes a huge proportion of the available light. Also, if we can deliberately introduce specified amounts of certain aberrations into the illumination system, then we can produce an overall balance of aberration over the combined system which acts to somewhat relax this last condition.

In practice, of course, we can tolerate some slight bit shifting, and some slight noncoincidence of beamlets from all bits for each hologram (vignetting tolerance is effectively nil, however). Calculations of these permissible tolerances have recently been made. Their magnitudes depend, of course, on the various system parameters, but the aberrational specification of the optical system remains very tight indeed. In other applications where

---

* A restricted form of the Optical Sine Condition merely requires that the height of any ray at the hologram plane be proportional to the sine of the angle that the same ray makes with the axis as it leaves the axial point of the BDC.

a fixed high standard of performance over the field is required, there is rarely an insistence on zero vignetting, and the designer generally uses vignetting to his advantage to reduce the effects of extra-axial aberrations – this is possible because vignetting ordinarily implies merely loss of light and not loss of information. The third consideration of well-corrected pupil aberrations imposes an additional burden on the optical design.

2.3 Controlled Aberration Lens Design

We carried out a controlled aberration design of the signal path illumination and transform optics for the 6.55×10^6 bit memory and the $.25 \times 10^8$ bit memory. The 6.55×10^6 bit memory system designed using a 128 x 128 element BDC and a 20 x 20 hologram array was carried out to gain experience with the design techniques and programs and was not fully tool designed. The $.25 \times 10^8$ bit memory system design using a 128 x 128 element BDC and a 40 x 40 hologram array was completed including tooling and tolerancing. The maximum bit shift for an edge bit in the zonal hologram was 1/10 of the bit spacing at the PDA.

The following general description of the lens design procedure uses the parameters of the 6.55×10^6 bit memory system. The section following then reviews the $.25 \times 10^8$ design.

2.3.1 Lens Design Procedure.

– First, the physical details of the hardware dimensions are required to determine focal lengths, field angles, object sizes and image sizes. The approximate calculations of the values for the three independent lens aberrations (Petzval field curvature, chromatic variation of focal plane, and chromatic variation of magnification) are made for an assumed singlet construction. On this basis, a decision is made regarding a suitable number of components for the design (a component being here defined as one or more thin elements in effective contact). Initially, a choice between one or more components is made. If the choice is two or more lenses, then use is made of the principles of multilens Gaussian design published by Hopkins to establish preliminary designs for various arrangements of focal lengths and separations. The solutions with the best aperture ratios and best possibility of aberrational correction are selected to be progressed in parallel. This completes the Gaussian design.

A decision is then made regarding the number of elements in each component. This follows the procedures for establishing trial curvature of singlet- and two-components design published by Hopkins and Rao,[2] together with the lens designer's experience in using the aperture ratios of the components. A cemented doublet is normally preferred to an air-paced doublet in view of easier mounting and alignment. Target values of spherical aberration, central coma, and longitudinal chromatic aberration are selected for each component which, when combined, will produce the required correction. These target values are obtained by a variety of techniques, including curvature and glass-type selection. The system lenses are then thickened, suitable axial thicknesses consistent with the diameters of the elements are inserted, and the curvatures appropriately modified to restore the Gaussian properties of the system. This completes the primary aberration design.

Finite rays are now traced through the system and the effect of higher-order aberrations become apparent. These are balanced out by altering the primary aberrations via thick-lens curvature modifications.

When an adequate modified Gaussian design has been selected an automatic design program can then be efficiently employed. Computer programs have been used at earlier stages, but require manual guidance based upon the lens designer's experience to steer the design into a form offering the best possibilities.

The automatic design program used is POSD (a University of Rochester program); POSD is an acronym for Program for Optical System Design. It uses a damped least squares optimization procedure to minimize the weighted sum of squares of various selected image defects. Neither wave nor transverse ray aberrations are explicitly included in the choice of image defects, although various functions of ray aberrations are available. These include odd and even parts of ray aberration, fractional distortion, and coefficients of a ray aberration polynomial. A list of these constructional parameters which can be treated as variables

is given with the data and these may be weighted (that is sensitive variables may be heavily weighted to prevent violent system changes during optimization). The program contains some mechanism for the control of boundary conditions in order to prevent negative thicknesses, etc., but in parctice this part of the program does not always work satisfactorily, and frequent manual intervention is necessary. Also, it is not possible to control pupil aberrations which are relevant in this application as noted in the second quarterly report.[3]

POSD is procedure-oriented so that input and output appear alternately in a printout. The system is loaded into memory by the call LTM and each further call initiates some specific action; thus, FFT causes finite rays to be traced, SPT causes geometric spot diagrams to be output, FPR causes the "fifth-order" ray aberration polynomial coefficients to be evaluated, AUT causes the automatic design optimization procedure to be triggered, etc.

2.3.2 <u>Optics Required</u>. - The optics required can conveniently be divided into three parts, namely the deflection optics which provide the block data composer (BDC) with a set of full-aperture beams over a range of discrete directions, each direction corresponding to a different hologram, the BDC:HA optics which focuses each of these beams onto a different position in the hologram array (HA), these being source images, and the HA:PDA optics which arranges that the diverging beam from each hologram into a full-aperture beam at the photodetector array (PDA), the direction being different for each hologram. Each of these three parts is a two-conjugate system. In terms of the other set of conjugates the deflection optics focuses onto the BDC, the diverging beam which is arranged (by the BDC:HA optics) to pass through the full aperture of the HA, these beams forming a set of discrete directions, one for each bit, and then the HA:PDA optics focuses each of these beams onto the PDA, forming a reconstructed bit pattern image of the BDC.

The two conjugate sets are identifiable as source imagery and bit imagery, respectively. For either type of imagery the other corresponds to pupil imagery. It is for this reason that pupil aberrations must be considered at every stage of the design.

2.3.3 LA:BDC Optics. - Here each source produced by an element of a lenslet array (LA) must be converted into a near-collimated full aperature beam illuminating the BDC from a direction dependent upon the lenslet position in the array. Each source is ultimately imaged onto its conjugate hologram at the HA. The current system shown in Figure 2-7 employs a cemented doublet and singlet as the first component and a cemented doublet as the second component. This part of the optics plays two parts; its first task is to ensure that the light from each lenslet fully illuminates the BDC without vignetting. This illuminating beam must be near collimation in order to reduce the overall angular range of illumination at the BDC, however, there is no strict collimation requirement. The cone of light from each lenslet is arranged to be oversize so that a slight degree of nominal vignetting will still leave the BDC fully illuminated. The second task of this optics is to provide the first stage of the imagery of the lenslet sources onto the HA. In this source imagery, the BDC acts as the aperture stop and the entrance pupil is at infinity. There is also an aberrational requirement for this pupil imagery (which is also bit imagery).

The current system data for this part of the optics is shown in Figure 2-1a and the parameters are given in Table 2-2. Comments on performance and construction are given in Paragraph 2.3.6.

2.3.4 BDC:HA Optics. - Aberrational considerations for this part of the optics and the HA:PDA optics were discussed in the second quarterly report,[3] and the form of the initial design was shown. The BDC:HA optics has the source (or hologram) imagery task of completing the imagery of the LA sources onto the HA, and the bit imagery task of performing the first stage of imaging the BDC onto the PDA with the HA as the plane of the aperture stop. Further investigation of the initial design revealed that the source imagery at the HA was not adequate. Ideally, each source should be imaged at exactly the same point in the HA; in practice, some noncoincidence is permitted. Changes in the BDC:HA optics were found to be necessary to improve the HA imagery. The current system comprises a thick negative singlet followed by two positive cemented doublets is shown in Figure 2-7b and the parameters are given in Table 2-3.

RADIATION
A DIVISION OF HARRIS-INTERTYPE CORPORATION

A. LA: BDC OPTICS

LA

BDC

B. BDC: HA OPTICS

BDC

HA

C. HA: PDA OPTICS

HA

PDA
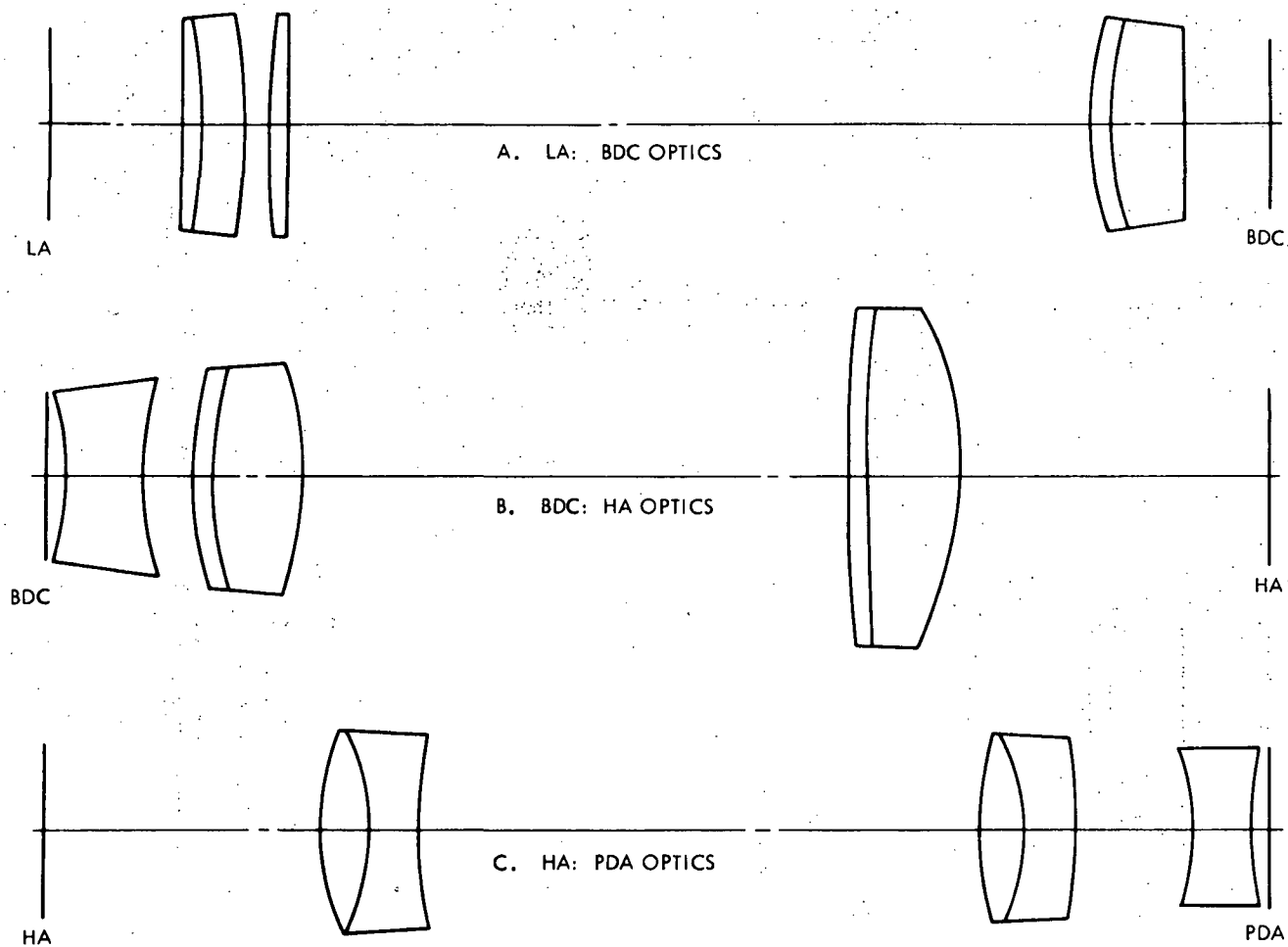
Figure 2-7. Optical System Design, 6.6×10^6 Bit Memory

TABLE 2-2. POST-LA DEFLECTOR OPTICS

r	d	t	μ	
9607.07	66.1			
		7.0	1.79882	1st doublet, f 14.7
-1316.22	66.1			
		14.0	1.65653	
-806.146	66.8			
		13.177	Air	
241.163	68.4			singlet, f 7.5
		6.0	1.61200	
993.720	70.6			
		260.380	Air	
81.6506	70.4			
		7.0	1.86305	
72.9501	68.6			
		23.911	1.61200	2nd doublet, f 2.3
491.884	65.6			

LA source plane to first surface distance = 40.033 mm

Last surface to BDC plane distance = 29.704 mm

r = lens curvature in mm^{-1}

d = working diameter of surface in mm

t = lens spacing or thickness in mm

μ = index of refraction

RADIATION
A DIVISION OF HARRIS INTERTYPE CORPORATION

TABLE 2-3. BDC:HA OPTICS

r	d	t	μ	
-86.498	46.5			
		27.123	1.51032	first component, f 1.6
74.856	53.8			
		15.972	Air.	
122.317	66.7			
		7.0	1.70255	
86.804	68.5			second component, f 1.9
		22.835	1.46773	
-106.081	72.1			
		137.714	Air	
698.749	103.9			
		7.0	1.65653	
2211.52	104.3			third component, f 2.5
		21.932	1.52002	
-166.808	105.4			

BDC plane to first surface distance = 3.945 mm

Last surface to HA plane distance = 240.467 mm

r = lens curvature in mm^{-1}

d = working diameter of surface in mm

t = lens spacing or thickness in mm

μ = index of refraction

2.3.5 <u>HA:PDA Optics</u>. - The design configuration of the HA:PDA optics was also modified (via POSD) to recorrect the PDA imagery; this part of the optics inherits a large amount of aberration (with respect to the bit imagery) from the BDC:HA system. The current system consists of two doublets followed by a singlet as shown in Figure 2-7c and the lens parameters are given in Table 2-4.

2.3.6 <u>Comments on Performance, Construction and Next Steps</u>. - If the entire optical system following the lens array, LA is taken together (as in Figure 2-7), the rays are traced from an object at infinity and entrance pupil at the LA source plane, and with the aperture stop at the HA, then each object space field angle is equivalent to a different bit position when the aberrations of the post-LA deflector optics are small, and choosing different points in the aperture corresponds to different holograms in the array. Even when the first system aberrations are not small, any chosen ray (in terms of its position in the aperture and field) may be identified with a certain bit and a certain hologram by its intersection with the BDC plane and LA source plane. If traced through to the PDA, its position, relative to the Gaussian image position of the bit with which it is identified, reveals the amount of bit shift associated with this bit-hologram pair upon reconstruction. The bit shift is the transverse ray aberration.

2.3.7 <u>Design .25 x 10^8 Optics</u>. - The physical parameters for several .25 x 10^8 bit capcity optics system design are given in Table 2-5. We have selected the design which incorporates the 128 x 128 bit BDC and the 40 x 40 hologram arrays. This is the largest bit size BDC we expect to be available in the next few years and the hologram array is a size which can be conveniently fabricated. The Gaussian optics system using simple lenses will be three times the focal length of the basic lens or .95 meters long with a lens diameter of

RADIATION
A DIVISION OF HARRIS INTERTYPE CORPORATION

TABLE 2-4.   HA:PDA OPTICS

r	d	t	μ	
74.305	72.4			
		19.994	1.52002	first component, f 4.2
-75.036	72.0			
		18.444	1.65653	
323.625	69.0			
		144.657	Air	
59.137	64.3			
		18.000	1.46773	second component, f 2.3
-81.526	63.4			
		15.103	1.70255	
-494.805	58.7			
		31.192	Air	third component, f 1.3
-37.787	45.6			
		12.324	1.51032	
143.678	50.5			

HA plane to first surface = 81.737 mm

Last surface to PDA plane = 4.968 mm

r = lens curvature in mm^{-1}

d = working diameter of surface in mm

t = lens spacing or thickness in mm

μ = index of refraction

TABLE 2-5. 0.25 × 10^8 BIT CAPACITY MEMORY COMPARISONS

#BDC BITS	N	100	116	*128	144	256
#HA Holograms	$\bar{N}$	50	44	40	35	20
BDC Bit Spacing	cd	625 μm	466 μm	390 μm	254 μm	254 μm
HA Hologram Spacing	$\bar{c}\bar{d}$	1.25 mm	1.25 mm	1.25 mm	1.06 mm	3.3 mm
Size BDC and HA	$Ncd=\bar{N}\bar{c}\bar{d}$	62.5 mm	54 mm	50 mm	36.6 mm	65 mm
Gaussian Lens Design	f#	2.86	2.42	2.22	1.38	2.42
Gaussian Lens Design	F.L.	510 mm	369 mm	314 mm	143 mm	445 mm

*Parameters selected

111 millimeters. The controlled aberration lens design using multielement distributed lens is larger than the Gaussian design. The system is 1.57 meters long with a maximum lens diameter of 140 mm.

We sifted through about 50 likely three-lens solutions (for the basic symmetry-unit of the complete system) and did initial aberration calculations on all of these to ensure that the ones we chose for further action had low primary aberrations per component as well as reasonable f/#s, spacings, diameters, etc. This was important as we intended to make full use of symmetry in the system (such that the whole LA:PDA system will comprise three times the basic unit) in order to minimize manufacturing and mounting costs.

The current system represents a careful compromise between mechanical and optical considerations (i.e., the system is as short as practical), and there is no doubt that attempting to make significant dimensional reductions would have the effect of reducing system symmetry, as well as the more obvious consequences of increasing the number and complexity of the components, requiring more exotic glass types, and increasing the difficulty of the design.

Design Approach - The design approach is to use a basic Gaussian design which can be used in a symmetrical approach to reduce or cancel the aberrations of a 3-unit symmetrical approach where the optics subsystems A, B, C, Figure 2-8, are identical.

As far as bit imagery is concerned (BDC:PDA), the primary aberrations of system (B + A) are related to those of System A above as follows:

Sph. abr. $S_1 = 2(S_1)_A$

Coma $S_{11} = $ zero

Astig. $S_{111} = 2(S_{111})_A$ (52)

Petz. fld. curv. $S_{iv} = 2(S_{iv})_A$

Distn. $S_v = $ zero
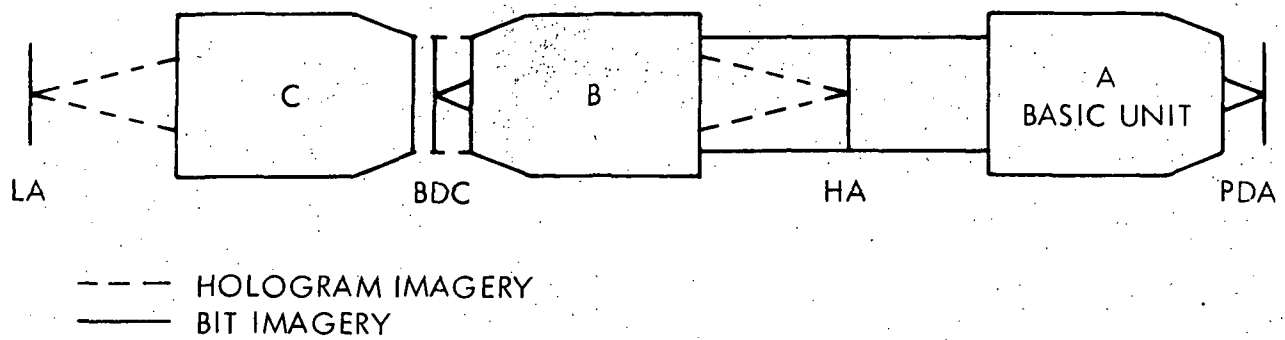
Figure 2-8. Three Unit Symmetrical Optical System

The zeros of the odd aberrations arise because of symmetry about the stop (at the HA). Thus, to make all the primary aberrations for bit imagery small, one only needs to design the basic unit A with small values of $(S_1)_A$, $(S_{111})_A$, $(S_{iv})_A$.

Now as far as hologram imagery is concerned (LA:HA), the primary aberration of system (C + B) are related to those of system C in the same way as above; that is

$$S_1 \quad = 2(S_1)_C$$

$$S_{11} \ = zero$$

$$S_{111} = 2(S_{111})_C \tag{53}$$

$$S_{iv} \ = 2(S_{iv})_C$$

$$S_v \quad = zero$$

Because of the symmetry, the LA is to system C (in respect of distances and orientation of optics) exactly as the HA is to system A. That is, the aberrations of LA imaged through C are those of HA (as object) imaged through A. Thus, the aberrations of LA imaged through C are simply the pupil aberration of system A. Thus,

$$(S_1)_C \quad = (S_1)_A$$

$$(S_{11})_C \ = (S_{11})_A$$

$$(S_{111})_C = (S_{111})_A \tag{54}$$

$$(S_{iv})_C \ = (S_{iv})_A$$

$$(S_v)_C \quad = (S_v)_A$$

So that good hologram imagery is obtained by keeping $(S_1)_A$, $(S_{111})_A$, $(S_{iv})_A$ small, with S_{11} and S_v cancelling to produce zeros. This follows from (53) and (54).

Now primary pupil aberrations are not independent of regular primary aberrations (except for S_1, S_1) even for a general system. And if, in particular, we arrange that for system A the bit-imagery object is at ∞ and the hologram-imagery image is at ∞ (both

desirable in that ray angles of BDC and HA are reduced and the LA lenslets work on axis)
then, in our case, this gives

$$(S_{11} - S_v)_A = 100.5\lambda$$

$$(S_{111} - S_{111})_A = zero$$

$$(S_{iv} - S_{iv})_A = zero$$

$$(S_v - S_{11})_A = 100.5\lambda$$

and $(S_1)A$, $(S_1)_A$ are independent.

This implies that making $(S_{111})_A$, $(S_{iv})_A$ near-zero to control bit-imagery automat-
ically ensures the correction of the hologram-imagery aberrations $(S_{111})_A$, $(S_{iv})_A$. Thus,
for good bit and hologram imagery for the complete optics, one need only control

$$(S_1, S_1, S_{111}, S_{iv})_A$$

and the remaining 6 aberrations $(S_{11}, S_{11}, S_{111}, S_{iv}, S_v, S_v)$ will be automatically
dealt with.

The correct functioning of this theory in the practical lens design case depends on
keeping low the higher-order aberrations, since they do not conform to this theory – the
theory is for primary aberrations only. One must, therefore, ensure that the design is
primary-aberration dominated.

Given this state of affairs, this approach relieves the designer of the task of
attempting simultaneously to control all of the pupil and regular aberrations – a job
requiring a special set of computer programs to be handled successfully (if a successful
solution is obtainable by this route).

In the current design we are forcing the system to be primary-aberration dominated
by ensuring that angles of incidence and ray deviations are kept small throughout the
system. The price paid for this is the probable adding of an extra couple of elements
per unit (i.e., the system A) but this is more than compensated for by, a) saving on
special programs, b) permitting more reliable "next step" forecasting of difficulties and

RADIATION

"state of the design" assessments, and c) almost certainly leading to a "tolerant" final design in respect of production errors.

The reduction of hologram optic aberrations demands that S_{11}, S_{11}', S_v, S_v', although finally exactly cancelling to zero, should not be too large in System A, otherwise they will induce noncancelling hologram optic aberrations. This poses certain difficulties. For example, (52) implies that S_{11} and S_v cannot be simultaneously small. Here, the way out is that 1 percent distortion $= 156\lambda$ of S_v and so a quite small amount of pincushion distortion will allow S_{11} to be reduced - unfortunately the "natural" distortion for the system A is broad and so a problem is encountered. This particular one is now mostly resolved.

The S_1 problem has been solved by changing the power balance and allowing S_{iv} to rise somewhat; S_{iv} is now around the maximum acceptable level - about equivalent (in system A) to a single component of focal length of 1.2 meters.

Non-Tool Fitted Design

We include below details of the monochromatic non-tool fitted design for a 128 x 128 bit BDC and a 40 x 40 hologram array.

This details the optics between the lenslet array focal plane and the photodetector array. The design described is for the wavelength 514.5 nm prior to fitting the curvatures to a manufacturer's tool list. The glasses used are all Schott; they are all on the Schott preferred list, none of them have extreme chemical or mechanical properties. They are all available in large diameter blanks, and none are bubble prone.

Fabrication should be straightforward, with no deep curvatures or knife edges to present problems. The design is relatively insensitive to production errors (as established by a very rough first attempt tool-fit during which some of the curvatures changed by as much as 2 percent, and with no attempt to compensate for this, when the aberrations increased by up to 15 percent - consequently a typical curvature error of 0.03 percent will have a negligible effect on aberration) so that standard workshop tolerances will be

perfectly acceptable (e.g., radius: ±0.03%, spherically: 1 fringe, thickness: ±2 mils; diameters: + zero, -2 mils).

Because of the precisely symmetrical construction, the complete system involves only 7 different elements (each being required 3 times for one complete system). This will keep down fabrication costs.

Construction - As shown in Figure 2-9 and the Table 2-6 of surfaces, the system comprises 3 exact copies of the basic unit of 7 elements in 3 groups.

Performance

a. Bit Imagery - The maximum bit shift is less than 40 microns as shown in Figure 2-11. That is the maximum relative displacement between reconstructed bits and their corresponding photodetectors does not exceed 40 microns for any hologram. This maximum occurs for end-of-diagonal bits reconstructed from end-of-diagonal holograms. This maximum shift represents only one-tenth of the inter-bit spacing and should not, therefore, significantly degrade the S/N ratio of the system.

b. Hologram Imagery - The LA focal plane is imaged at the HA and the departure of an LA spot image (for a given bit) from its geometrical position in the HA is interpreted as a hologram shift. The maximum hologram shift does not exceed 40 microns. This effect is illustrated in Figure 2-10. The maximum shift occurs for an end-of-diagonal hologram receiving light from an end-of-diagonal bit, and represents only 3 percent of the inter-hologram spacing - clearly a negligible effect.

c. Chromatic Correction - This has not been of concern in the system as it now stands. That is, the glasses have been chosen for qualities other than dispersions. This is evidenced by the fact that for the last 2 components the positive elements are flint and negative crown - a reversal of the standard procedure. As it happens, the chromatic is not too bad for bit imagery - much of the
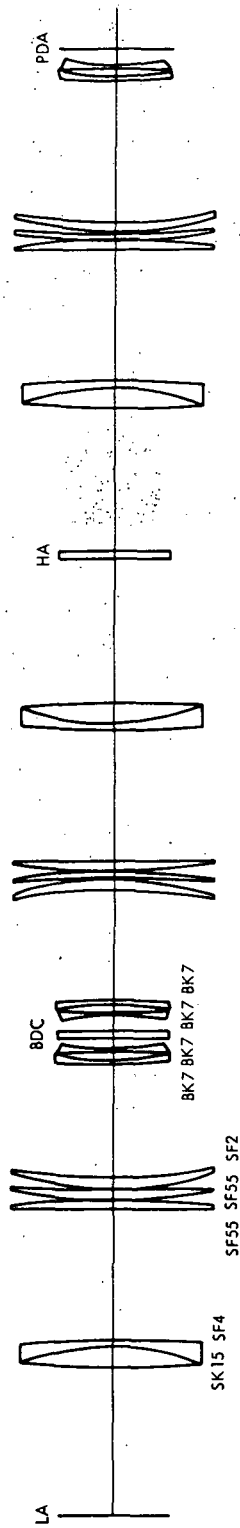
RADIATION
A DIVISION OF HARRIS · INTERTYPE CORPORATION

PDA

HA

SCALE X $\frac{1}{3}$ [(REFERENCE: DRAW1A/110473/142143)]

BDC

BK7 BK7 BK7 BK7

SF55 SF55 SF2

SK15 SF4

LA

Figure 2-9. Untooled System

Table 2-6.

LA:PDA SYSTEM

43SURFS	:DISPERSIONS	.OTH SURF IS STOP	0 ASPHERICS	WAVELENGTH	.00051450

SURF	C	n	N	DISPS
			1.00000	.000000
1	.001517			
		16.0000	1.62792	.010340
2	-.005486			
		4.50000	1.76785	.026670
3	-.001731			
		369.463	1.00000	.000000
4	.000000			
		6.50000	1.77486	.027540
5	-.001912			
		.200000	1.00000	.000000
6	.002151			
		6.50000	1.77486	.027540
7	.000241			
		.200000	1.00000	.000000
8	.004318			
		8.50000	1.65652	.018590
9	.002093			
		97.3000	1.00000	.000000
10	.000882			
		3.00000	1.52049	.007740
11	.004453			
		5.00000	1.00000	.000000
12	-.000813			
		3.00000	1.52049	.007740
13	.004628			
		6.36037	1.00000	.000000
14	.000000			
		6.35000	1.50000	.007740
15	.000000			
		10.5937	1.00000	.000000
16	-.004628			
		3.00000	1.52049	.007400
17	.000813			
		5.00000	1.00000	.000000
18	-.004453			
		3.00000	1.52049	.007740
19	-.000882			
		97.3000	1.00000	.000000
20	-.002093			
		8.50000	1.65652	.018590
21	-.004318			
		.200000	1.00000	.000000
22	-.000241			
		6.50000	1.77486	.027540
23	-.002151			
		.200000	1.00000	.000000
24	.001912			
		6.50000	1.77486	.027540
25	.000000			
		369.463	1.00000	.000000
26	.001731			
		4.50000	1.76785	.026670
27	.005486			
		16.0000	1.62792	.010340
28	-.001517			
		224.036	1.00000	.000000
29	.000000			
		6.35000	1.50000	.007740
30	.000000			
		219.8?3	1.00000	.000000
31	.001517			
		16.0000	1.62792	.010340
32	-.005486			
		4.50000	1.76785	.026670
33	-.001731			
		369.463	1.00000	.000000
34	.000000			
		6.50000	1.77486	.027540
35	-.001912			
		.200000	1.00000	.000000
36	.002151			
		6.50000	1.77486	.027540
37	.000241			
		.200000	1.00000	.000000
38	.004318			
		8.50000	1.65652	.018590
39	.002093			
		97.3000	1.00000	.000000
40	.000882			
		3.00000	1.52049	.007740
41	.004453			
		5.00000	1.00000	.000000
42	-.000813			
		3.00000	1.52049	.007740
43	.004628			
			1.00000	.000000

RADIATION
A DIVISION OF HARRIS-INTERTYPE CORPORATION

MAXIMUM
DISPLACEMENT
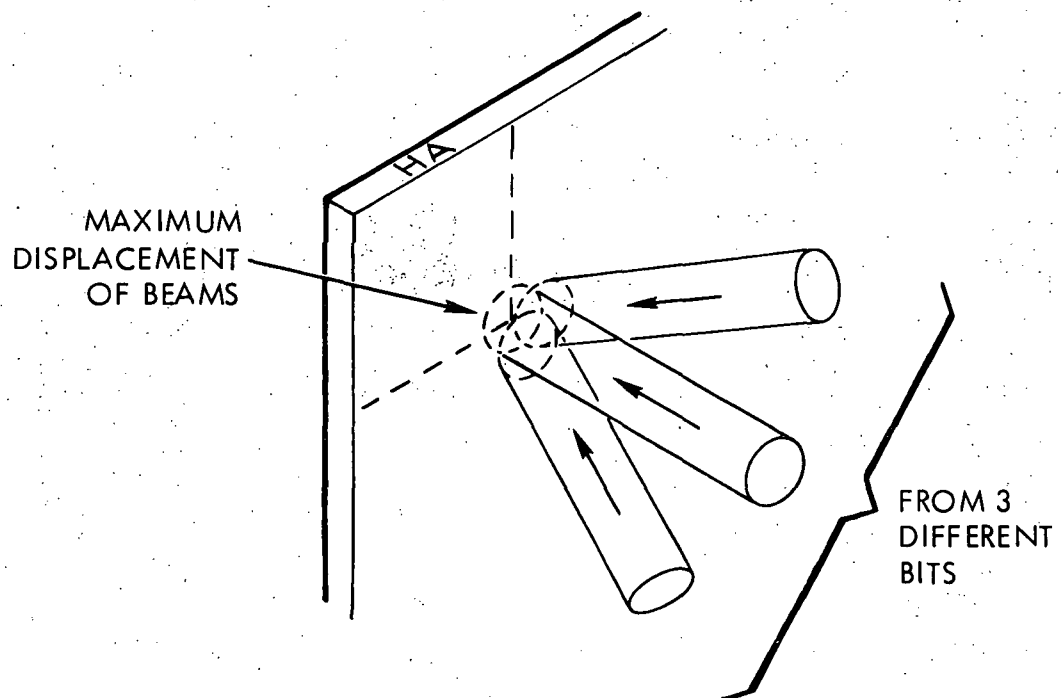OF BEAMS

FROM 3
DIFFERENT
BITS

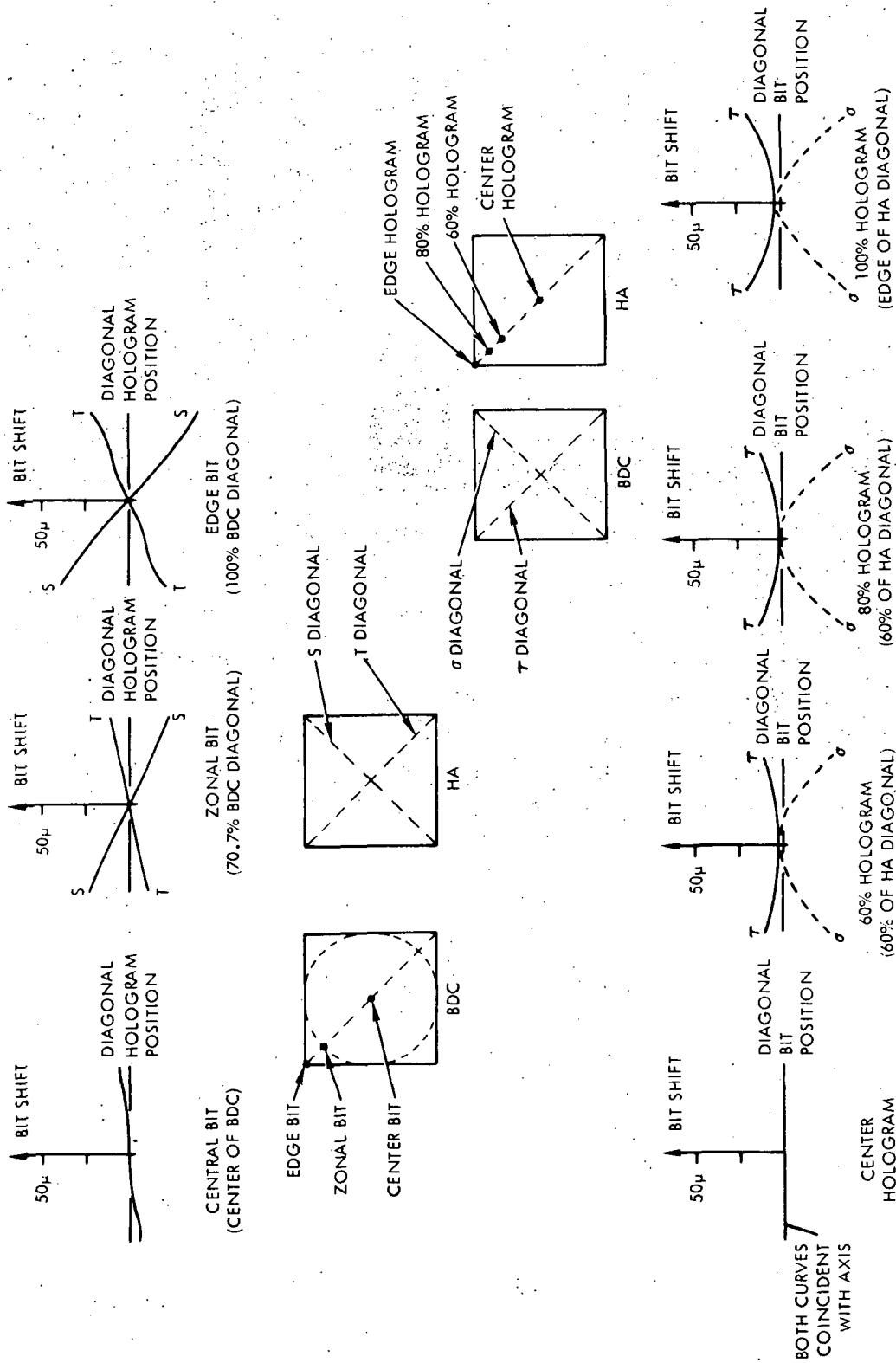Figure 2-10.   Hologram Imagery

Figure 2-11. Plot of Bit Shifts

aperture and field being probably within specification, but the chromatic aberrations in the hologram imagery renders the optics unusable at wavelengths significantly different from 514.5 nm.

Changing the SFSS and SF2 to LaFN2 (much more exotic glass) and the BK7 to a light flint would improve the chromatic situation without any serious degradation of 514.5 performance but would still leave the chromatic well outside specification for use at 632.8 or 480.0. However, it is a good possibility that this could be achieved by converting the first element of the second-component into a doublet. Thus, the price to pay for polychromatic operation is probably an extra element in the basic unit and the use of the less-desirable (in terms of chemical properties and sizes of blanks readily available) glass LaFN2 in the large diameter elements.

Tooled 128 x 40 Mono Design - The final tooled design lens data, together with tolerances, is given below.

The list of data, Table 2-7, includes the illumination optics, of course, the first "surface" is the array of point sources produced by the lenslet array, the 14th and 15th surfaces are the BDC with the 15th surface being the active side of the substrate, surfaces 29 and 30 are the HA with the 29th surface being the active one, and surface 44 is the plane of the photodetector array.

During the "tooling" process of replacing the computer surface curvatures by nearby ones in the Herron tool list, the changes involved ranged up to two percent, and up to a fringe departure of 240 fringes. The Gaussian and aberrational properties were then restored simply by adjusting the air gaps between the components - no glass thickness or small air thickness was altered, and no reselection of tools (to adjust powers or shapes) was necessary. The changes in the air gaps were -3 mm in a distance of 224 mm, -0.8 mm in a distance of 97.3 mm, and +0.7 mm in a distance of 10.6 mm.

TABLE 2-7. TOOLED SYSTEM

	Radius of Curvature in Inches (Tools from Herron List)	Axial Separation or Thickness in Millimeters	Schott Glass Type (Catalog 3050e)	Clear Semi-Aperture in Millimeters	Recommended Manufactured Semi-Diameter in Millimeters
1	25.853	16.0000	SK15	60.7	64.5
2	-7.170	4.5000	SF4	60.8	64.5
3	-22.833	369.4630	Air	61.4	64.5
4	∞	6.5000	SF55	69.7	72.0
5	-20.592	0.2000	Air	69.7	72.0
6	18.142	6.5000	SF55	68.9	72.0
7	166.875	0.2000	Air	68.7	72.0
8	9.146	8.5000	SF2	66.9	72.0
9	19.033	96.4843	Air	66.2	72.0
10	44.636	3.0000	BK7	38.7	41.0
11	8.853	5.0000	Air	37.6	41.0
12	-47.554	3.0000	BK7	37.2	39.5
13	8.502	7.0673	Air	36.4	38.5
14	∞	6.3500	μ = 1.5 Plexiglass		As required
15	∞(BDC)	11.3006	Air		
16	-8.502	3.0000	BK7	36.4	38.5
17	-47.554	5.0000	Air	37.2	39.5

TABLE 2-7. TOOLED SYSTEM (Continued)

	Radius of Curvature in Inches (Tools from Herron List)	Axial Separation or Thickness in Millimeters	Schott Glass Type (Catalog 3050e)	Clear Semi-Aperture in Millimeters	Recommended Manufactured Semi-Diameter in Millimeters
	(Surfaces 16 to 28 are simply a mirror reflection of surfaces 1 to 13)				
27	7.170	16.0000	SK15	60.8	64.5
28	-25.853	221.0481	Air	60.7	64.5
29	∞(HA)	6.3500	μ = 1.5 Glass		
30	∞	216.8147	Air		
31	25.853	16.0000	SK15	60.7	64.5
	(Surfaces 31 to 43 are simply an exact copy of surfaces 1 to 13)				
42	-47.554				
43	8.502	3.0000	BK7	37.2	39.5
44	∞(PDA)	11.3006	Air	36.4	38.5

In view of these results and bearing in mind that the fabrication errors in curvature introduced by a combination of spherometer error (in measuring the test plate) and failure-of-fit error (comparing the surface with the test plate) are unlikely to exceed 0.05 percent or so, we may reliably conclude that there will be no difficulty on assembly, since any slight discrepancy may be readily taken up by air-gap adjustment. This assumes that ordinary workshop tolerances are applied during fabrication (of the type normally used for good quality image-forming optics) – no specially tight tolerances are required and it is wasting money to ask for them. We would expect these "standard tolerances" to be:

radius of fit to test plate	:	within 5 fringes
sphericity	:	within 1 fringe
glass axial thickness	:	±0.002"
finished diameter	:	+ zero, -0.002"
test plate radius	:	±0.04%

In our experience, manufacturers have 3 sets of standard tolerances that they apply in the absence of contrary information: these are "condenser quality," "ophthalmic quality," and "good image-forming quality." The above list corresponds to the last type.

As a cost-control exercise, we asked a manufacturer for a quote for 2 complete sets of the optics (based on his tool list).

The price estimate for two complete sets from OMT Ltd. was $1,800, excluding materials (one complete set is LA:PDA).

The tolerances for tilt and displacement (i.e., eccentric mounting) have not been established. We are not yet equipped to handle this sort of error. One can say qualitatively that large meniscus lenses of the type used in SF55 and SF2 do normally require careful mounting, but this is unlikely to present a major difficulty. Eccentric edging by the manufacturer is also unlikely to be severe enough to be serious, but it would be safest to check the tolerance on the same program (off-axial displacement is, in fact, entirely equivalent to a surface tilt plus a negligible axial displacement, for a spherical surface).

RADIATION
A DIVISION OF HARRIS INTERTYPE CORPORATION

2.4 Breadboard System

We considered several alternative system configurations which conform to the available BDC, PDA, and hologram array devices and which can be incorporated into the test breadboard system at NASA/Marshall.

The present illumination of all the lenses in the lenslet array contribute light simultaneously to all locations in the hologram array resulting in poor optical efficiency. Exposures on the order of several seconds is presently required. Deflection of the laser beam in the signal path as well as the reference path will increase the optical efficiency in future test bed modifications. We have considered three approaches to odd signal path laser beam deflection to the test-bed system: (1) the use of a small mirror (3 x 3 mm) galvanometer deflection system capable of deflection over relatively large angles (order of five degrees) thereby deflecting the laser illumination to a selected lens in the lenslet array, (2) the use of a large mirror (50 x 50 mm) galvanometer deflection system deflecting a wide aperture beam through a simple single lens illumination system to the selected hologram, and (3) the use of a high efficiency holographic optical element which redirects the laser illumination from an acousto-optic beam deflector to the selected hologram.

The photodetector hardware and software is presently designed to readout a Texas Instrument 32 x 24 bit array. The array data can be read out and transferred to the controller buffer memory in 192 μs. The effective readout rate will depend upon the integration time which is selected considering the reconstruction illumination energy/bit, the PDA detector sensitivity, and the acceptable system error rate. We expect the integration time for the test-bed to be on the order of 1 ms providing an effective read rate of .768 MHz. Larger PDA arrays and shorter integration times in future systems will provide increased read rates on the order of 1-10 MHz. A hardware/software modification, adding an interface for an additional eight detector rows, will be required to read out and transfer the full 32 x 32 bit Westinghouse array.

The test breadboard at NASA/MSFC is being retrofitted with a Westinghouse 32 x 32 element photodetector (PDA) in place of the less sensitive Texas Instrument array which had 1.016 mm column by 1.27 mm row detector spacings.

The Westinghouse 32 x 32 bit photodetector array elements are on 254 μm centers which will be compatible with the 128 x 128 bit block data composer (also 254 μm centers) when operated with the unity magnification image optical system. If we position the photodetector to collect the central 32 x 32 matrix of imaged block data composer bits, the errors previously reported[4] resulting from bit shifting will be reduced. Bit shifting was experienced in the test-bed transform lens system as a result of uncorrected spherical aberration over the full 128 x 128 bit BDC array diagonal of 40.32 mm.

$$\tan \phi = \frac{Ncd}{2\,FL}$$

where Ncd = 32.5 mm

FL = 184 mm.

For small angles

$$\phi = \frac{32.5}{2 \times 184} \text{ radians}$$

$$\phi = .0884 \text{ radian}$$

$$\phi = 5.05°$$

The beam deflection required for the system is therefore approximately ±5° and the mechanical deflection required of a mirror galvanometer will be ±2.5°.

We report first on the deflection systems followed by the photodetector test results.

2.4.1. Galvanometer Deflection Systems. - The present holographic storage material, photoplastics, require several seconds to complete the record cycle. Storage materials being investigated and developed can be expected to decrease the cycle time. In the present test-bed we use a lens array whose geometry matches the hologram array. Each

lens in the array focuses a part of the incident signal path illumination through the BDC to the hologram plane. The result is a simultaneous array of Fourier transforms of the BDC in the hologram plane, only one of which we will record. We can optimize the present system by deflecting the signal path illumination to the selected hologram. We are investigating an x, y galvanometer deflection system for the prototype development as a simple state-of-the-art device which can later be replaced by a more sophisticated beam deflector.

The input deflection angles required to select any hologram in the array are identical for the systems being considered and are determined by the size of the block data composer and the focal length of the transform lens (see Figure 2-12).

We have considered several system configurations using x, y galvanometer systems which can be incorporated into the test breadboard systems at NASA/Marshall. The two systems which satisfy the system requirements are described, one requiring a single pair of x, y galvanometers and a second using two pairs of x, y galvanometers.

We evaluated galvanometer systems as an available, economical, state-of-the-art technique to increase the optical efficiency and resolution of the test breadboard system. The relatively slow access time of the galvanometers, order of 5 ms, can still provide 3×10^6 bits/second readout data rates.

2.4.2 Galvanometer System Design. - A holographic memory system using mirror galvanometer deflection is shown in Figure 2-12a. The laser beam controlled by a shutter is shaped to a .75 mm diameter beam and directed by the x, y galvanometer combination to a selected lens on the 20 x 20 lens array. The single illuminated lens is imaged by a pair of lenses onto the 20 x 20 hologram array through the block data composer. This configuration is considerably more efficient optically than the present breadboard system which divides the illumination over the entire 20 x 20 lens array, imaging the block data composer simultaneously on the 400 hologram positions although only one is being recorded. A Glan-Air prism passes the vertical polarized component of the x, y deflected laser beam into the signal path and directs the horizontal polarized component into the reference path.
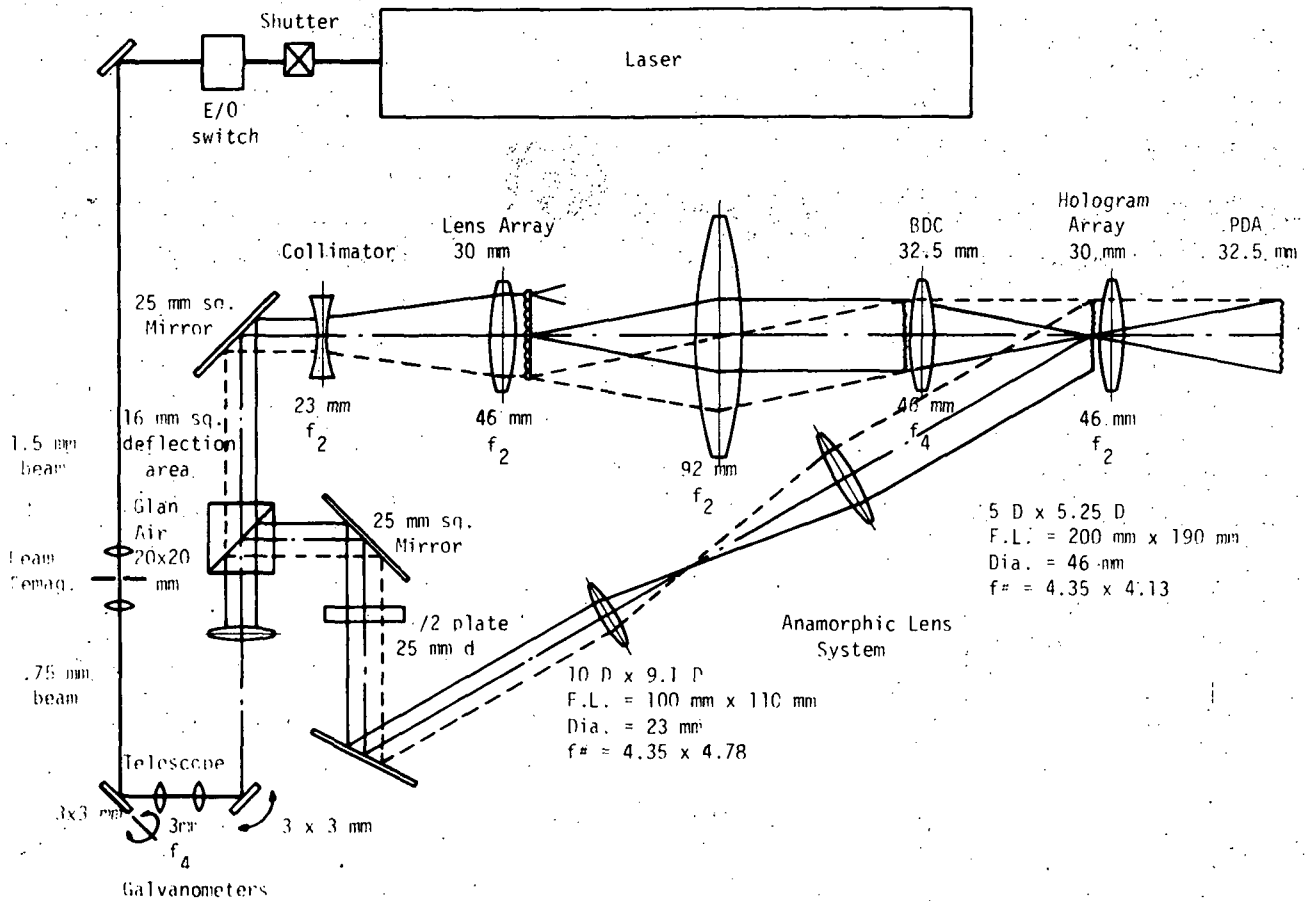
Figure 2-12a. Galvanometer Deflecting System

RADIATION

The vertical/horizontal polarization components are determined by the electro-optic switch which under system control rotates the laser's vertical polarization. A $\lambda/2$ plate is provided in the reference path to rotate the horizontal polarization component back to vertical polarization maximizing the hologram efficiency.

The x, y galvanometer deflection system initially deflects the laser beam over a 16 x 16 mm spatial array. This reduces the size of the Glan-Air prism required. Prisms are normally available with a 20 x 20 mm aperture or smaller. The signal path spatial array deflection is expanded after the Glan-Air prism by a telescopic lens system to cover the 30 mm x 30 mm lens array.

The reference beam spatial deflection is expanded by an anomorphic telescope system. The telescope system is necessary to properly invert the reference spatial deflection and track the hologram position selected by the signal path optics. The anomorphic lens is required in the telescope to provide unequal x and y deflection compensating for the hologram array not being perpendicular to the reference beam deflection axis. The telescope lens is approximately f/4 in both axes with the anamorphic parameters specified in diopters on Figure 2-12a.

The x galvanometer and y galvanometer are also coupled by a telescope system so that the x and y deflection will have the same deflection center. The 3 x 3 mm mirrors required in this system allow small fast galvanometers to be used. An acousto-optic beam deflector system (AOBD) is compatible with this galvanometer deflection system and AOBD systems with adequate bandwidth and performance are under development.

A second system is shown in Figure 2-12b. This system is considerably simpler optically but is not expected to be compatible with developing AOBD systems. A smaller 5 x 5 mm Glan-Air prism can be used. A 20 x 20 lens array is not required, the hologram position selection being determined directly by the galvanometers. The signal path optics between the BDC and the PDA are identical to the previous system. Four galvanometers are required, the signal and reference path being deflected separately. The major disadvantage is the relatively large 50 x 50 mm mirror required for y deflection which will reduce the system access time by a factor of ten, from 5 to 50 ms.
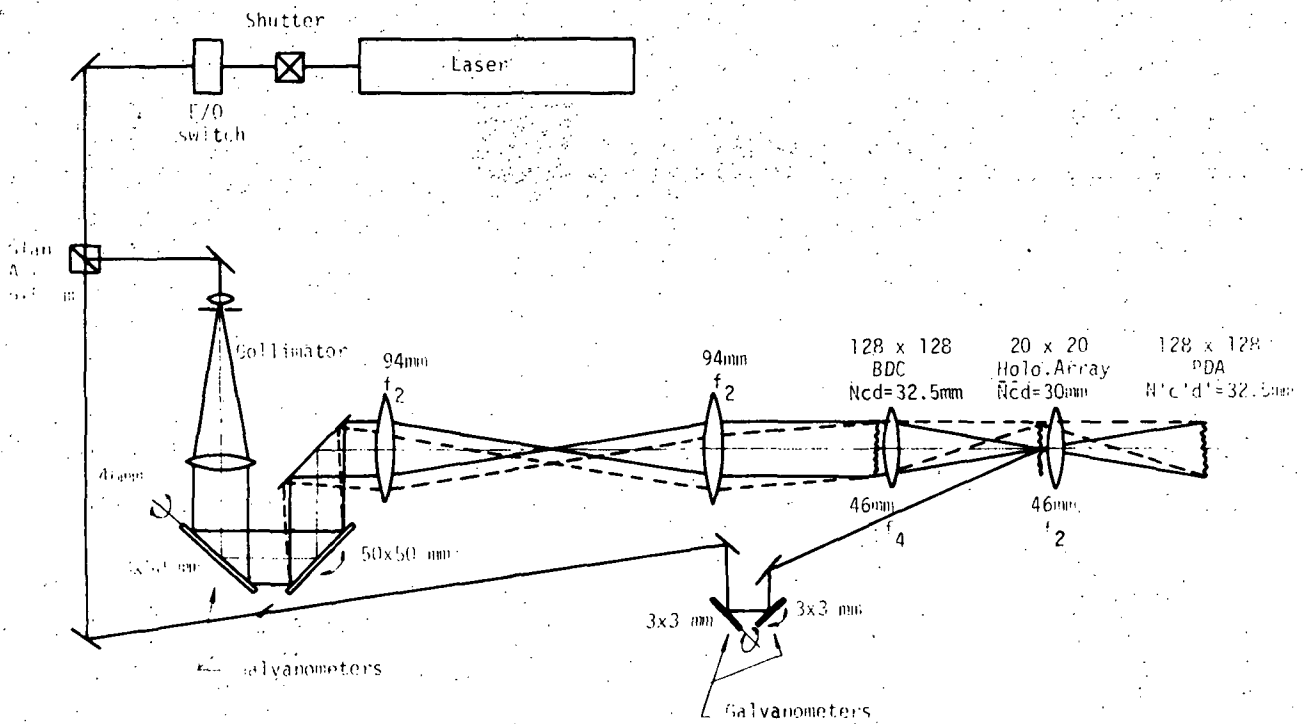
Figure 2-12b. Quad Galvanometer Deflection System

2.4.3 Galvanometer Techniques. - We investigated the mirror galvanometer deflection for holographic memory systems. The optical scanner we tested is a General Scanning G-108 with an optional position transducer. The response of the device is determined by the total inertia, mirror plus armature. A 6 mm square mirror with the pivot axis through the front surface of the mirror is mounted on the scanner. The rotary inertia of this mirror is approximately 1/3 of the galvanometer armature inertia and therefore reduces only slightly the no load (without mirror) resonant frequency of the device. The frequency response of the scanner with the mirror was determined by driving the device with a sinewave and measuring the peak-to-peak deflection. A resonant frequency of 1.038 kHz was measured. The maximum peak-to-peak mechanical rotation of $\pm 4^\circ$ provides a $\pm 8^\circ$ optical deflection, more than adequate for the deflections required by the proposed system. The armature coil resistance of 8 ohms required a ± 600 milliamp drive to reach the peak-to-peak deflection.

Approximately 1.8 watts are dissipated in the coil at maximum drive voltage and a proper heat sink is required to assure the repeatable position accuracy of .05 percent of the peak-to-peak deflection. If a positional error of 10 percent can be tolerated in selecting the hologram location, the scanner still has a 200-position capability which exceeds the anticipated system requirements.

The galvanometer linearity 1 percent of the peak-to-peak deflection is a factor of 20 less than the positional repeatability. We can store in the system controller's program the appropriate voltage steps required to drive the scanner and obtain the desired linearity. Alternatively, a positional transducer is available on the scanner being tested, which with the appropriate feedback to the driver coil, can directly improve the linearity of the device. A linearity of .2 percent of peak-to-peak deflection can be obtained providing a 50-position capability directly without requiring unequal step programming compensation. The position transducer also provides a temperature stability of .02 percent per degree C. The transducer consists of a variable capacitance bridge connected to the armature shaft and reduces the frequency response of the device by 30 percent. The bridge circuit has a 10 μs signal rise time and will not increase the scanner response.

The scanners are second order systems which are characterized by the resonance and damping parameters. If underdamped, the galvanometers will react to a step function with an overshoot and oscillation around the desired position. If critically damped, the scanner would provide a stable system but increase the step time. A signal processing technique is utilized to minimize the response time, i.e., the galvanometer is driven by a modified step function. Initially, only a fraction of the step voltage is applied to the drive circuit. What occurs dynamically after a step is applied to the underdamped scanner is a position overshoot. By reducing the magnitude of the step called for appropriately, upon overshoot, the scanner will be at the desired position. At that instant full step voltage is applied and the galvanometer remains at the desired position. The galvanometer can be positioned in approximately one-half of the resonant period by this technique. Additional settling time will be required to adequately stabilize the galvanometer prior to recording a hologram. Experiments measuring the position stability of a deflected beam indicate a 5 ms settling time will be required for the test device.

We operated the General Scanning G-108 device driving a 6 mm square mirror to deflect the reference beam holographic memory system. We assembled this system at HEOC which simulates the test-bed system to check the BDC and hologram array devices being fabricated in the present program. We were able to record and reconstruct holograms following galvanometer deflection of the reference beam to the proper pad on the thermoplastic array and a 5 ms settling time.

2.4.4 Galvanometer Evaluation. - We have evaluated a General Scanning Instrument deflection system with a view to using such a system as a beam deflection unit in our optical memory system. The galvanometer deflection systems consists of a G 108 galvanometer and an RAX 100 drive amplifier. The system requires an analog deflection input voltage between -1 and +1 volts and a trigger input such that the galvo moves to a position corresponding to the analog input on the positive edge of the trigger input. The drive amplifier has a signal conditioning facility which can be set for optimum drive capability with minimum overshoot and undershoot.

RADIATION

Our evaluation of the General Scanning galvanometer system has been limited by the lengthy downtime we have experienced with the system. However, we have shown that it is possible to make holograms using the galvanometer as a deflection unit, with millisecond settling times. Shown below in Figure 2-13 is the setup we used to establish the minimum settling time necessary to allow for stable fringes before making a hologram. The monostable delays the opening of the shutter and was adjustable over a 1 to 10 ms range. Operation of the circuit is as follows: The deflecting galvanometer is first reset to some reference position. Then, the circuit is manually triggered so that the galvanometer mirror moves back to the desired position and at the same time the monostable starts timing out. At the end of the monostable period exposure is made. We found that setting up the drive-amplifier for optimum signal conditioning in the manner described in the instruction sheet it was possible to make holograms after a 2 ms delay.

Although this suggests that it is possible to make holograms after only a 2 ms settling period it should be noted that those measurements were made at only one deflection angle. Due to considerable operational problems with the deflection system, it was not possible to make repeated measurements at different deflection angles, but it had been noticed in the initial setting-up procedure that optimizing the drive-amplifier characteristics in the advised manner was good for one deflection angle only. At values of deflection angle other than the optimized value, the output was either underdamped or overdamped and one or two cycles of damped oscillation were observed. It can be assumed that this may increase the settling time in the worst-case out to approximately 5 ms.

To ascertain the deflection characteristics of the galvo system more directly we performed the following: Using a 44-mm lens to produce a 50 μ spot we observed the motion of the deflected spot by moving the spot through a 100 μ aperture in front of a photomultiplier tube. As in the hologram tests previously described, we set the spot to a reference position and then triggered the deflection circuits to bring the spot to a programmed position directly in the center of the 100 μ aperture. The output from the PMT was displayed on an oscilloscope and some typical responses are shown in Figure 2-14. Figure 2-14 shows the response of the drive amplifier and galvo to a 400 mV input signal with all signal
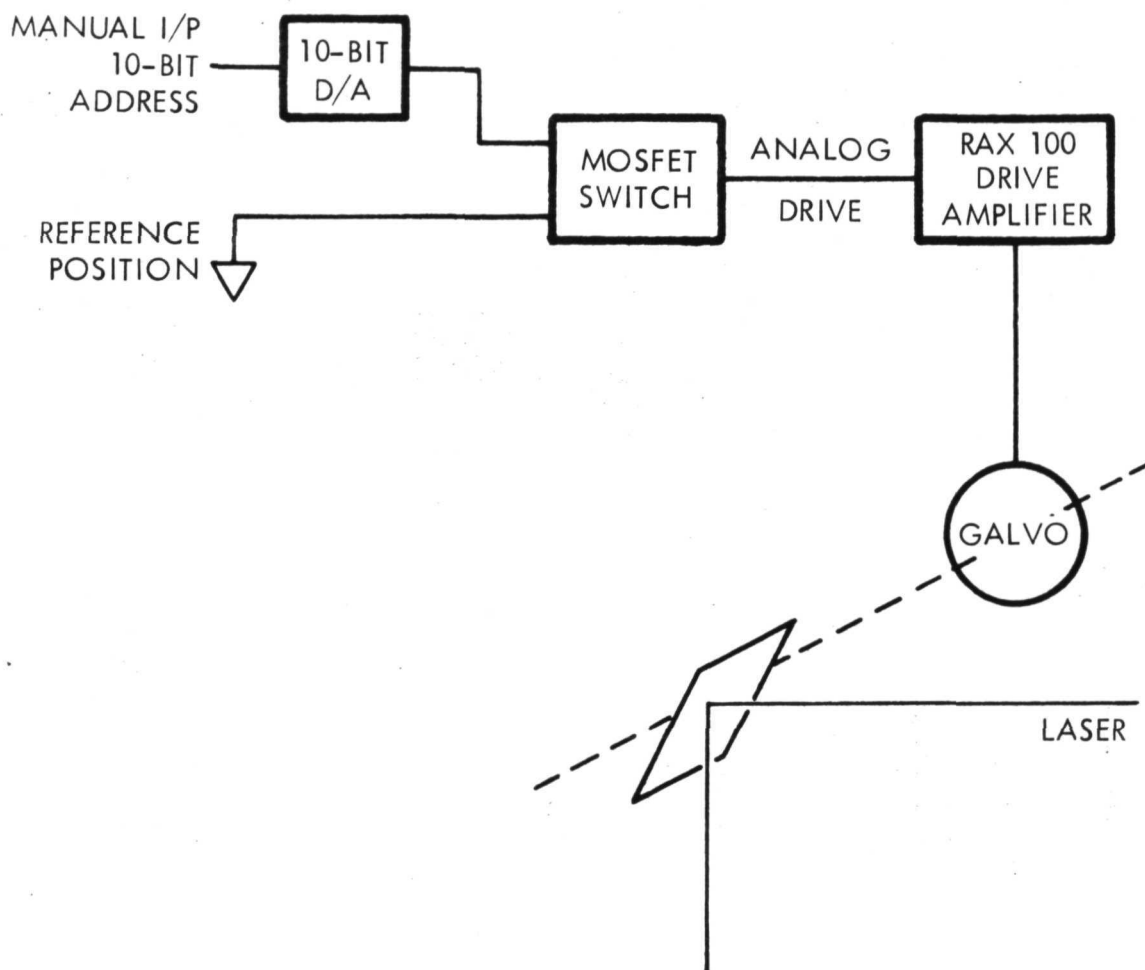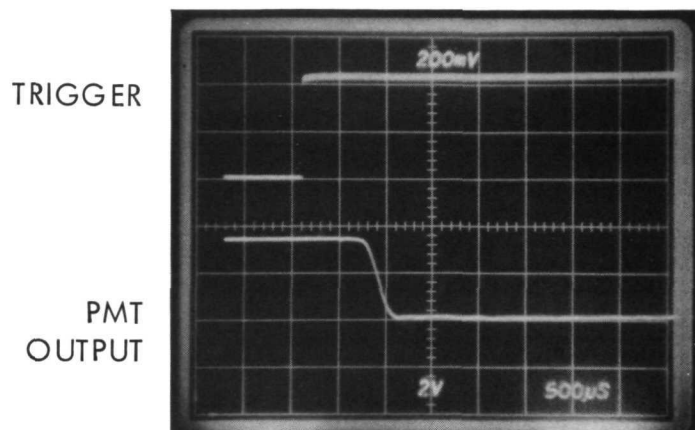
Figure 2-13. Galvanometer Drive System

RADIATION
A DIVISION OF HARRIS INTERTYPE CORPORATION

TRIGGER

PMT
OUTPUT

Figure 2-14a. V_{in} = 400 mV with Signal Conditioning and Optimum Damping
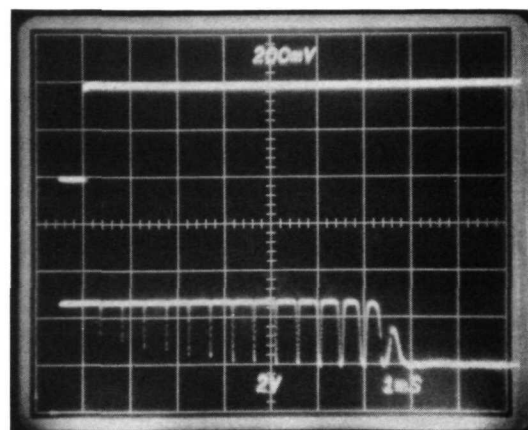

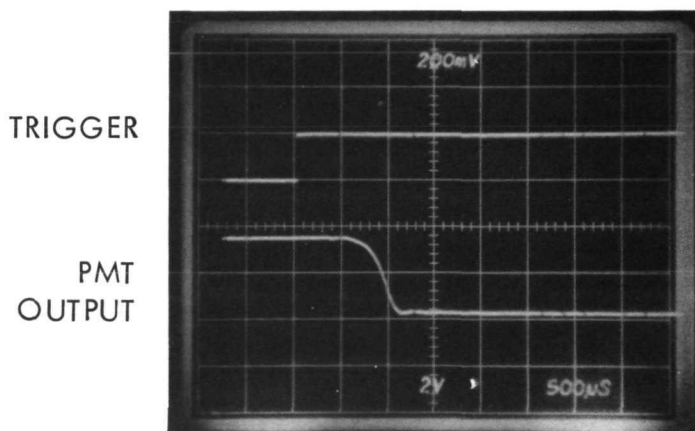Figure 2-14b. V_{in} = 400 mV with Optimum Damping Only

TRIGGER

PMT
OUTPUT

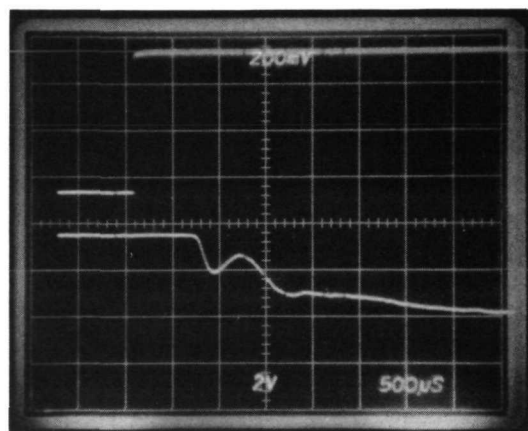Figure 2-15a. V_{in} = 200 mV with Signal Conditioning Optimized for V_{in} = 400 mV

Figure 2-15b. V_{in} = 600 mV with Signal Conditioning Optimized for V_{in} = 400 mV

conditioning and damping controls optimized. Figure 2-14a was taken with the trigger input applied whereas Figure 2-14b was without the trigger applied. Figure 2-15 was taken with 200 and 600 mV inputs but with the controls left as for the 400 mV input of Figure 2-14. Clearly, the controls are optimized for one deflection value only.

Our testing has shown that in principle it is possible to deflect a laser beam with a galvanometer such that no significant fringe motion occurs after 2 mS, when that laser beam is used in the making of a hologram. The General Scanning deflection system, however, needs considerable improvement in reliability and ease of operation before it can be considered for use in a holographic memory system.

2.5   HOE Device Signal Path Deflection

We investigated the use of a holographic optical element to implement the signal path deflection and increase the illumination efficiency of the system (see Figure 2-16). In the present breadboard the acousto-optic beam deflector deflects the laser beam only in the reference path. A 12 mm aperture laser beam is deflected angularly in x and y to the selected hologram location. The total AOBD angular deflection in y is approximately 2.8 milliradians for the 20 x 20 hologram array. After imaging by the telescope into a 1 mm aperture beam the total angular deflection increases to 33.6 milliradians and at a distance of approximately 91.5 mm from the focal plane of the telescope matches the profile of the hologram array. Because of the 30 degree offset angle in x selected for recording the holograms, the angular deflection for x is decreased by the factor cos 30 degrees at the AOBD to match the subtended angle of the hologram array.

We design the signal path deflection system to have the identical angular deflection at the HOE element as at the hologram array. The signal path telescope is fabricated identical to the reference path telescope and the identical angular throw is obtained by folding the optical path with a pair of mirrors.

The HOE element is fabricated to produce one out of a set of point sources on centers identical to the hologram array when illuminated by the 1 mm signal path beam.

RADIATION

The signal path optical s stem is modified by adjusting the interspacing of the lens set located between the HOE and the BDC to produce a 1:1 image from the HOE focal plane to the hologram array.

The differential of the number of reversals of the image for the signal and reference path to the hologram array are odd both in x and y. In order to obtain the proper number of reversals such that the signal and reference beams will track at the hologram array, we must insert a x and y reversal in either the reference or signal path. In Figure 2-16, we inserted a double reversing prism, an amici roof prism or paro prism, the offset in the optical path due to the prism can be compensated for during the reference beam alignment.

The efficiency of the HOE devices we have fabricated has been on the order of 60 percent. The major difficulty arises in fabricating the proper design. Devices fabricated during the program from dichromated gelatin materials have a high efficiency but the material thickness is difficult to predict after development. The recording angle during fabrication of the HOE device must be distorted to compensate for the effect of the gelatin expansion during development. Further, the final device must be protected from changes in humidity which will vary the device thickness and, therefore, the reconstruction angle required of the laser beam. We believe the experience gained during the program will allow us to fabricate devices, which can be sealed between glass plates to produce the stability, for the desired system configuration.

2.6   Investigation of Photodetector Arrays

We examined the performance of several Westinghouse phototransistor arrays. We tested a 10 x 10 array with an active area of 150 μm x 150 μm per transistor. The transistors are on 254 μm centers. We also tested two 32 x 32 bit phototransistor arrays having established the basic performance of devices we made some comparisons between the Westinghouse phototransistor array and the Reticon photo-diode array. Reticon photo-diode array, being
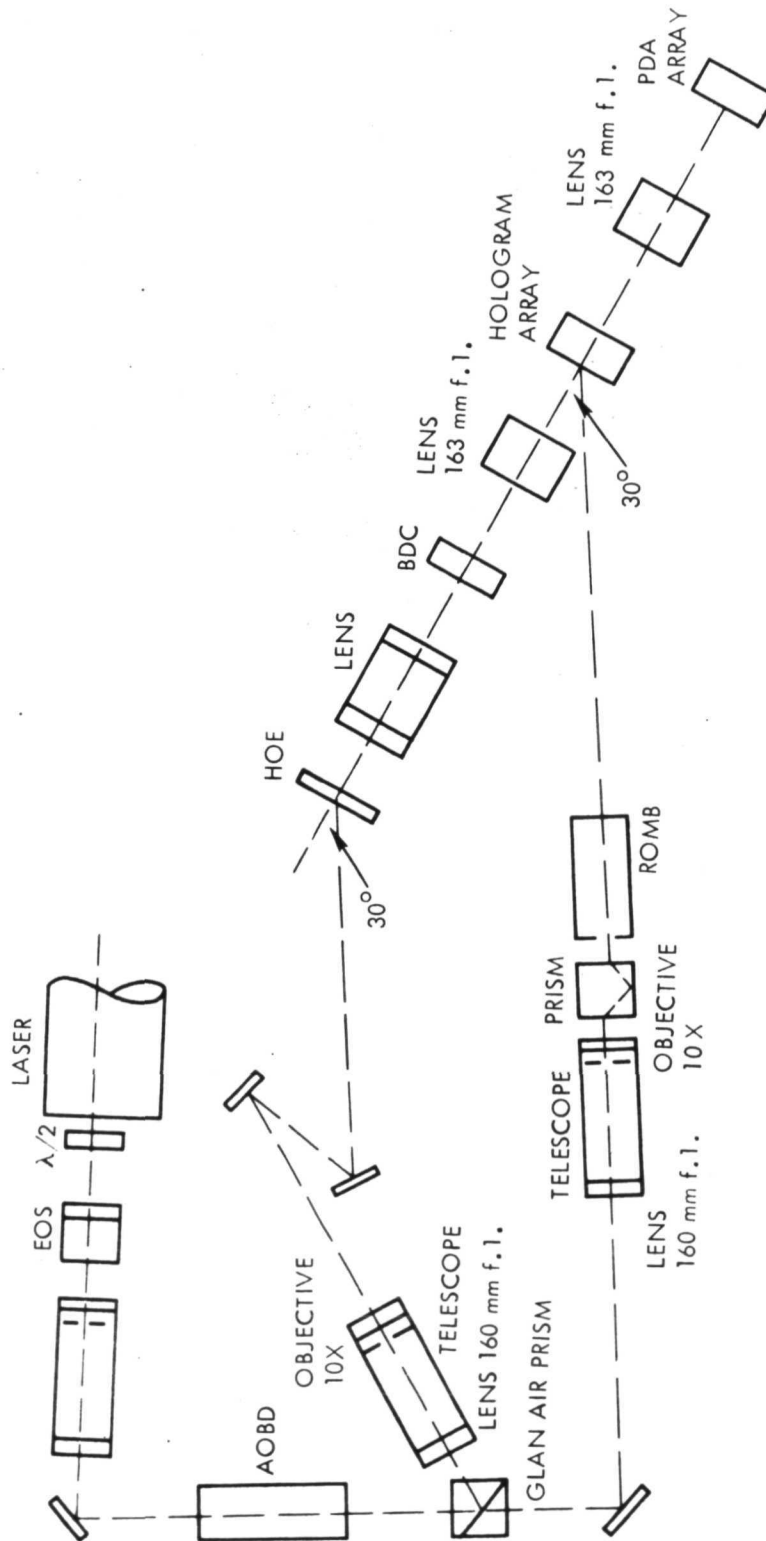
Figure 2-16. Breadboard Memory with HOE

a 32 x 32 bit array but on 102 μm centers, would require a redesign of the optic system (demagnification) to accept it. We first report on the theoretical operation of photo transistor and photo-diode arrays and provide test data from the 10 x 10 Westinghouse array using a linear Reticon array. Finally, we report on the test data obtained from the 32 x 32 arrays from Westinghouse and Reticon.

2.6.1 <u>Theoretical Predictions</u>. - It was shown in the Final Technical Report, Optical Read/Write Memory System Components,[5] that the behavior of a single photo-transistor, operating in the integration mode, is defined by the following expression:

$$V_{CB} = \frac{KIT_i}{C_{BC}} , \qquad (55)$$

where K is a linear constant depending on the efficiency of the transistor

base material,

I is illumination,

T_i is integration time,

C_{BC} is base-collector capacitor.

This implied that providing transistor β was high, β or load termination are not significant factors affecting output signal. It is to be expected, therefore, that output level is linearly related to integration time and illumination level only.

2.6.2 <u>Photosensitivity Plots</u>. - The sensitivity of each photosensitive transistor was established by evenly illuminating the array with a collimated beam and examining the output of a single transistor.

Figures 2-17 and 2-18 show the basic sensitivity of the device to both wavelengths ($\lambda = 632.8$ μm, $\lambda = 488$ μm). The output voltage prior to saturation is essentially linear with respect to both integration time "T_i" and illumination "I" as predicted from Equation (55). Also, from Equation (55), it is apparent that a tradeoff can be made between integration time and illumination, that is, for a constant output voltage, $I\alpha\,(1/T_i)$. This was plotted on Figure 2-19 which is a plot of I against $1/T_i$ for a constant output voltage of 50 mV. The output voltage of 50 mV was selected since this is the voltage threshold level of the sense amps in the NASA breadboard. Figure 2-19 can, therefore, be interpreted as the trade-off graph for illumination versus integration for the NASA system.

It will be seen that the original design illumination level of 20 nw/bit requires an integration time of only 0.3 ms, or alternatively by increasing the integration time to 3 ms, a tenfold increase in sensitivity can be achieved, so a sensitivity of at least 2 nw/bit should be realized from the new array at 632.8 μm.

2.6.3 Comparison with Photodiode Arrays. - We also considered the Reticon self-scanned photodiode linear arrays and made a comparison between the two arrays. The advantage of the photodiode array is that the Reticon array comes with its own MOS shift register in the same package as the array. The diode array we tested was only a line array, not an x-y matrix. Since the amplitude from the diode array is small, a charge amplifier is used to increase the output signal.

Any comparison between arrays has to include the following criteria: 1) Sensitivity, 2) Signal-to-noise ratios, and 3) Uniformity of sensitivity.

1. Sensitivity. - Figure 2-20 is a basic sensitivity plot for the self-scanned diode array and charge amplifier combination. Compared to the signal from the transistor array, Figure 2-17, the output of the diode array and amplifier combination is of the same order of magnitude despite the considerable gain of the amplifier.

RADIATION
A DIVISION OF HARRIS INTERTYPE CORPORATION
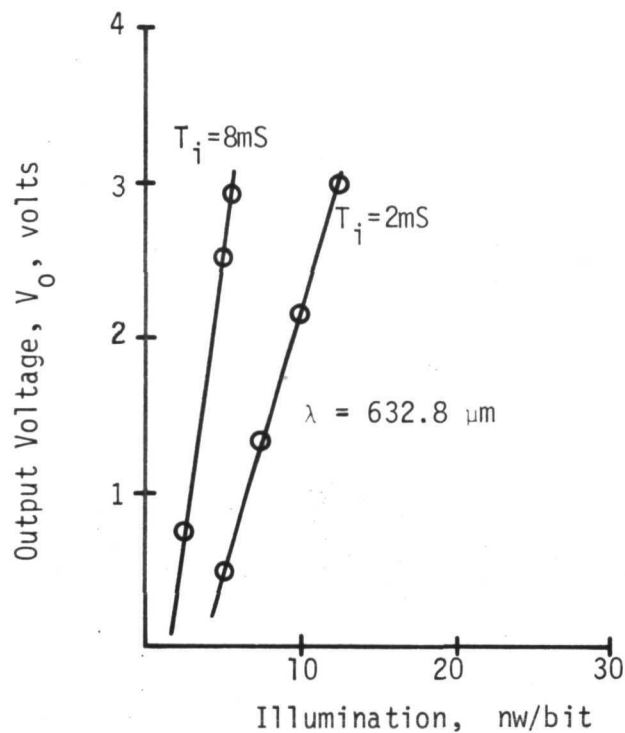
a) Output Voltage as a Function of Illumination
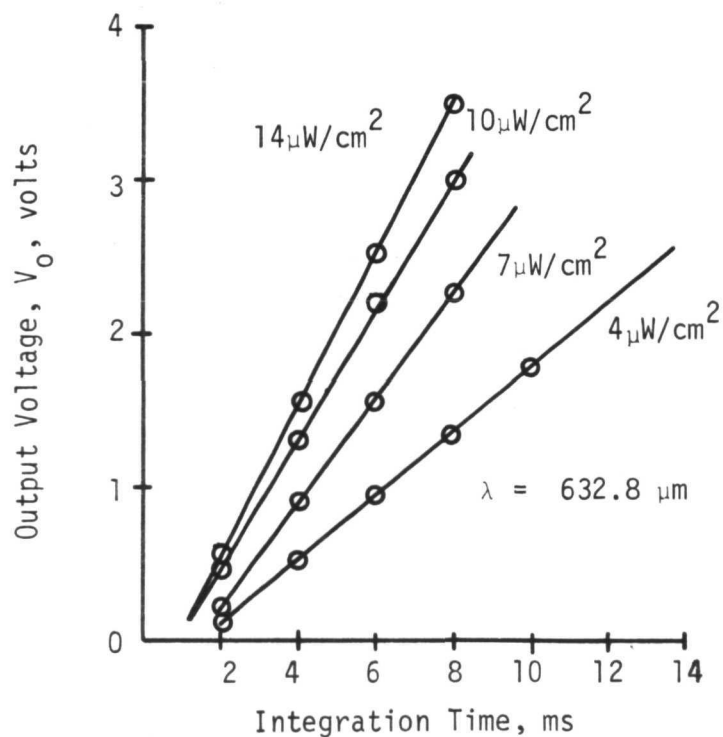
b) Output Voltage as a Function of Integration Time

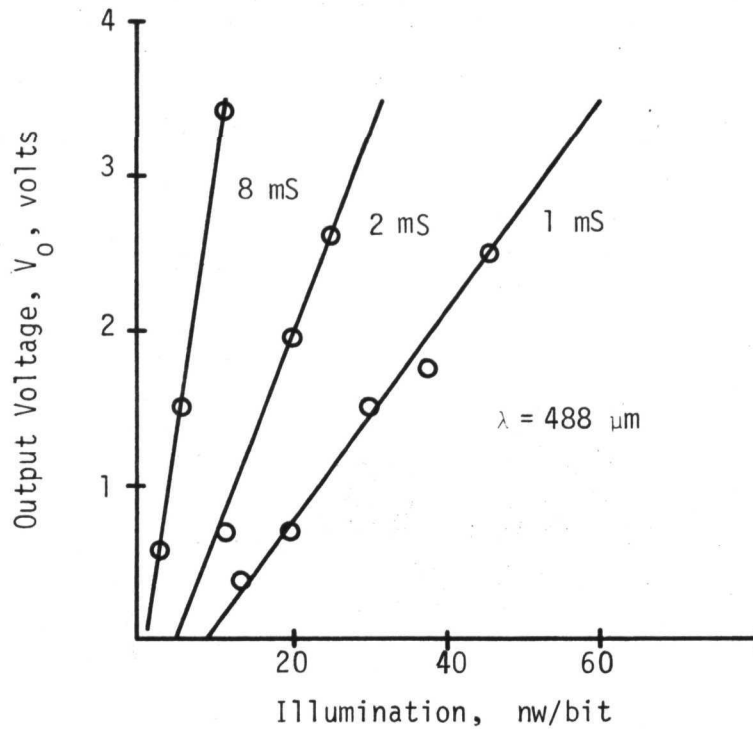Figure 2-17. Sensitivity Plots for Westinghouse Phototransistor Array

FIGURE 2-18. Sensitivity Plot for Westinghouse
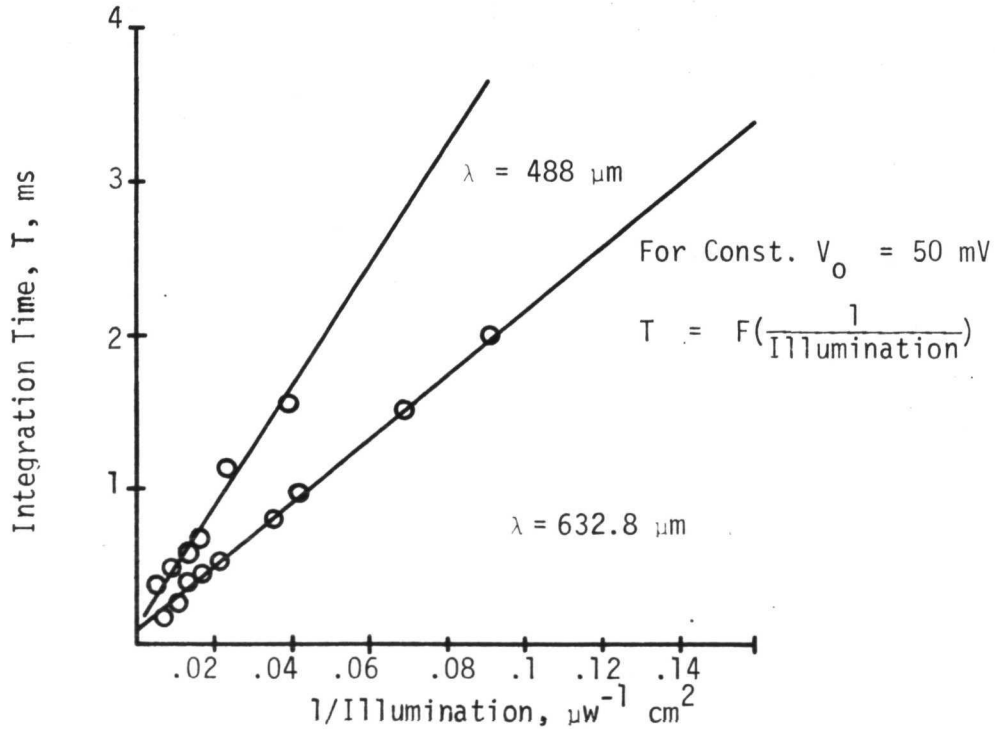Phototransistor Array
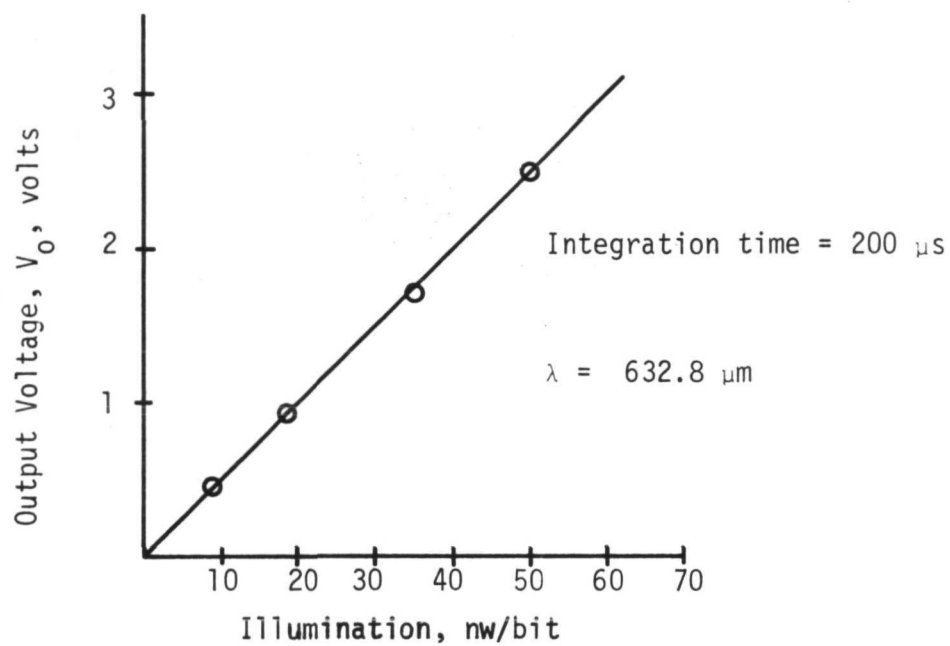

Figure 2-19.   Integration Time Required for 50 mV O/P

RADIATION
A DIVISION OF HARRIS INTERTYPE CORPORATION

Figure 2-20. Sensitivity of Reticon Photodiode Array

The photosensitive elements of each array may be modeled as shown in Figure 2-21. We assume the typical photosensitivity of each device to be 0.3 $\mu A/\mu$ watt and calculate a total charge of $Q = 0.3$ (I) x T_i coulombs collected either by C_{BC} for the phototransistor case or by C_P, the diode depletion layer capacitance, for the diode case. Therefore, for an illumination of 30 nw and an integration time of 256 μs, the charge collected in each case is 2.5 pico-coulombs. This is a very small charge and needs to be amplified. In the transistor array, amplification is through the transistor itself whereas in the diode array, amplification is through an external video amplifier. Both capacities C_{BC} and C_D are of the order of 2 pF, so some effect can be expected from the stray capacities.

In the transistor array, the β of the transistor acts as a buffer between the small C_{BC} and the external stray capacities. When the transistor is switched on, in the emitter circuit, the voltage appearing across the output resistor, neglecting the V_{BE} drop, becomes V_o β $C_{BC}/(C_{BC} + C_{strays})$. V_o is the voltage lost by the collector-base capacitance C_{BC} just prior to switch on due to the electron-hole-pair generation in the light sensitive area of the base. For large β, this voltage becomes V_o. The factor $(C_{BC} + C_{strays})$ can be established from the time-constant of the output waveform Figure 2-22. This gives $(\beta C_{BC} + C_{strays})$ > 1000 pF, and clearly since stray capacities are of the order of 10-20 pF, $\beta C_{BC} \gg C$. Thus, the output of the transistor array appears as a capacitive source approximately 1000 pF, and virtually no signal is lost.
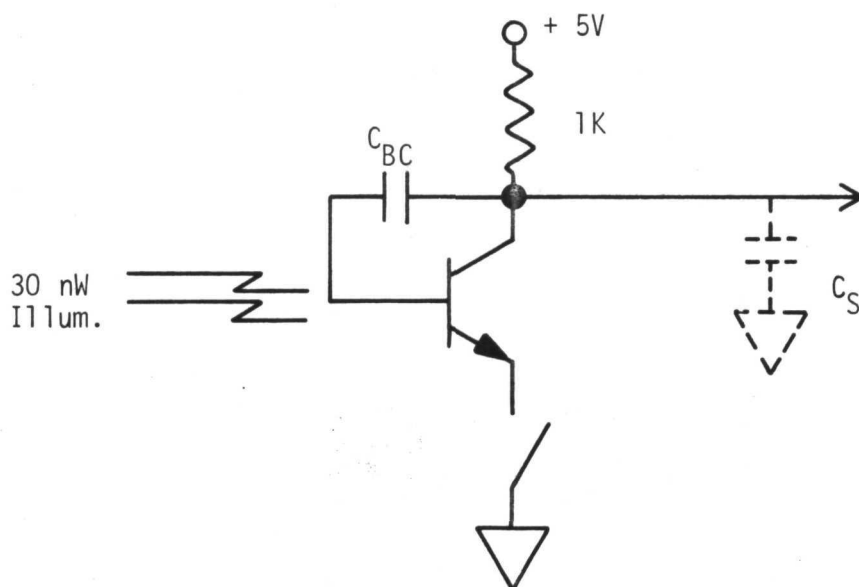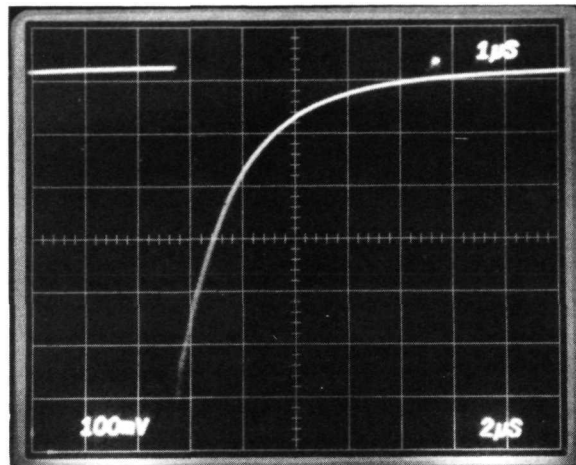
a) Single Photosensitive Transistor

C_D = depletion capacitance
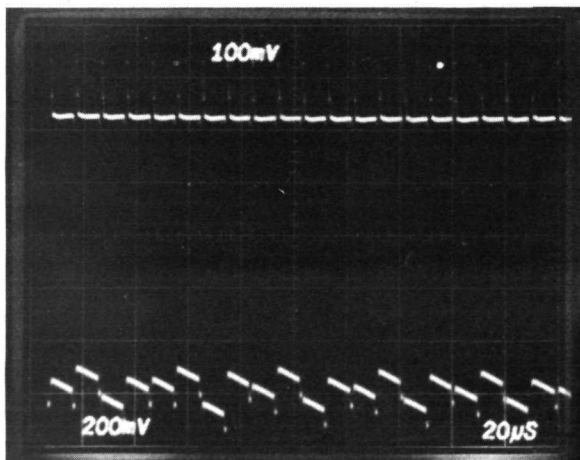C_S = stray capacitance
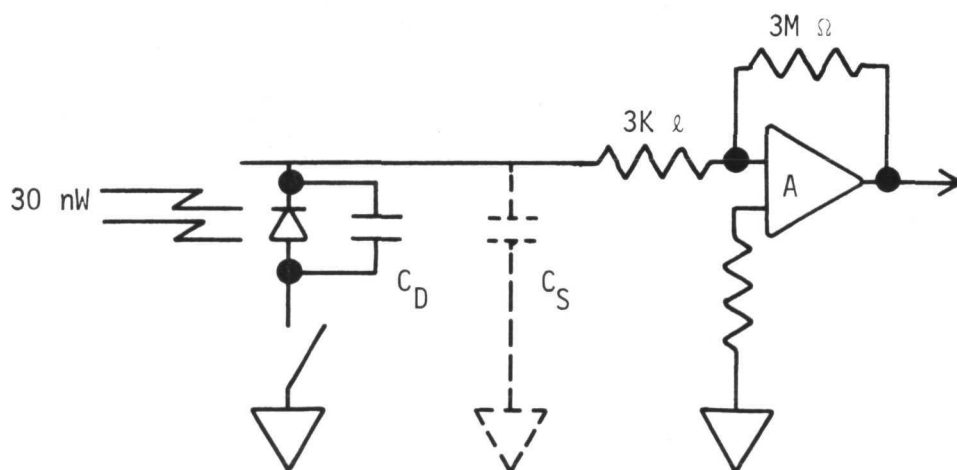
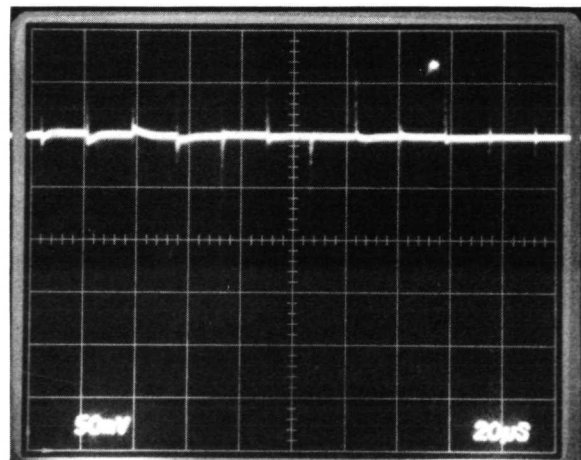b) Photosensitive Diode

Figure 2-21.   Photodetector Equivalent Circuits

(a) TYPICAL OUTPUT FROM WESTINGHOUSE PHOTOTRANSISTOR

PHOTODIODE ARRAY (LOWER TRACE)

PHOTOTRANSISTOR ARRAY

(b) NOISE LEVEL FROM TRANSISTOR AND DIODE ARRAYS

Figure 2-22. Signal-to-Noise Ratio Measurement

Illumination = 30 nW/Bit
Integration Time = 500 μs

RADIATION
A DIVISION OF HARRIS INTERTYPE CORPORATION

In the diode array, the small diode-capacitance is heavily shunted by the stray capacities but the charge amplifier collects the total charge and the diode array's video amplifier gain makes up for the gain inherent in the transistor array.

Clearly, both approaches exhibit good sensitivities at the light level of interest for holographic systems.

2. Signal-to-Noise. - There are many contributing factors to noise in the video output of both arrays. The main contributors are switching noise coupled through interelectrode capacities, and leakage resistors associated with the arrays. All these greatly outweigh the dark current associated with each photosensitive device. Of all these, capacitive effects are the most severe. In particular, the diode array suffers from a regular odd/even pattern due to capacitive differences between the two clock lines and the video line. It is possible to minimize this noise by differential weighting of the clock-lines, but it is not possible to eliminate the phenomena. Figure 2-22 shows the minimized odd/even pattern at the final output of Reticon's video processing circuit. For equivalent bit illumination intensities, the diode array had an effective signal-to-noise ratio of 8:1, whereas the Westinghouse was better than 50:1. These measurements were made at an illumination level equivalent to 30 nw/bit. Figure 2-22a shows the signal and noise levels for the transistor array for an integration time of 500 µs and illumination level of 30 nw/bit. The noise level is further compared with the equivalent noise level from the diode array in Figure 2-22b.

One reason for the superior Westinghouse performance is the β isolation, so that variations in stray capacities as well as the capacities themselves, have less effect. As was shown previously, the output charge of the photo-diode array video line is of the order of 2 pico-coulombs and a capacitance

of 2pF so any noise signals picked up will be amplified along with the signal in the video amplifier. In the transistor array, however, each transistor contains its own gain factor which isolates the collector base capacitance from the strays on the video line and the noise picked up on the output video lines is a small proportion of the signal. In the Reticon array, there are two clock lines for the shift register. The difference in capacity between these two lines and the video line accounts for the odd/even noise pattern on the output. Basically, the diode array system is more susceptible to noise than the transistor array system at the signal levels encountered in the NASA system, since the noise is introduced at a weak signal node in the diode array.

2.6.4   Uniformity of Sensitivity. - Uniformity of sensitivity is primarily a function of deflection layer capacities in both array systems. Measurements on both systems indicate that the diodes are more uniform than transistors but the degree of uniformity on the transistor array is better than 15 percent.

2.6.5   32 x 32 Photodetector Arrays. - We received two Westinghouse 32 x 32 bit arrays and one Reticon 32 x 32 bit array which were procured by NASA/MSFC. The Harris Electro-Optics Center had previously recommended that 32 x 32 arrays from Westinghouse and Reticon be evaluated and their level of performance as a component in the test breadboard established. The photosensitivity of the two arrays was measured for a uniform illumination with a wavelength of 514.5 nm. With an integration time of 6.5 ms, the Reticon array required 8 μwatts of illumination to saturate the photodiodes and the Westinghouse array required 40 μwatts of illumination to saturate the phototransistors. Considering that the Reticon array elements are on 102 μmeter centers with an effective aperture of 50 percent and the Westinghouse array elements are on 254 μmeter centers with an effective aperture of 70 percent, we calculate the bit sensitivity at saturation.

The Reticon array requires .4 nwat/element and the Westinghouse array 18 nwatts/ element to reach saturation during an integration time of 6.5 ms and an illumination wavelength of 514.5 meters. The Texas Instrument array presently in the breadboard requires over 300 nwatts for the same integration and illumination. We concluded during the initial testing that the variations in background or bias current for each element along a row were more significant in causing error during thresholding the output voltage (detecting the presence of a bit) than the random system noise. The major contributor to nonuniformities in the output voltage for the Reticon array was the odd/even pattern corresponding to the two-phase clock. In the Westinghouse array, a linear background slope was prominent which, we believe, results from the resistance of the array collector/ emitter bus lines. The majority of the background variations can be eliminated by proper driver and amplifier design.

We have tested both the Reticon and Westinghouse photodetector arrays and found that both arrays exhibit at least the minimum sensitivities required. The Westinghouse array was given somewhat more exhaustive tests for both signal-to-noise and sensitivity. The sensitivity plots are shown in Figure 2-23. The S/N measurements are defined as the following ratio: maximum illumination intensity to produce correct readout with no spurious "1's" to minimum illumination intensity to produce correct readout with no spurious "0's." During these tests, we imaged a 32 x 32 data pattern onto the array and examined the output of a single row, which was thresholded to give a 32-bit binary word. The maximum illumination limitation represents the noise level at which the first data "0" becomes a data "1," and the minimum illumination represents the sensitivity at which the first data "1" becomes a data "0" as represented in Figure 2-24. The noise so measured is a combination of system switching noise and photodetector dark current. We failed to reach the S/N value of 10 dB given by Westinghouse but came close with 8.5 dB. The S/N ratio is essentially independent of integration time (Figure 2-23).
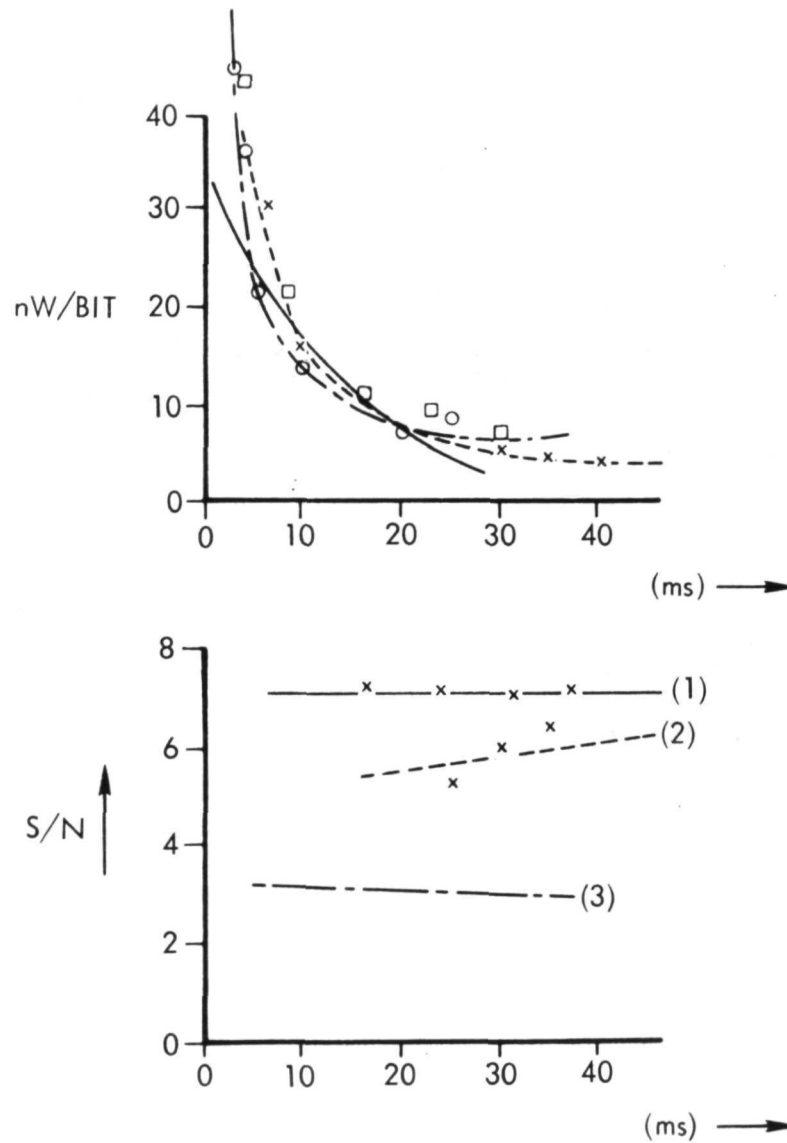
Figure 2-23.   Westinghouse Sensitivity and Signal-to-Noise Plots
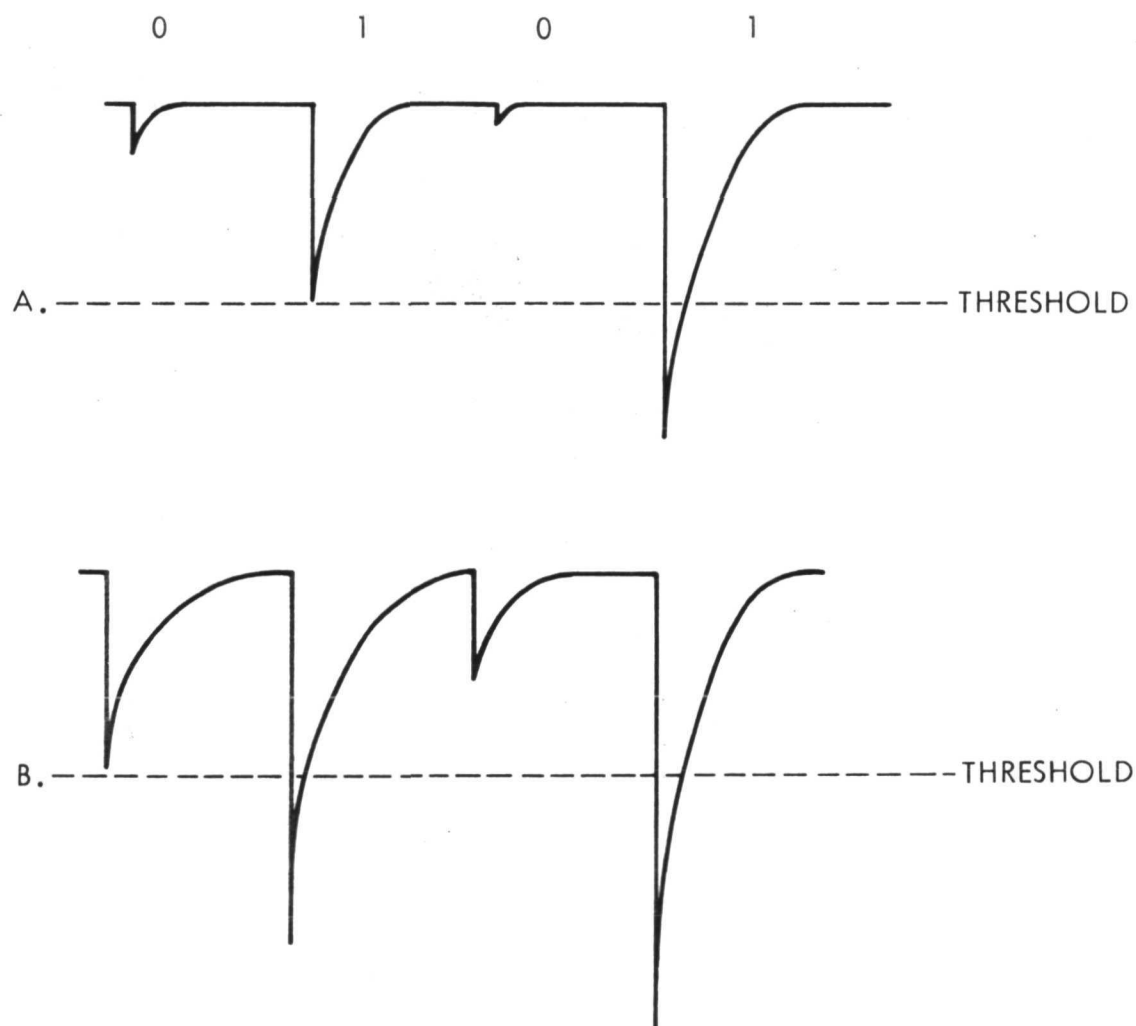(S/N Ratios (2) and (3) Indicate Imperfect Alignment)

Figure 2-24.   S/N Definitions

a.   Minimum Illumination to Produce Correct Readout with no Spurious "O"s
b.   Maximum Illumination to Produce Correct Readout with no Spurious "I"s

It appears that the Westinghouse transistor arrays are more than adequate in meeting the photodetector requirements of the present breadboard NASA system.

RADIATION

SECTION III
BLOCK DATA COMPOSER

The digital data is entered into the holographic memory system by a block data composer (BDC). The BDC provides a two-dimensional spatial array of successive blocks of data extracted from the input data stream. Each array of data spatially modulates a laser beam which is directed to a storage location where it interferes with the reference beam to form a hologram.

In this section, the BDC goals are reviewed and related to the results achieved during the contract. The large variation in the electro-optic properties and the availability of PLZT are discussed. A study of the parameters of the PLZT which most affect the performance of the BDC is recommended. The effects of polishing on the optical properties are shown and improvement in optical quality is noted. The procedures for fabricating PLZT BDC's are given for both Cr-Au and $IN_2O_3 : SnO_2$ electrodes. The number and types of BDC's fabricated during the contract are listed. The improvements seen in strain-bias devices from thicker Plexiglas substrates are mentioned and the suitability of Pyrex as a substrate for other types of BDC's is considered. A 32 x 32 element and 128 x 128 element BDC are shown. Other fabrication details, including device interconnections are mentioned. A study of four operational modes of the BDC - strain bias, edge effect, scattering and differential phase - is presented along with experimental data obtained from devices operating in these modes. An analysis of the edge-effect and differential phase modes is given in this section and an analysis of the scattering mode is given in Appendix A. The special electronics for testing 32 x 32 element BDC's that was constructed during the past contract are described along with the simplified holographic memory test system used. The most significant problems are reviewed and conclusions and recommendations are given.

RADIATION

A DIVISION OF HARRIS INTERTYPE CORPORATION

3.1 Review of Goals for BDC Performance

Constraints imposed by the overall holographic memory system and by the various devices within the system affect the BDC configuration and the BDC performance requirements. For example, the center spacings between BDC elements and the element dimensions are related to the size of optical components, to lens focal lengths, and to the size of each hologram in the memory. Also, the BDC must register with the PDA during readout. The contrast of the BDC affects the signal-to-noise ratio of the output data which is, in turn, related to bit error rates. The optical efficiency of the BDC affects the laser output power requirements. The switching speed of the light modulating elements in the BDC affects the input data rates at which the system can function. Switching voltage requirements impact the drive circuitry and power supply designs. These and other considerations strongly affected the particular configuration and performance goals established for the BDC at the inception of this program. The goals are summarized below:

1. Number of light modulating elements: $128 \times 128 = 16,384$

2. Center spacing between elements: 0.15 to 0.25 mm

3. Overall dimensions: 20×20 mm to 40×40 mm

4. Input bit rate: 10^6 bits/second

5. Contrast (Extinction ratio): 100/1

6. Optical efficiency: 30 percent

7. Peak switching voltage: ≤ 300 volts

During this program thirty-two 32×32 element BDC's with 1 mm center spacing and four 128×128 element BDC's with 250 µm center spacing were fabricated. With the special test electronics described in Paragraph 3.4, several of the 32×32 BDC's were composed at the rate of 120 µs/row for an effective input data rate of

$(32/120) \times 10^6 = 0.27 \times 10^6$ bits/second. Sections of 32 x 32 elements from one of the 128 x 128 BDC's were also composed at the same above rate of 120 μs/row; the effective data rate achievable is therefore $(128/120) \times 10^6 = 1.07 \times 10^6$ bits/second. Higher rates are achievable with increased switching voltage and lower electrode sheet resistance.

Local contrasts of greater than 50/1 have been measured in the 32 x 32 element BDC's after optimizing the strain-bias level for the region of the array under investigation. Thickness and compositional variations in the PLZT plate cause the optimum strain-bias levels to vary over the full BDC aperture. Lower contrast ratios of 20 to 1 have been achieved over a 9 x 9 section of a 32 x 32 BDC and a more uniform composition of the material should give a more uniform response of the PLZT to strain-bias. The problem of polishing PLZT plates to achieve more uniform thickness has been considered in detail on this program. Improvements have been made but more effort is required to completely solve the uniform thickness problem.

The optical efficiency of modulating elements in the Plexiglas-PLZT structure with chromium-gold (Cr-Au) transparent electrodes (80 to 100Å of gold) is typically 10 to 15 percent (excluding the absorption losses in the polarization analyzer). Tests with 32 x 32 element BDC's with sputtered In_2O_3: SnO_2 electrodes showed an optical efficiency in excess of 30 percent.

Switching voltages for the 32 x 32 element BDC's are typically 180 to 250 volts for 200 μm thick PLZT discs. The drive circuitry design permits levels up to 300 volts.

In summary, the fabrication, optical efficiency, and input data rate goals have been met, but the goal of contrast ratio has not been met. The contrast ratio of the BDC will be dependent greatly upon uniformity of the electro-optic properties of the PLZT which have shown wide variation. A study of the parameters of the PLZT that most affect the performance of the BDC and possibly the operation of the BDC in another mode, such as the differential phase mode, should result in the contrast ratio goal being met.

3.2   Materials and Fabrication

The PLZT discs used in fabricating the BDC's were obtained primarily from Honeywell Ceramics Center. These were of the composition 7/65/35 indicating $PbZrO_3$ and $PbTiO_3$ in a 65 to 35 ratio with 7 atomic percent doping of La.[6,7] A total of 60 discs, with diameters from 2-1/8 to 2-1/4 inch, both polished and unpolished, were received, of which 47 were refractive index change mode materials (grain size $< 2.5\ \mu m$) and 13 were scattering mode materials (grain size $< 4.0\ \mu m$). A major difficulty in this contract has been that the majority of the discs received were not of high quality. However, we continued to fabricate devices from PLZT of lesser quality which had inclusions, discolorations and nonuniform grain size and porosity.

The material we have received in the past from our supplier has steadily increased in quality from the first samples received three years ago. The original material, hot pressed from mixed oxides (MO-HP), was changed to oxygen hot pressed (MO-OX-HP) with a marked increase in quality. Out supplier (Honeywell) has changed to the chemically co-precipitated, oxygen hot pressed material (CP-OX-HP) with which Sandia has achieved high uniformity, and contrast ratios of better than 100 to 1. However, Honeywell has not completely refined its techniques to the point where the new material is the equivalent of their older MO-OX-HP material. We have discussed this and other problems of PLZT with Honeywell and also with Sandia, the discoverers of the electro-optical properties of lanthanum doped PLZT ceramics. In Sandia's opinion, there is no fundamental problem in producing PLZT by the CP-OX-HP process, equal in quality to the material they reported more than two years ago. The quality of the Sandia CP-OX-HP material would exceed our current quality requirements. Honeywell has increased its staff and funding for PLZT production within the last year and we expect the PLZT to continue to improve in overall quality.

In the last few weeks of the program, 13 discs of 7/65/35 PLZT of three different grain sizes were obtained from Sandia Laboratories. Complete data sheets on each group of material were also obtained from Sandia listing the electrical properties of the PLZT. However, there was not sufficient time to completely evaluate the electro-optical performance of this material. During the past contract, we have strongly felt the lack of information on the physical and electrical properties of the Honeywell material to correlate with the data from the electro optic testing of BDC's. The optical and electro optical properties of the PLZT have varied greatly over the various shipments received leading us to believe the composition and electrical properties were different for each batch. Several discs were sent for spectrographic analysis; the results indicated variations in the lanthanum and lead concentrations. However, the reliability of these tests is in question. Our experience with electro-optic testing of BDC's leads us to believe that a program of testing is necessary to establish the parameters of the PLZT which most influence the performance of BDC's and to establish the allowable variations of these parameters for maximum performance of BDC's. Once these parameters can be identified, then commercial suppliers of PLZT can adjust their processes accordingly to meet the specifications.

The unpolished discs of PLZT that we have received were ground and polished to thicknesses of 175 to 200 μm for the refractive index change material and 230 to 380 μm for the scattering mode material. Some of the discs were polished in our own shop, but during the last half of the contract, almost all discs were polished by an outside firm, Statek, Inc. Their polishing results have improved greatly over the year, and are now equal to, or better than, our own optical shop. The optical quality of each polished disc was checked by 1) examination between crossed polaroids in white light, 2) examination by reflected monochromatic light, and 3) examination in transmission in collimated monochromatic light. The first test reveals strain patterns from saw marks, polishing, pullouts, and scratches, and also shows nonuniformities in coloration (i.e., compositional

nonuniformities). The second test reveals thickness variations by the number and shape of the interference fringes caused by light reflecting from the front surface and the back surface of the disc. Thickness variations that will affect the performance of BDC's are revealed in much more detail by the third test in collimated monochromatic light. Results of such tests for four different polished discs are shown in Figure 3-1. The disc in Figure 3-1a was polished in our own optical shop, the disc in Figure 3-1b by Honeywell and the last two by Statek. Figure 3-1c shows the effects of waxing the PLZT disc down on a metal block with a grid pattern during polishing. Figure 3-1d was waxed down on a smooth block for polishing. The lensing effects are due to variations in the last surface of the PLZT to be waxed down and are caused by wax buildup under the PLZT. We have discussed this problem with Statek, and they have resolved this problem some-what and are trying other adhesives, such as thermoplastic, to hold the discs for polishing.

A procedural block diagram which traces the fabrication steps for BDC's with both vacuum evaporated electrode patterns and photoresist-etch formed patterns is presented in Figure 3-2.

The PLZT plates are always annealed in air at 650°C after polishing and, in some cases, before polishing. The post-polish annealing step is essential to relieve the stresses induced during the grinding and polishing. The prepolish annealing step may improve the PLZT uniformity slightly; comparative data on devices with and without prepolish anneal-ing are inconclusive. During the annealing operations, the PLZT is held at 650°C for at least one hour with heat-up and cool-down times of 3 to 5 hours.
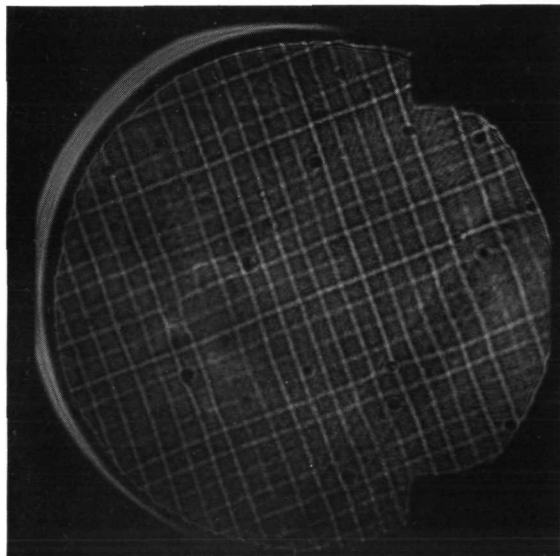
The PLZT plates are cleaned prior to electroding with hot solvents (trichlorethylene, acetone, and isopropyl alcohol), hot Liquinox detergent, and multiple deionized (DI) water rinses. Transparent electrodes on most BDC's fabricated in the first half of the contract were chromium-gold layers vacuum deposited through thin metal masks.
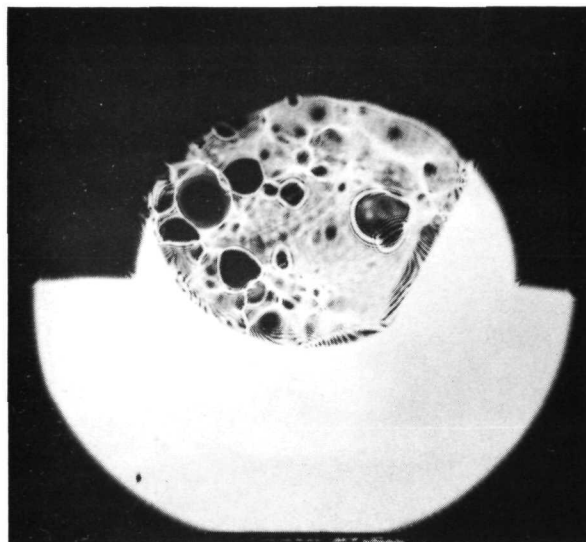
(a)
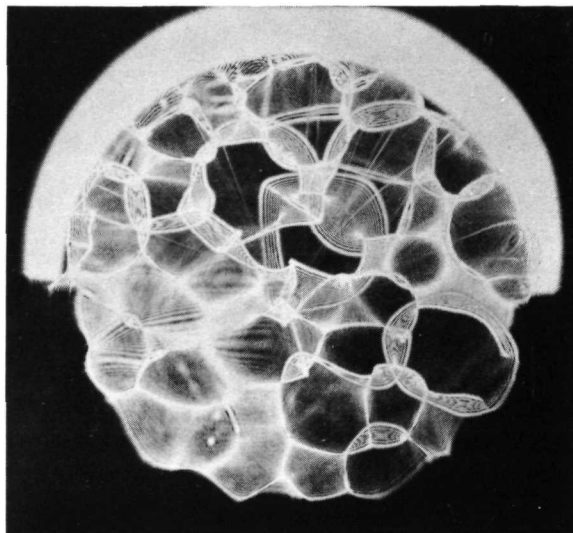
(b)

(c)

(d)

Figure 3-1. Polished Discs of PLZT Viewed in Transmission One Meter Distant
From the Sample. Note: Discs Partially Obscured by Sample Holder.
Polished By: a) Radiation, b) Honeywell, c) Statek (with Grid
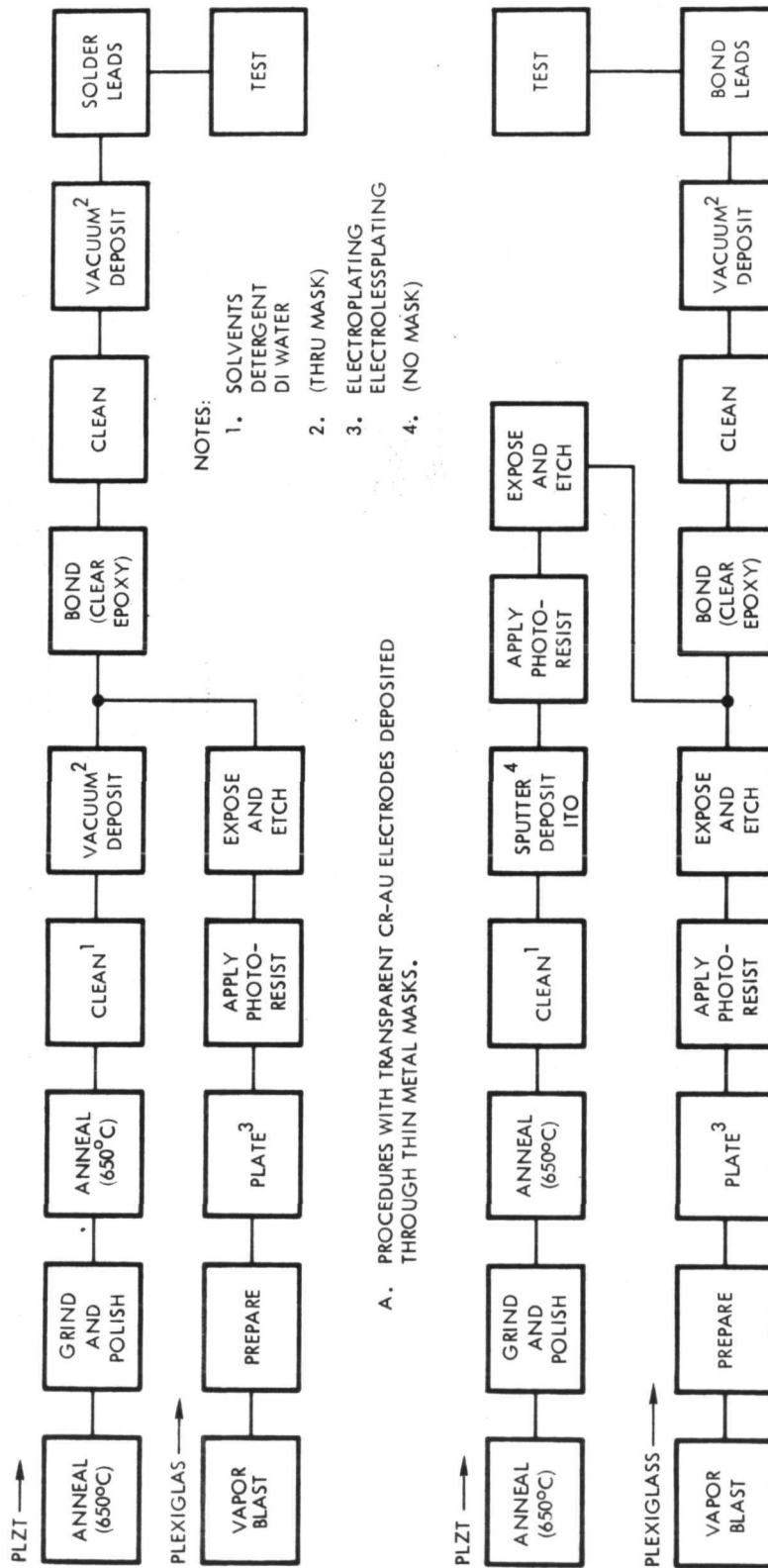Plate) and d) Statek (with Flat Plate).

RADIATION
A DIVISION OF HARRIS - INTERTYPE CORPORATION

NOTES:

1. SOLVENTS
   DETERGENT
   DI WATER

2. (THRU MASK)

3. ELECTROPLATING
   ELECTROLESSPLATING

4. (NO MASK)

A. PROCEDURES WITH TRANSPARENT CR-AU ELECTRODES DEPOSITED THROUGH THIN METAL MASKS.

B. PROCEDURES WITH TRANSPARENT ITO ELECTRODES FORMED BY PHOTORESIST-ETCHING PROCEDURES.

Figure 3-2. BDC Fabrication Procedures

Typically, only one PLZT face is electroded prior to the epoxy bonding step. The PLZT is bonded to the Plexiglas substrate with DER 332 clear epoxy at 70 to 75°C for 48 hours at a pressure of 100 to 200 psi. The excess epoxy is then stripped from the exposed PLZT face (with methylene chloride followed by detergent and DI water rinses), and the other set of electrodes is deposited through an appropriate thin metal mask. Several of the devices fabricated in the last half of the contract had transparent electrodes of sputter deposited In_2O_3 doped with 9 percent SnO_2 (ITO). These sputtered films had thicknesses between 4500Å and 6000Å with sheet resistivities of 40 to 150$\Omega/\Box$. For the BDC's made with ITO electrodes, the electrode pattern on both sides of the disc was defined and etched, using photoresist techniques. The ITO electrodes were etched with a 1 to 1 solution of concentrated hydrochloric and acetic acids at 75°C. The fabrication procedure shown in Figure 3-2b was then followed for these devices.

For both types of transparent electrodes, thicker opaque electrode strips are deposited through masks on each PLZT face at the end of the transparent electrodes. The thicker electrodes on the PLZT underside mate with similar thick electrodes on the Plexiglas during the bonding step to provide electrical access to the underside electrodes. This procedure has largely overcome the problem of loss of electrical contact to these electrodes. In recent devices, access to more than 95 percent of the elements has been noted; the dropouts were a result of breaks in the transparent electrodes or of PLZT cracks and were not related to poor contact in the mating regions.

The mating thick electrode patterns on the Plexiglas are formed with photoresist-etching procedures, in both cases. Problems of electrode adherence on Plexiglas were overcome by lightly vapor blasting the Plexiglas surface (with the optical aperture region protected) and using the electroplating and electroless plating techniques followed by photoresist-etching.

Indium solder is used to attach gold wire leads from the PLZT top face to the thick metallic electrodes on the Plexiglas. Heavier insulated leads are soldered to the relatively thick electrodes on the Plexiglas and wire-wrapped to the connectors. Wire bonding techniques for finer patterns (such as 128 x 128 on 10 x 10 mil centers) must be used. Ultrasonic approaches are applicable for bonding to the electrodes on the PLZT and the Plexiglas, but care must be taken not to pull the thicker Cr-Au electrodes from the substrate after bonding.

The Plexiglas substrates used in the BDC's have been changed from 3.12 cm to 6.25 cm thick. The result has been less strain in the PLZT plate due to the fabrication process and a more uniform operating strain-bias. For BDC's other than the strain-biased type, 3.12 cm thick Pyrex has been tested as a substrate. Vapor blasting is used to increase adhesion of the electrode lines. Problems occur with residual birefringence in the Pyrex plates, thus Pyrex cannot be used for edge-effect mode devices, but may be used for scattering mode and differential phase mode BDC's.

A total of 36 BDC's have been fabricated during this contract. Of these, 32 were 32 x 32 element BDC's on 40 mil centers and 4 were 128 x 128 elements on 10 mil centers. Four of the 32 x 32 and two of the 128 x 128 element devices had ITO electrodes. Four of the 32 x 32 BDC's were fabricated on Pyrex substrates. Three of the 32 x 32 BDC's were scattering mode devices, and the remainder were index of refraction change devices.

In Figure 3-3 is shown a 32 x 32 element BDC on a Plexiglas substrate and a similar device on a Pyrex substrate is shown in Figure 3-4. A 128 x 128 element BDC with ITO electrodes is shown in Figure 3-5. Figure 3-3 also shows a new type of pressure pin connector which eliminates the soldering of the wire-wrap terminal wires to the substrate electrodes and allows the BDC in the strain-bias mount to be changed easily.
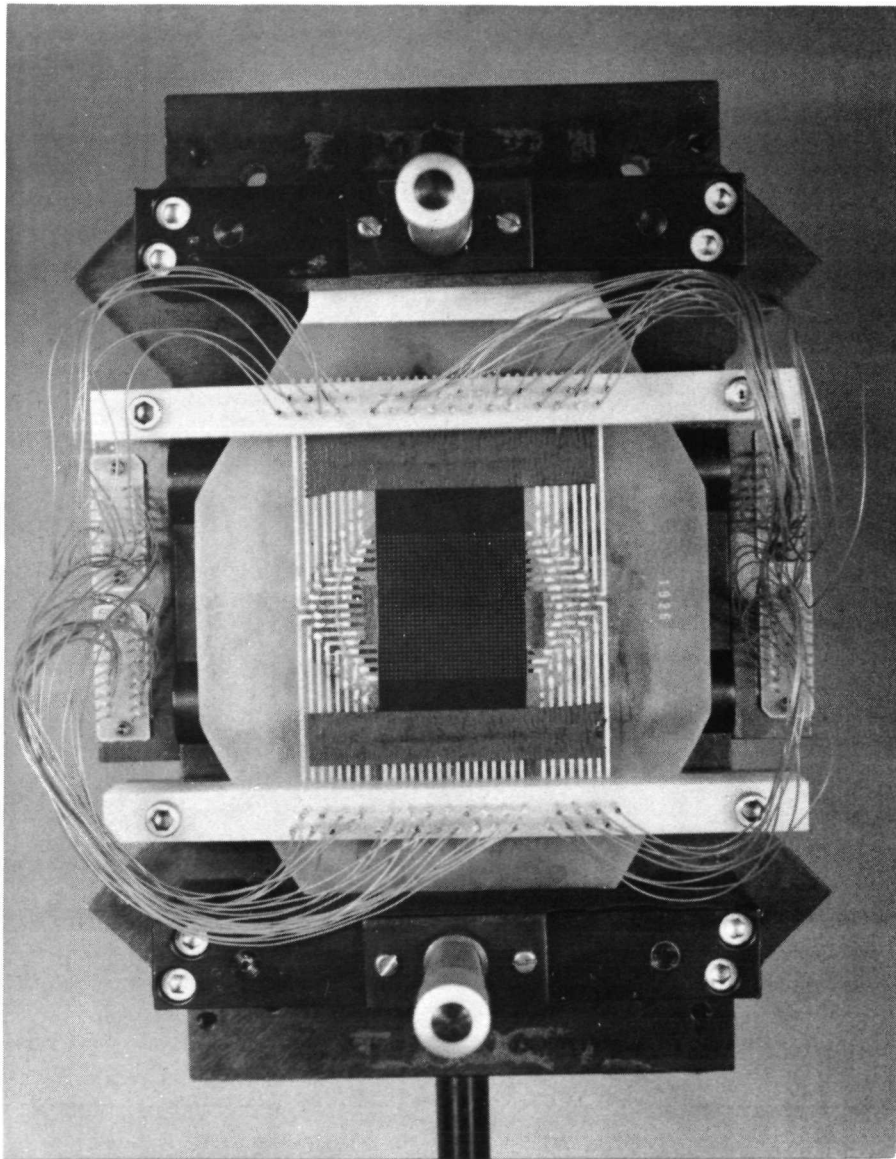
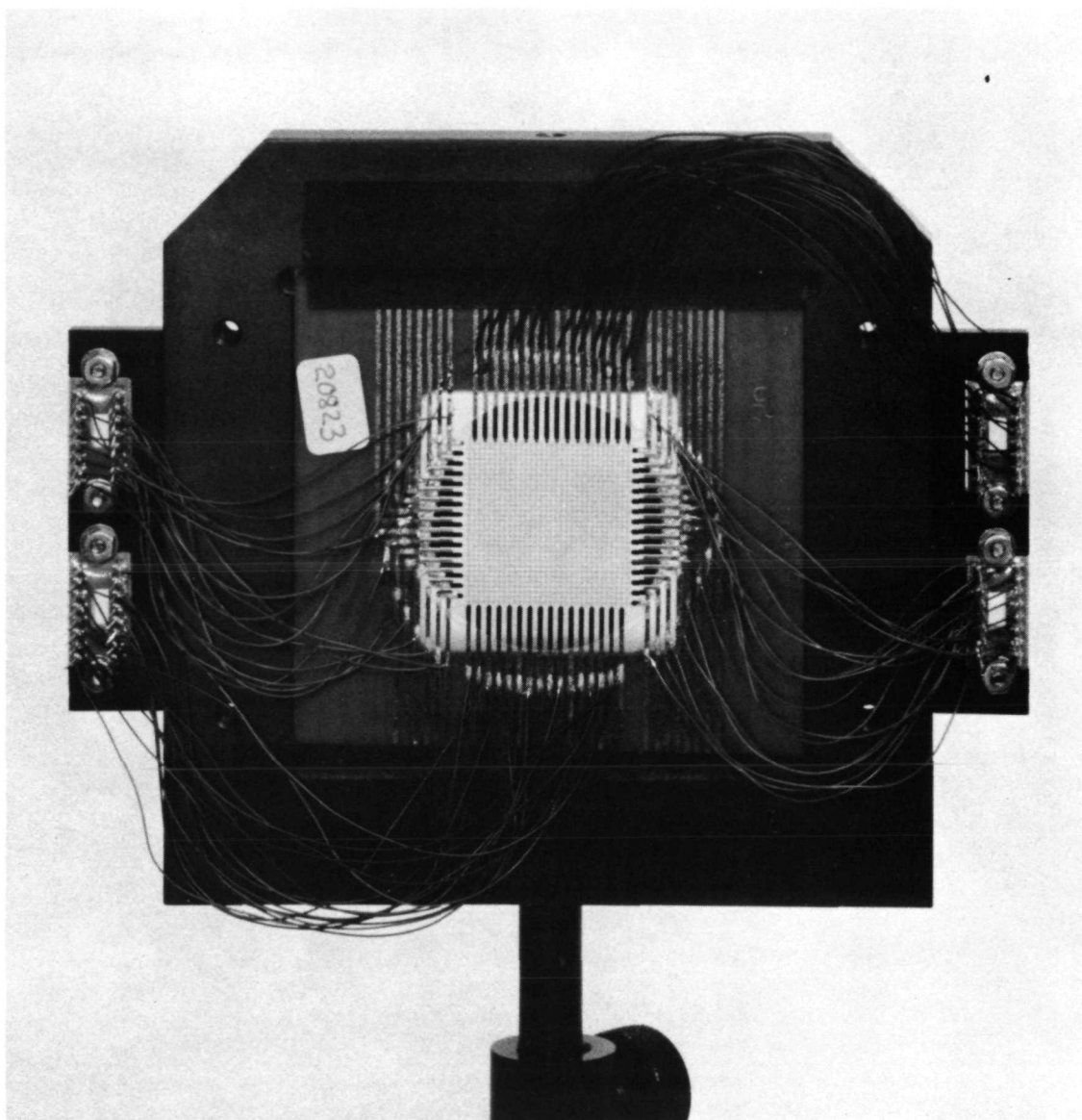Figure 3-3.   32 x 32 Element BDC on Plexiglas Substrate

RADIATION
A DIVISION OF HARRIS INTERTYPE CORPORATION

Figure 3-4.   32 x 32 Element BDC on Pyrex Substrate
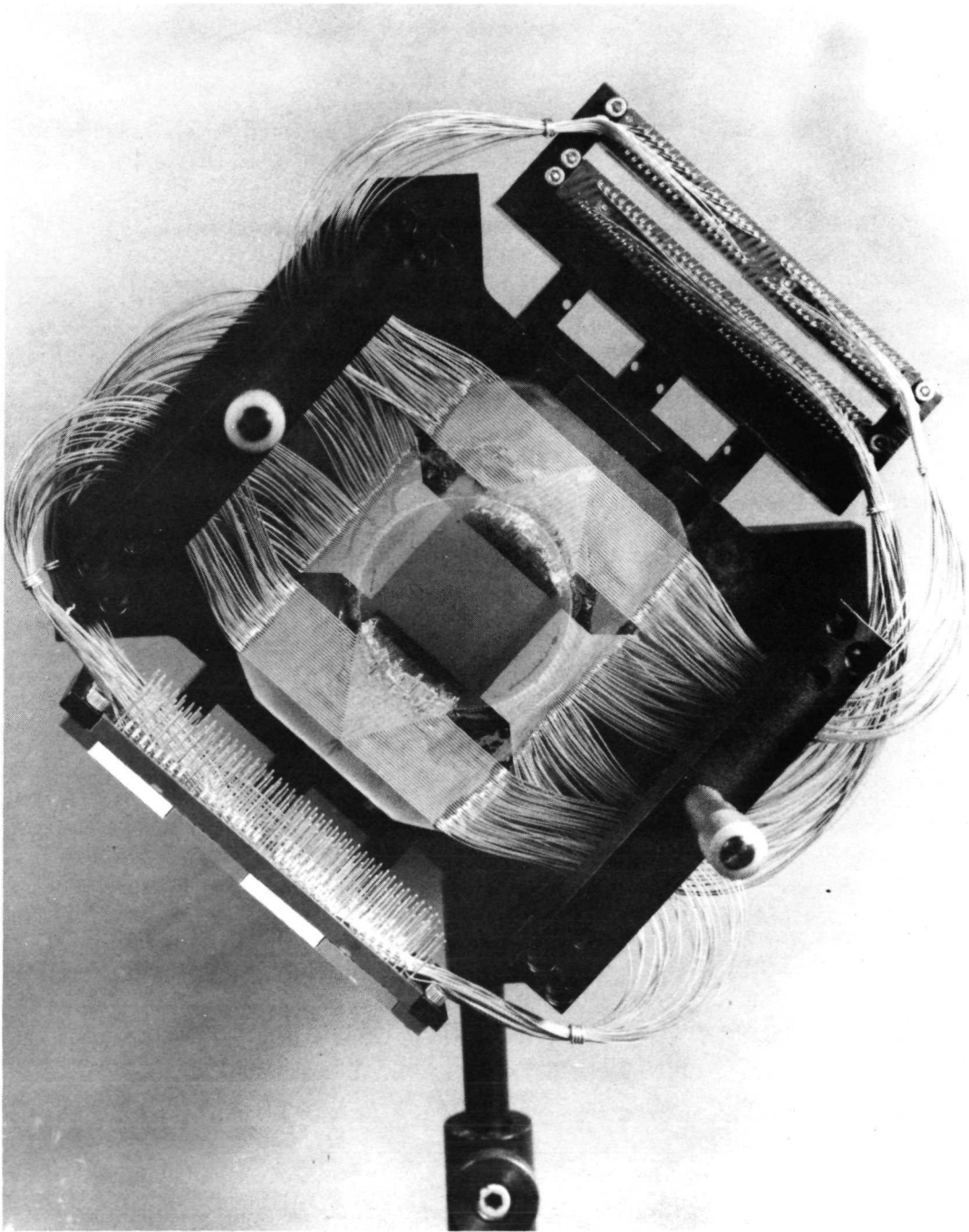
Figure 3-5.   128 x 128 Element BDC on Plexiglas Substrate

RADIATION
A DIVISION OF HARRIS INTERTYPE CORPORATION

3.3 Operational Modes

The operation of PLZT BDC's in strain-biased, scattering, edge-effect and differential phase modes will be discussed in this section and comparisons made among the modes.

All four of the modes share a common electrical switching technique. The switching of the matrix elements between "1" and "0" states is done by a modified "voltage control" method[8, 9] illustrated in Figure 3-6. The states are: "1" - electrically poled to saturation polarization, P_S, and the electric field reduced to zero whereupon P_S goes to P_r (remanent polarization), and "0" - electrically depoled to $P_r \approx 0$. We have modified the method by first switching all elements to $+P_r$ and then to $-P_r$ before depoling to the "0" state. The pulses shown in Figure 3-7 are for Reset (depoling the entire matrix to "0's"), Write "1" (full select) and Write "0" (half-select). Pulse widths of 0.1 to 10 ms have been used. This switching method has shown a greater resistance of the "0" state to half-selects than the original method. Half-select resistance has not been a problem for the 32 x 32 element or 128 x 128 element devices but the contrast ratio obtainable is lower than for a single element device since the polarization may not completely saturate for a "1" state in a matrix device.

Strain-Biased Mode. - The strain-biased mode of operation has, until recently, been the principal mode investigated for PLZT BDC's.[10, 11] In this mode, each of the elements acts as an electro-optic amplitude modulator when the BDC is placed between crossed polarizers. Strain-bias applied to the BDC changes the birefringence of the PLZT and can be varied to make either the "1" or "0" state transmitting (or opaque). Switching an element from the "0" to the "1" state also changes its birefringence and its transmittance. The operation in the strain-biased mode is illustrated in Figure 3-8 and a means of varying the strain-bias is shown in Figure 3-9.[10] A 32 x 32 element strain-biased BDC is shown in Figure 3-3.
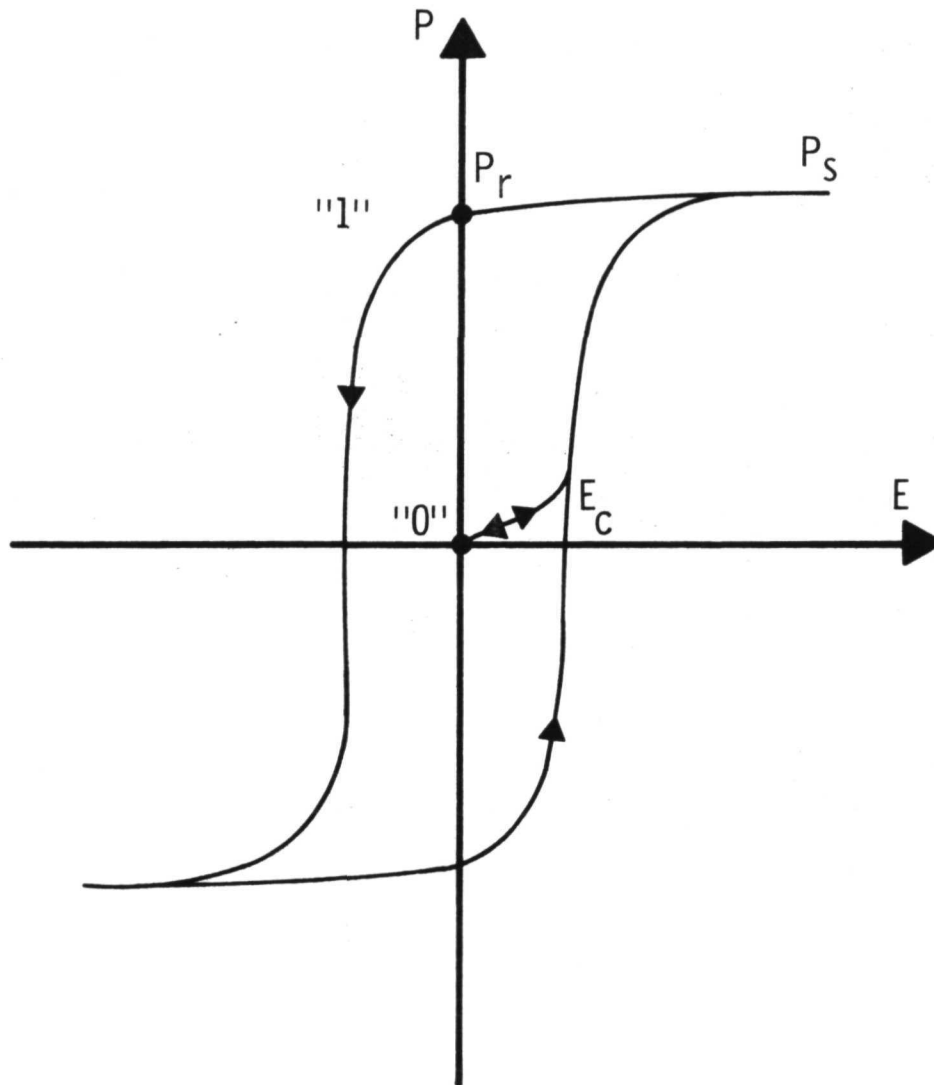
Figure 3-6. Polarization as a Function of Electric Field
For PLZT Ceramics Illustrating Memory Type
Operation Between the "1" State (Poled) and The
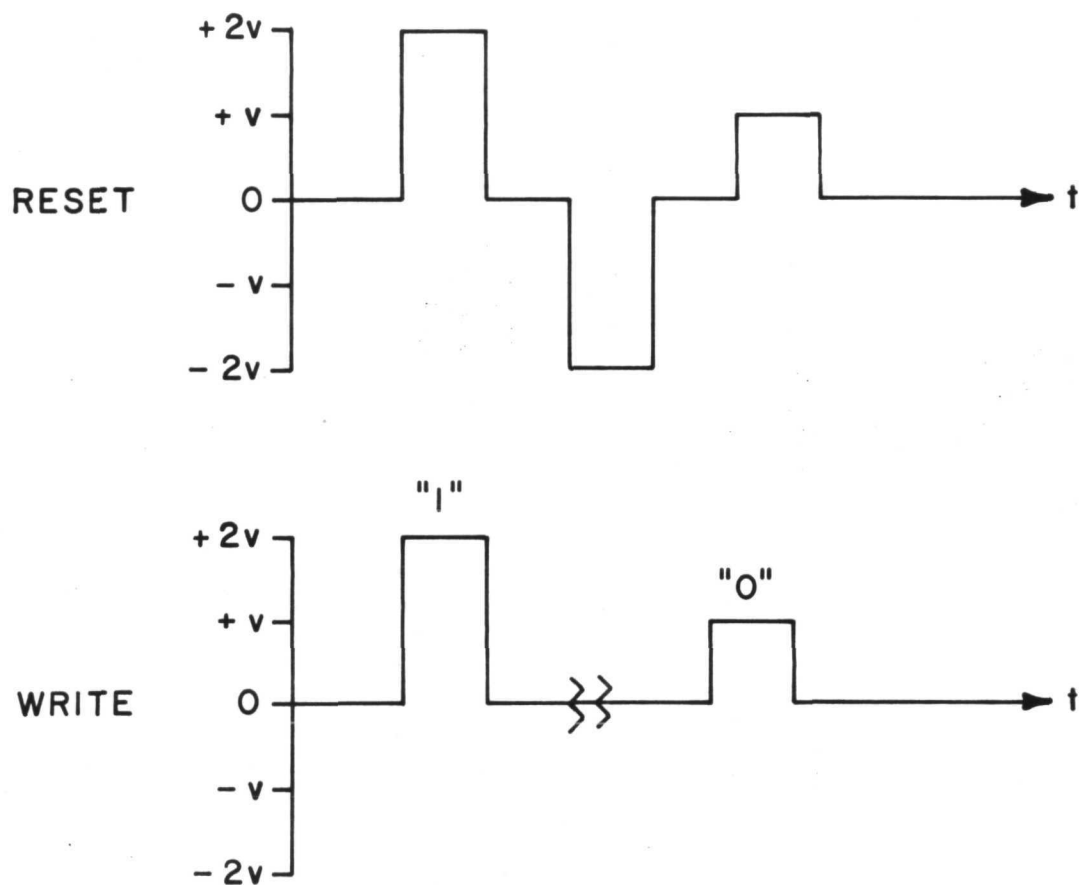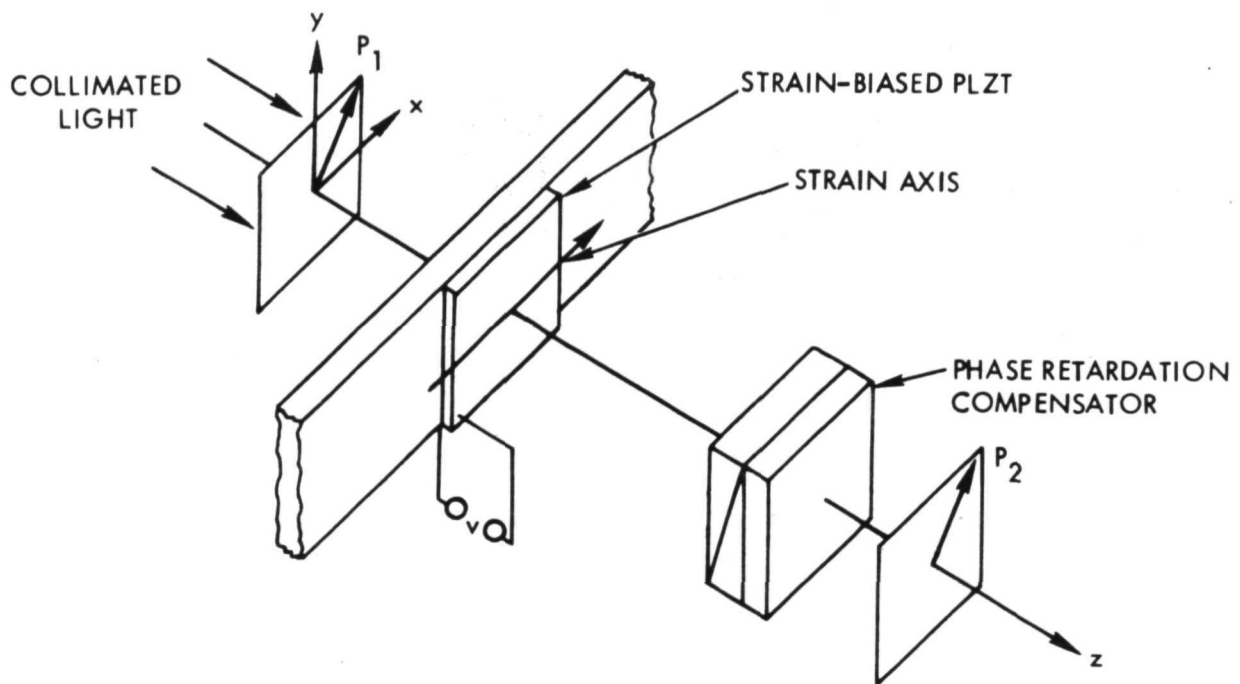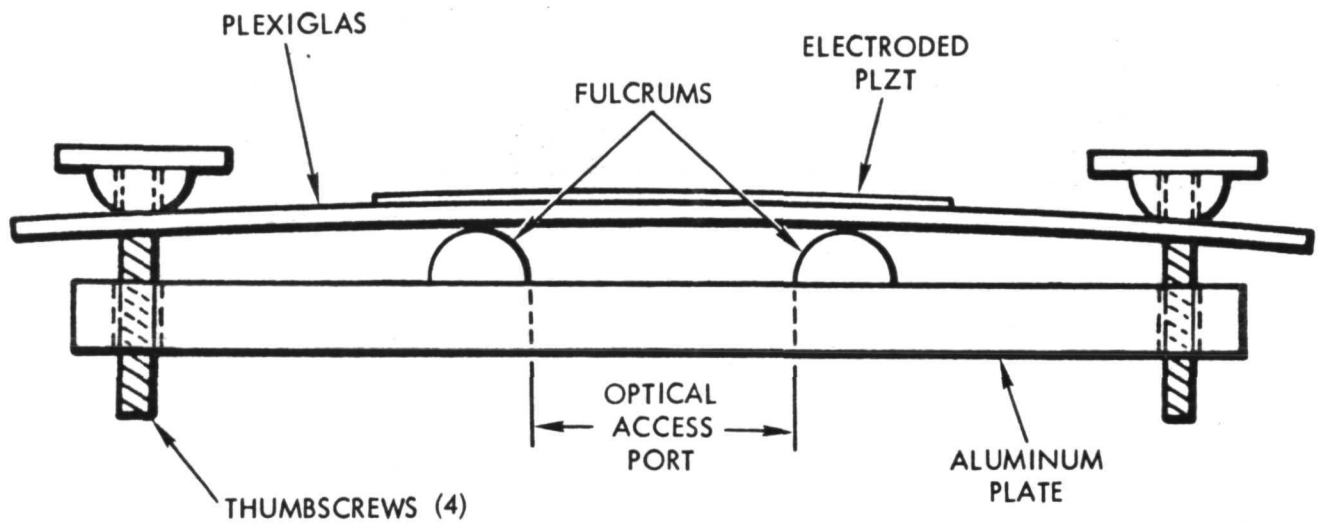"0" State (Depoled).

RADIATION
A DIVISION OF HARRIS INTERTYPE CORPORATION

Figure 3-7. Switching Pulses for Matrix BDC's

Figure 3-8. Optical Setup for Strain-Bias Operation

RADIATION
A DIVISION OF HARRIS INTERTYPE CORPORATION

PLEXIGLAS

FULCRUMS

ELECTRODED
PLZT

OPTICAL
ACCESS
PORT

THUMBSCREWS (4)

ALUMINUM
PLATE

85917-2A

Figure 3-9. Strain-Biasing PLZT by Bending Plexiglas in a Special Jig

The variation of the contrast ratio of a matrix element with switching voltage and with strain-bias is shown in Figures 3-10 and 3-11. The graph of contrast ratio versus $|\vec{S}|$ particularly illustrates both an advantage and a disadvantage of this mode – the high maximum contrast ratio and the rapid variation. This rapid variation means that nonuniformities in strain-bias over the matrix area will cause some sections of the array in the "1" state to be transmitting while other areas of "1's" are opaque. It has not been possible to operate a BDC at the maximum contrast ratio over the entire array because of the method of strain-biasing and also because of thickness variations and inhomogeneities in the PLZT. By reducing the strain-bias level, the matrix operation may be made more uniform. This is shown in Figure 3-12 for a 32 x 32 element BDC with ITO electrodes, and with the area between the elements masked off.

In Figure 3-13, is an enlargement of a 9 x 9 section from this 32 x 32 element array. The contrast ratio of the brightest elements has been measured at greater than 20 to 1. However, the nonuniform response of the PLZT to strain bias over the array remains the major problem in operating BDC's in this mode.

Scattering Mode. – The second basic mode of operation of PLZT BDC's is the scattering mode.[12] PLZT for this mode had G > 4.0 μm. Light passing through a matrix element is scattered into a solid angle which depends on the state of electric polarization of the element. An analysis of the scattering mode operation is given in Appendix A.

The optical elements for scattering mode operation are shown in Figure 3-14. Matrix elements which are poled into a "1" state will scatter the light into a much smaller solid angle than elements which have been depoled to the "0" state. The light from the matrix array of elements is focused on a pinhole which spatially filters the scattered light from the depoled elements but passes the majority of the light from the elements in the "1" state. In the image plane, the poled elements appear bright and the depoled elements appear dark. This mode of operation has the advantages that polarizers and strain-bias are not required and thickness variations are not critical.
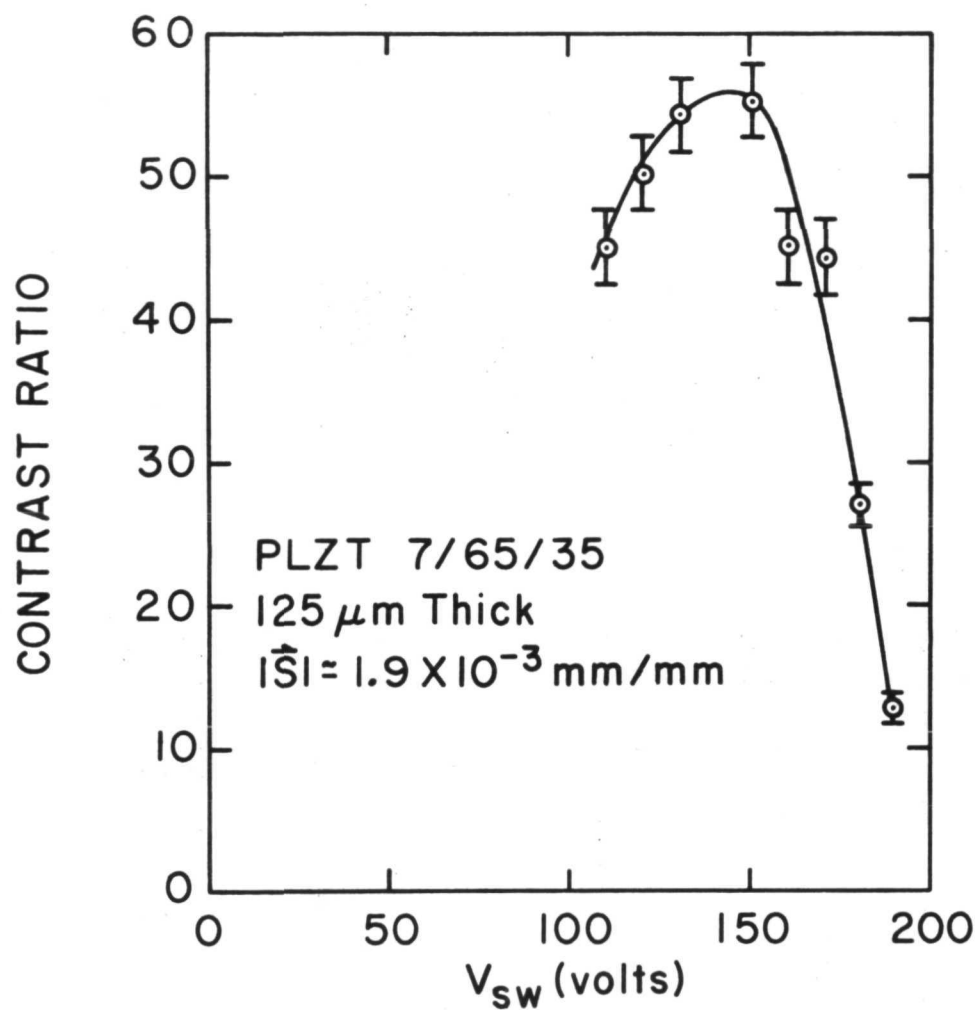
Figure 3-10. Contrast Ratio as a Function of Switching Voltage at Constant Strain
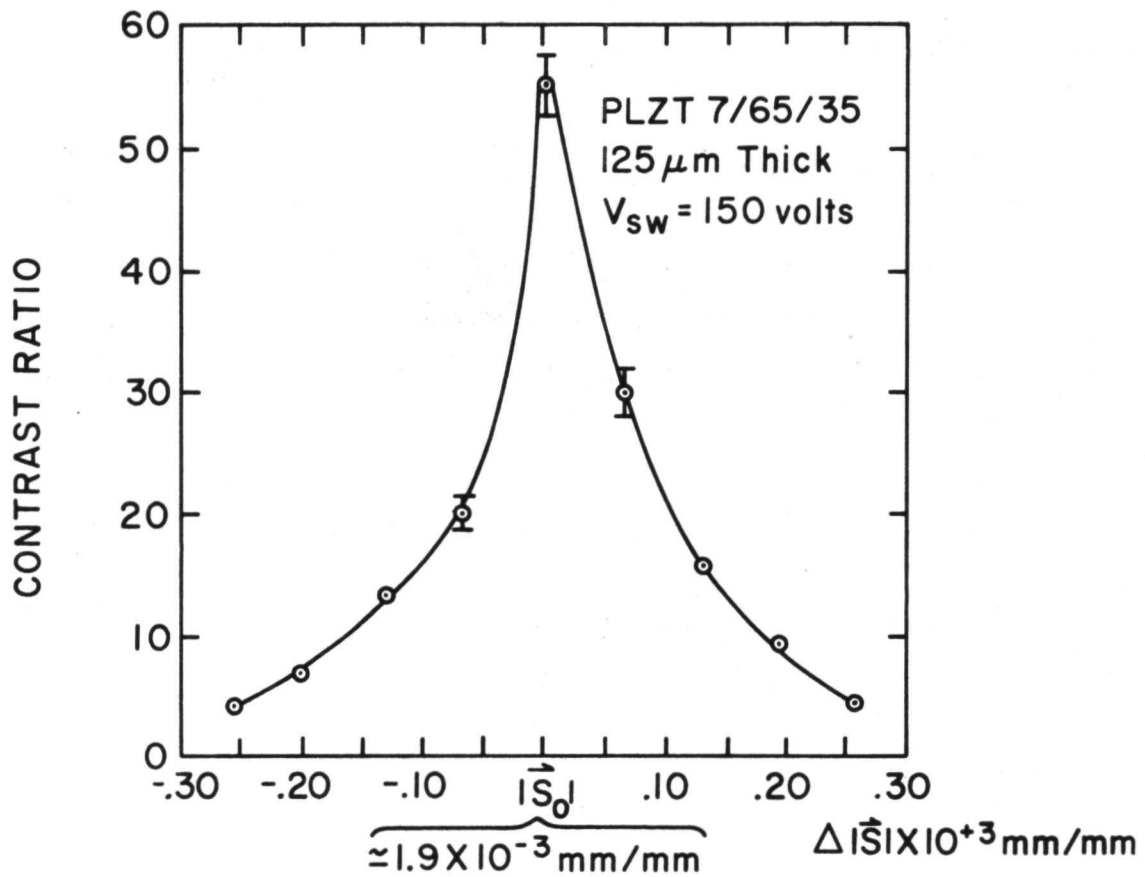
Figure 3-11. Contrast Ratio as a Function of Strain Bias at Constant
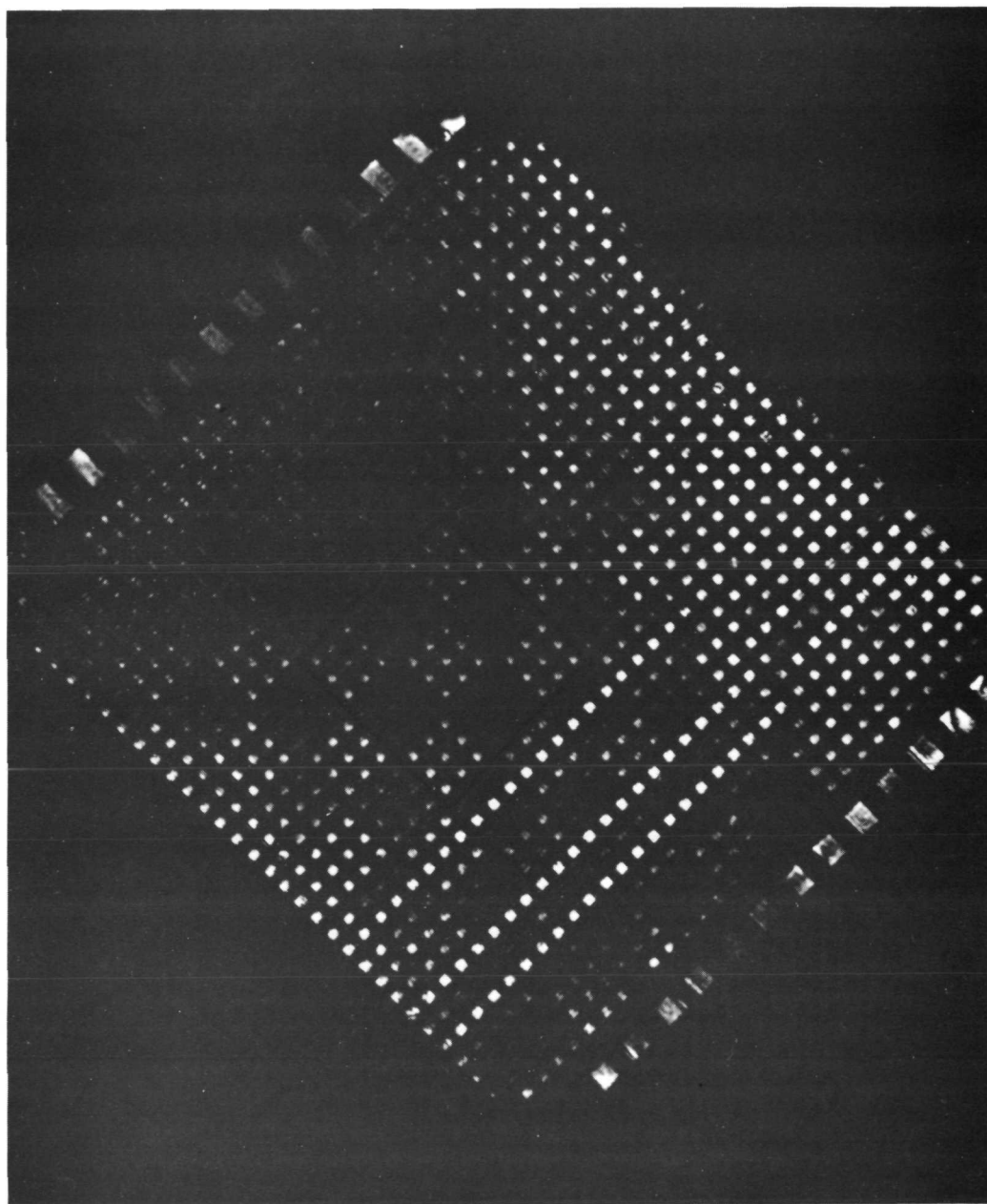Switching Voltage

Figure 3-12.   32 x 32 Element BDC with ITO Electrodes Operated in the Strain-
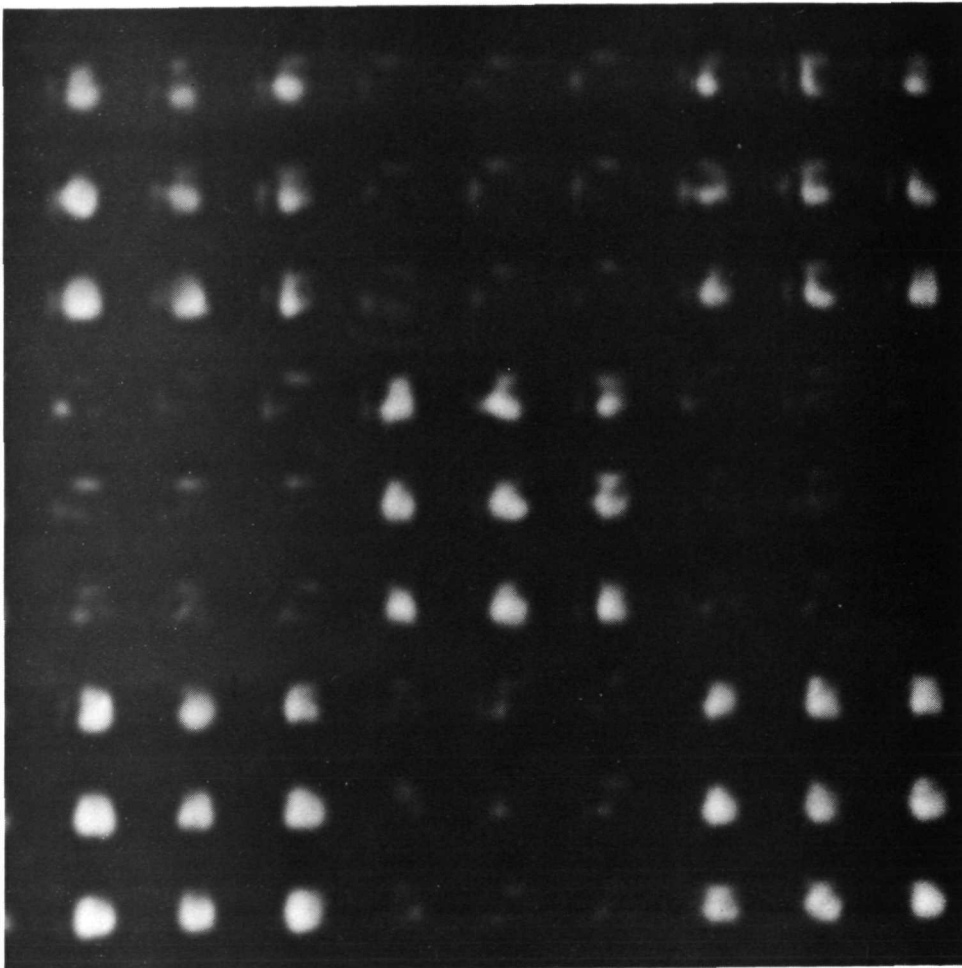Biased Mode with 3 x 3 Patterns of 1's and 0's
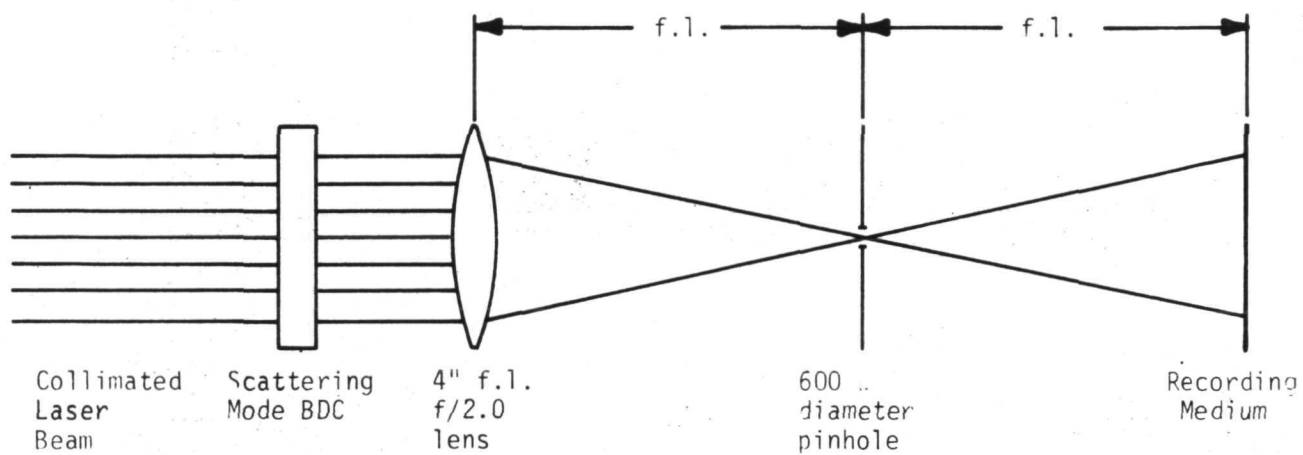
Figure 3-13.   Detail of Figure 3-12

RADIATION
A DIVISION OF HARRIS INTERTYPE CORPORATION

Collimated   Scattering   4" f.l.   600 ..   Recording
Laser   Mode BDC   f/2.0   diameter   Medium
Beam   lens   pinhole

Figure 3-14. Scattering Mode Optical Setup

The BDC's that we have tested in this mode have shown very uniform, but low, contrast ratios over the matrix array. Figure 3-15 shows the image of a 32 x 32 element device with a) all "0's" and b) checkerboard of "1's" and "0's" (two columns and one row did not work). For a 250 μm thick sample of PLZT and a switching voltage of 300 volts, using the optical setup in Figure 3-14, a contrast ratio of less than 5 to 1 was observed. Thicker PLZT (400 to 600 μm) and G > 6.0 μm should increase the obtainable contrast ratio but the optical insertion loss of the BDC will increase.

Edge-Effect Mode. - The edge-effect mode also depends upon a change in the birefringence of the PLZT but the change only occurs at the edges of the electrodes that define a matrix element. This type of BDC is placed between crossed polars as shown in Figure 3-16 and, thus, operates as an amplitude modulator with the same optical arrangement as the strain-bias BDC, but no strain-bias is necessary. The operation of the edge-effect BDC can be explained by referring to the diagram of a single element in Figure 3-17. The coordinate system is chosen with the unit vectors $\hat{x}_1$, $\hat{x}_2$ and $\hat{x}_3$ parallel, respectively, to the poling (optical) axis and the directions of the electrodes in the plane of the PLZT disc. When the matrix element is depoled then the average polarization is: $<\vec{P}> = 0 = <P_1> = <P_2> = <P_3>$. The principal strain components are: $S_{11} = S_{22} = S_{33} = 0$. This is also true for the volume of PLZT outside of the matrix element. When the element is poled then $<\vec{P}> = \hat{x}_1 <P_1> = \hat{x}_1 <P_r>$ and $<P_2> = <P_3> = 0$.

The strain components are then $S_{11} = S_{11}(P_r)$ and $S_{22} = S_{33} < 0$ (contraction). The volume of the PLZT outside of the matrix element is still in the depoled state, thus, a differential in strain of approximately $|S_{22}|$ occurs in the plane of the PLZT at the edges of the matrix element. This strain differential acts as a localized strain-bias, causing a high level of birefringence in the areas close to the element edges, and results in these areas acting as amplitude modulators. This effect can be seen in Figure 3-18 which shows a 32 x 32 element BDC operated in the edge-effect mode with a series of

RADIATION
A DIVISION OF HARRIS INTERTYPE CORPORATION
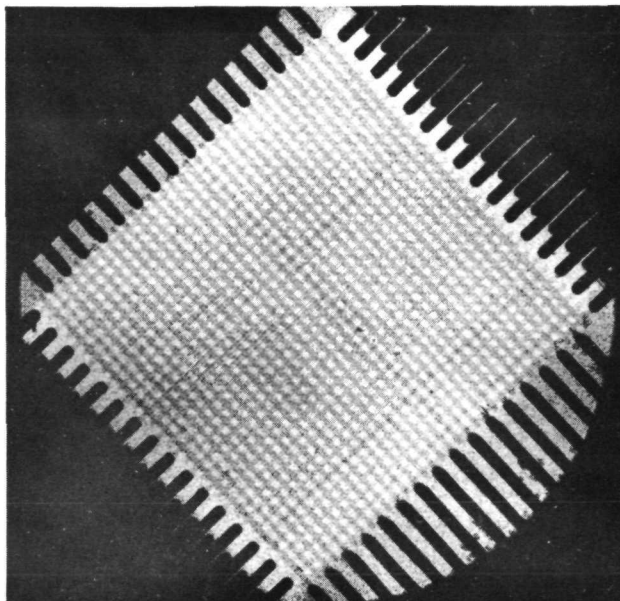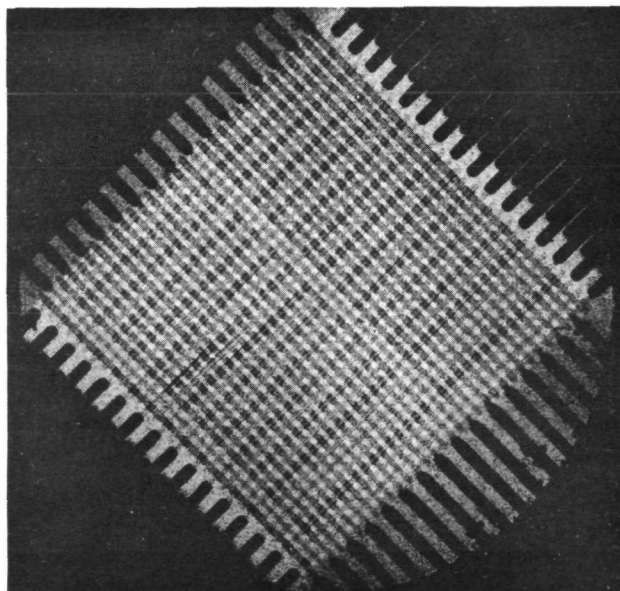
(a) ALL "0'S"

(b) CHECKERBOARD OF "1'S" AND "0'S"

Figure 3-15.   32 x 32 Element BDC Operated in Scattering Mode: a) All "0's" and
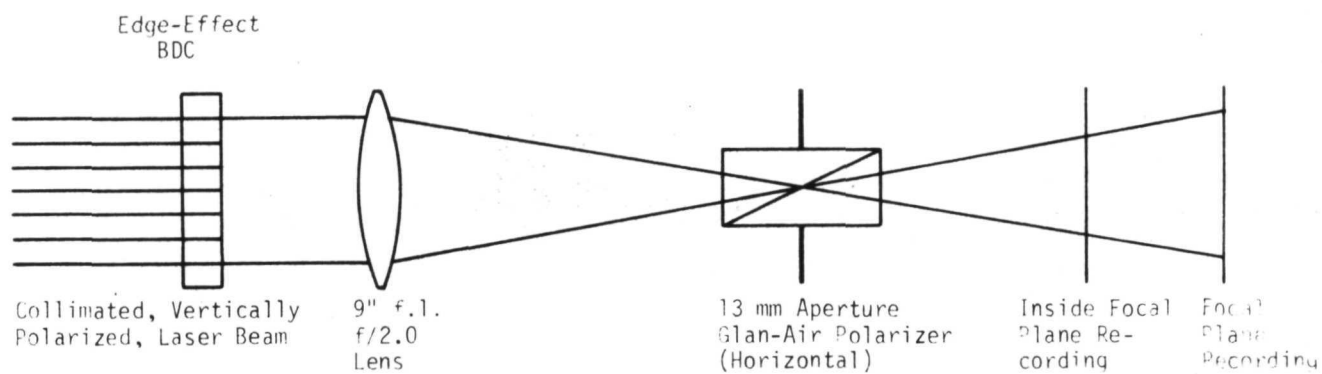b) Checkerboard of "1's" and "0's"

Edge-Effect
BDC

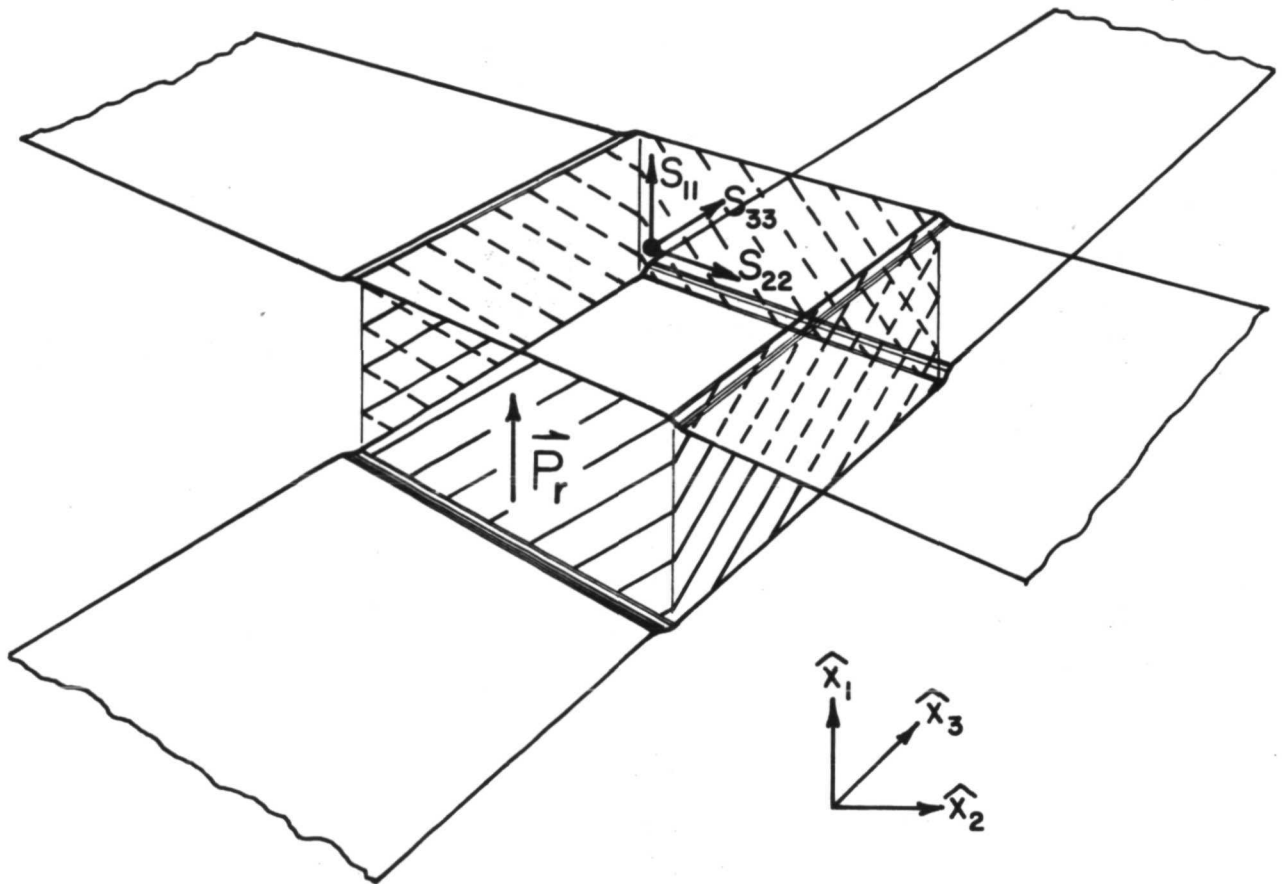Collimated, Vertically   9" f.l.   13 mm Aperture   Inside Focal   Focal
Polarized, Laser Beam   f/2.0   Glan-Air Polarizer   Plane Re-   Plane
                           Lens   (Horizontal)   cording   Recording

Figure 3-16. Edge-Effect Mode Optical Setup

RADIATION

A DIVISION OF HARRIS INTERTYPE CORPORATION

Figure 3-17.   Single Element of a Matrix-Type BDC
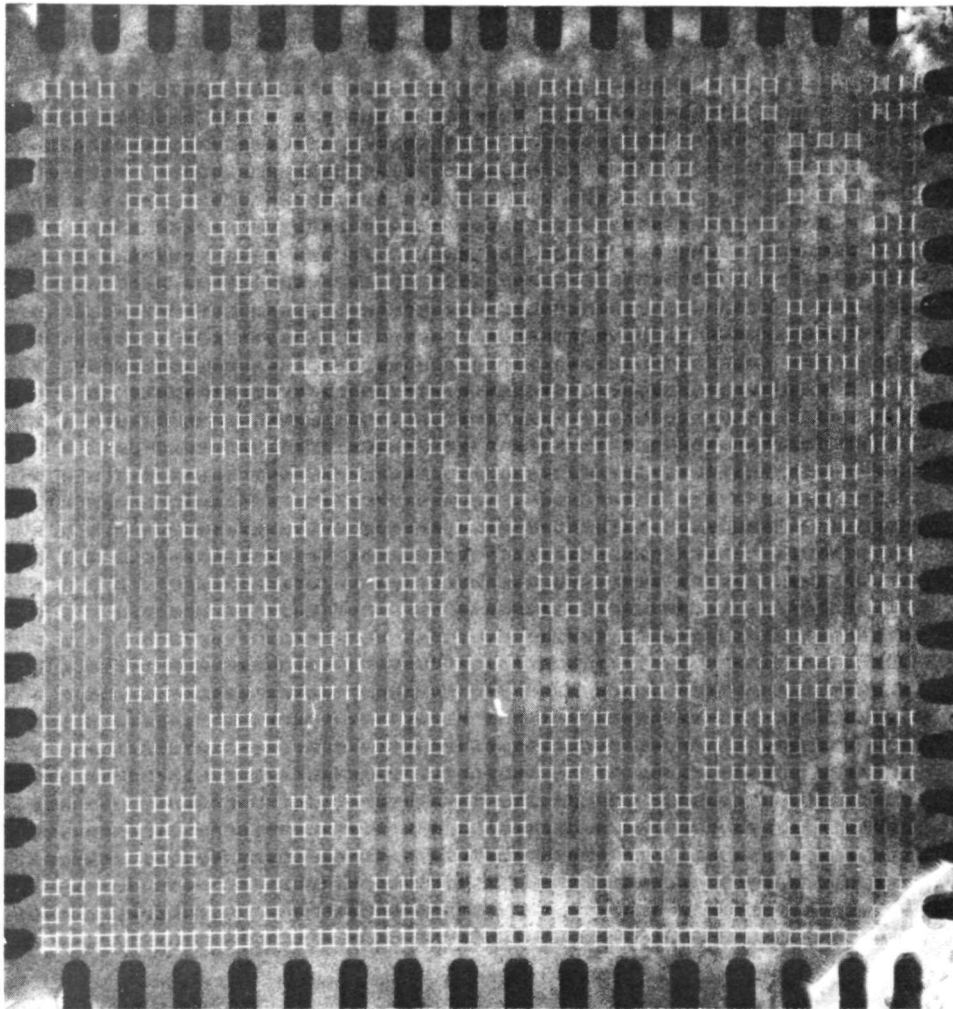
Figure 3-18. Edge-Effect Mode recorded at the Focal Plane

3 x 3 patterns of "1's" and "0's" written into the array. The bottom row, which has all "1's," shows the four birefringent areas outlining each element. If this BDC is then strain biased in the $\hat{x}_3$ direction, then the strain differential at the edges perpendicular to $\hat{x}_2$ will be decreased, reducing the birefringence while the differential at the edges perpendicular to $\hat{x}_3$ will be increased. Localized variations in the strain state of the PLZT will also affect the birefringence of the edge-effect areas. In operation, the pattern from the BDC would not be observed in the image plane of the lens, but slightly inside this plane giving a blurring effect as shown in Figure 3-19. We have also operated 128 x 128 element BDC's in the edge-effect mode and preliminary measurements have shown that the width of the edge-effect region depends only upon the thickness of the PLZT. This mode of operation would be useful for display purposes in the defocused case shown in Figure 3-19, or with segmented electrodes to increase the aperture fill factor. For BDC's with element sizes smaller than 100 μm x 100 μm and thicknesses greater than 200 μm, the width of edge-effect areas would extend into an appreciable amount of the aperture, yielding a useful contrast ratio. For the present devices, a contrast ratio of up to 10 to 1 has been observed, but the edge-effect mode also suffers from background level variations due to local strain variations.

Differential Phase Mode. - A new and very promising mode of BDC operation is the differential phase mode. In this mode, each element is used as a phase modulator rather than an amplitude modulator.

Phase modulation of the light passing through an element of the BDC results from a difference in the optical path length when the element is switched from a "0" state to a "1" state. In the "0" state, the optical path length through the element is $b_o n_a$ where b_o is the thickness of the PLZT and n_a is the index of refraction perpendicular to the optical axis. In the "1" state, the path length is:
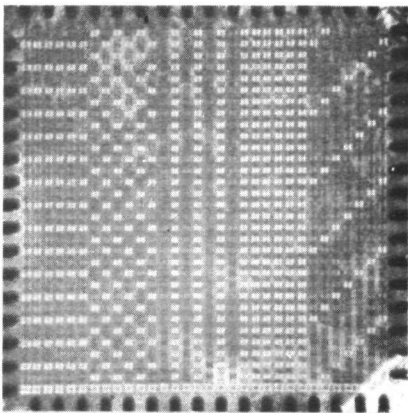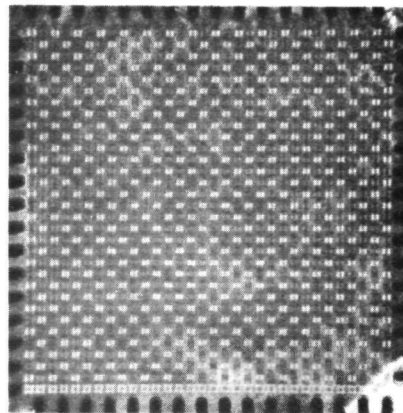
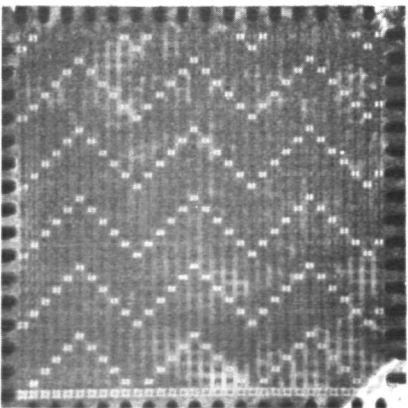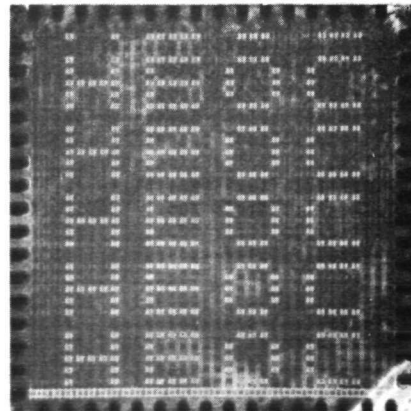$$b_r n_r = (b_o + \delta b)(n_a + \delta n) \tag{3-1}$$
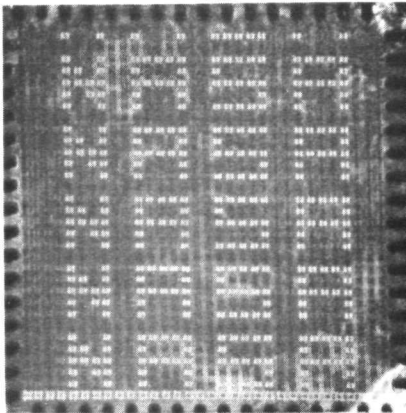
(a)
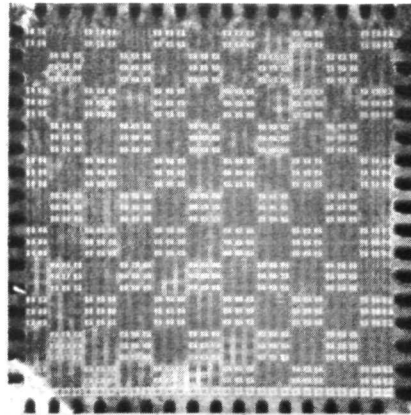
(b)

(c)

(d)

(e)

(f)

Figure 3-19. Edge-Effect Mode recorded inside the Focal Length

RADIATION

The change in thickness, δb, and the change in index of refraction, δn, are both functions of the strain components in the PLZT.

This can be explained by refering again to the diagram of a single element in Figure 3-17, and the strain components given for the "1" and "0" state given in the previous section.

Then:

$$b_r n_r = b_o n_a (1 + \delta b/b_o)(1 + \delta n/n_a)$$

$$\cong b_o n_a (1 + S_{11} + \delta n/n_a) \tag{3-2}$$

Where $\delta n/n_a$ is a function of S_{22} or S_{33} depending upon the light polarization, since S_{33} and S_{22} are the strain components perpendicular to $<\vec{P}> = \hat{x}_1 <P_r>$. The path length difference thus depends upon the electrostriction of the matrix element. The phase modulation is a function of the path length difference which is:

$$\Delta(bn_a) = b_r n_r - b_o n_a \cong b_o n_a (S_{11} + \delta n/n_a). \tag{3-3}$$

For 100 percent phase modulation $\Delta(bn_a) = \lambda/2$, at $\lambda = 633$ nm with $b_o = 125$ μm and $n_a = 2.5$, the sum of the electrostrictive and index of refraction change terms need only be $|S_{11} + \delta n/n_a| = 1.0 \times 10^{-3}$. It is not known at present which of these terms dominates but Uchida and Ikeda[13] have shown that $|S_{33}|$ for PLZT 53/47 is on the order of 1×10^{-3} mm/mm.

Further, we have observed that if strain-bias is applied to a BDC on a Plexiglas substrate with the axis of strain parallel to the polarization of the incident light, the phase modulation is reduced. This leads to the conclusion that $\delta n (S_{22}, S_{33})$ is the dominant term. It should be noted that since strain-bias in the $\hat{x}_3$ direction changes $|S_{22}|$ and $|S_{33}|$ and, thereby, $\delta n/n_a$, low level strain-bias can be used to adjust the path length difference to exactly $\lambda/2$ if $\Delta(bn_a)$ is slightly greater or less than $\lambda/2$.

Single Exposure Method. - In order to discuss the recording of data using the differential phase mode, we refer to a simplified version of the memory system as shown in Figure 3-20. The desired data pattern of "1's" and "0's" is switched into the BDC row by row. A hologram of the data is the recorded at or near the fourier transform plane on the photoplastic array, and the hologram developed. The BDC is then switched to a data pattern of either all "0's" or all "1's." The intensity of the signal and reference beams is adjusted so that the beam from the reconstructed hologram and that from the BDC are of equal intensity at the readout plane (photodetector array). If the linearly polarized light from the BDC is written as:

$$\vec{E}_1 (x,y,t) = \frac{\hat{x}_3}{2} \left[a_1(x,y) e^{i\phi_1(x,y) - i\omega t} + a_1^*(x,y) e^{-i\phi_1(x,y) + i\omega t} \right] \quad (3\text{-}4)$$

and the light from the BDC as:

$$\vec{E}_2 (x,y,t) = \frac{\hat{x}_3}{2} \left[a_2(x,y) e^{i\phi_2(x,y) - i\omega t} + a_2^*(x,y) e^{-i\phi_2(x,y) + i\omega t} \right] \quad (3\text{-}5)$$

where $a_1(x,y) = $ constant $\cdot a_2(x,y)$, then the total intensity of the two light beams interfering at the readout plane is:[11]

$$I_T = \frac{1}{2} \left[a_1^2(x,y) + a_2^2(x,y) \right] + \left[a_1^2(x,y) \, a_2^2(x,y) \right] \frac{1}{2} \cos \left[\phi_1(x,y) - \phi_2(x,y) \right] \quad (3\text{-}6)$$
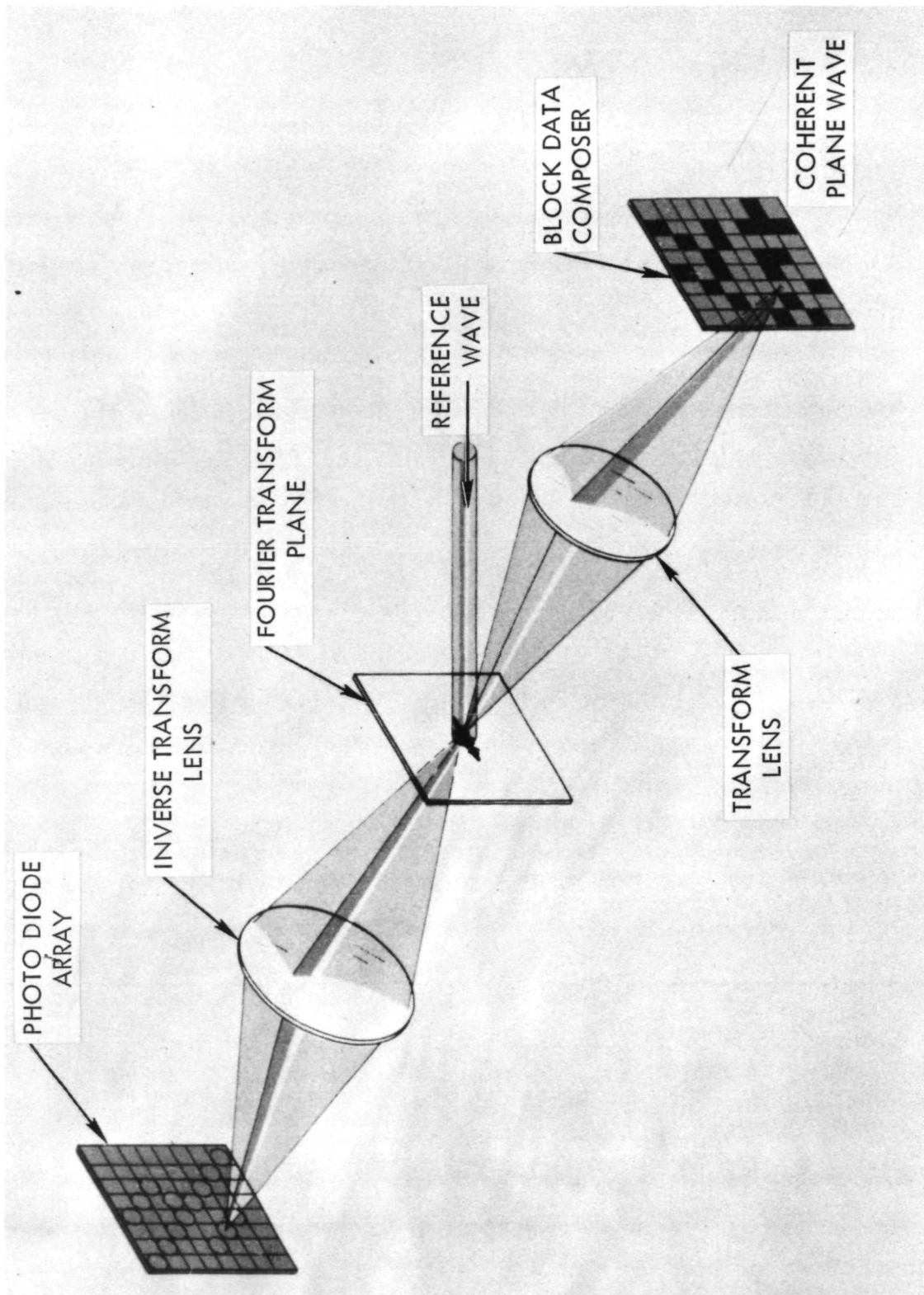
If the intensities of the two beams are equal, then:

Figure 3-20. Simplified Model of Holographic Memory System

$$I_T = 2a_1^2 (x,y) \cos^2 \left[\frac{\phi_1 (x,y) - \phi_2 (x,y)}{2} \right]$$

$$= 2a_1^2 (x,y) \cos^2 \left[\frac{2\pi}{\lambda} \Delta(bn_a) \right] = I_{max} \cos^2 \left[\frac{2\pi}{\lambda} \Delta (bn_a) \right] \qquad (7)$$

For maximum contrast ratio, $\Delta(bn_a) = \lambda/2$.

The background phase variations caused by thickness and strain nonuniformities will tend to cancel out; that is, if $\phi_1 = f_1 (x,y) + \frac{\lambda}{2}$ and $\phi_2 = f_1 (x,y)$ where $f_1 (x,y)$ is a random phase function, then $\phi_1 - \phi_2 = \lambda/2$. However, variations in the amplitude function $a_1 (x,y)$ caused by transmissivity variations in the PLZT will not be canceled out.

The data stored on the hologram can then be read out by writing all "1's" on the BDC. The elements written as "1's" on the hologram will interfere constructively with the light from the BDC and $I_{1-1} = I$ max. The elements written as "0's" on the hologram will destructively interfere with light from the BDC and $I_{0-1} = 0$. The complement of the data stored on the hologram can be read out by writing all "0's" on the BDC, that is: $I_{1-0} = 0$ and $I_{0-0} = I$ max.

This type of in situ readout could also be used to compare data stored in a hologram with other blocks of data. The difficulty associated with in situ readout is that the optical path lengths must not vary more than a small fraction of a wavelength of light during the entire time of recording and readout.

Double-Exposure Method. - The problem of keeping the optical path lengths stable for long periods of time can be avoided by the double exposure recording method. The desired data pattern is written on the BDC and the photoplastic exposured once, but not developed. The data pattern on the BDC is then changed to all "1's" and a second hologram recorded on top of the first. The photoplastic is then developed and both holograms are

read out with the reference beam only. In the readout process, light diffracted from the two holograms will interfere, and the "1's" and "0's" in the data pattern recorded on the first hologram will appear as bright and dark spots, respectively, at the readout plane. The optical path lengths need only remain stable over the time necessary to record the two holograms, while the data can be stored for an indefinite length of time before readout.

The BDC's used in our experiments were 32 x 32 element arrays on both Pyrex and Plexiglas substrates with Cr-Au and with ITO electrodes. The single-exposure method gave contrast ratios of greater than 15 to 1 while the double-exposure method gave contrast ratios of between 10 and 15 to 1.

An example of a reconstructed double-exposure hologram is shown in Figure 3-21. The pattern is of alternate rows of "1's" and "0's" written top to bottom. Columns 5, 6, 7, 8 and 11 from the right side of the pattern were only partially working due to a crack in the PLZT. The parts of the columns which were never switched scattered less light than the rest of the columns. The light from these unswitched elements appears much brighter in the reconstructed data. It was found that the sum of the exposures must be kept on the linear portion of the curve of diffraction efficiency versus exposure of the photoplastic for complete destructive interference to occur in the double-exposure method (see Figure 4-7).

The limit on the contrast ratio obtained for both methods was scattered light from the photoplastic recording material. Contrast ratios of greater than 35 to 1 should be achievable with low noise photoplastics.

The advantages of the differential-phase mode are: 1) no strain-bias is required, 2) no polarizers are required, and 3) thickness and strain variations (background non-uniformities) are cancelled out. The disadvantages are 1) the contrast ratio is lower than the maximum obtainable with strain-biased operation and 2) a double hologram must be recorded.
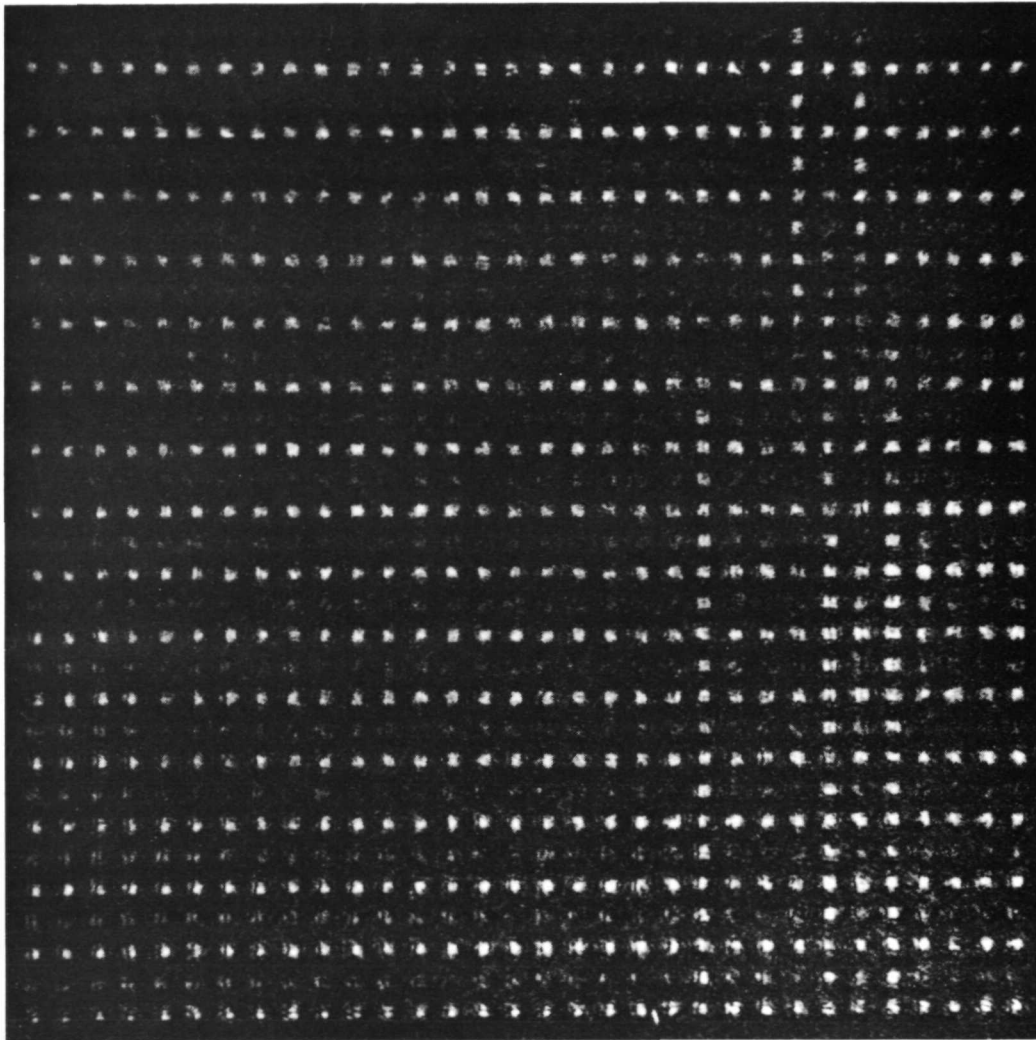
Figure 3-21. Reconstruction of a Double Exposure Hologram of Alternate Rows
of 1's and 0's Made with a 32 x 32 Element PLZT BDC Operated in the
Differential Phase Mode

RADIATION

A DIVISION OF HARRIS INTERTYPE CORPORATION

Summary. - The strain-biased mode has shown the highest contrast ratio for individual matrix-elements, but was the most nonuniform over the entire matrix array. The differential phase mode cancels out the background phase nonuniformities but the contrast ratio is lower than the strain-bias mode. The edge-effect mode also suffers from background nonuniformities and has a still lower contrast ratio due to the low-aperture fill factor. The scattering mode devices are the most uniform in contrast ratio and background level of any of the devices tested, but the contrast ratio is lower and the insertion loss higher than any of the other three modes.

3.4   BDC Testing

Electronics for testing 32 x 32 BDC's in a mode which simulates computer control of both the read-in and erase functions was designed, assembled, and successfully tested during the first quarter of the contract. The circuitry consists of 64 identical 300-volt transistor switches on eight plug-in pc boards, logic to define and control switching sequences, internal power supplies, four 16-conductor flat cables with 16-pin DIP connectors, and rack mountable cabinetry. Up to 32 x 32 positions can be accessed with this equipment. It can be programmed to perform a wide range of tests with the 32 x 32 BDC's. The important parameters are reviewed below:

1. ON/OFF/ERASE voltages can be set from the front panel to any level in the 25-300 volt range.

2. Six manual switches establish a six-bit sequence which is repeated to fill the column register. A complement switch is included to complement the data in successive rows.

3. A write sequence can be automatically or manually completed.

4. Successive rows can be switched at rates in the 10^0-10^5 rows/second range

5.   Pulse widths for row-writing can be as short as 20 μs and as long as needed (by changing a timing capacitor).

6.   A three-pulse ERASE cycle with pulse widths and pulse spacings down to 100 μs has been established. A manual switch for repeating ERASE cycles is included.

The Reset and Write pulses are shown in Figure 3-7.

All sequence start and manual control functions are activated from a remote-control unit which can be located up to six feet from the switching circuitry. This circuitry is shown in Figure 3-22.

During the last half of the contract, the BDC's were tested in a simplified version of the holographic memory system which included a one-element photoplastic recording device and a scanning photomultiplier for contrast ratio measurements. The measurements for the strain-bias mode, scattering mode and differential phase mode were made on this optical test bench.

3.5   Conclusions and Recommendations

The most significant problem of the past contract period was the variation in the electro optic response of the PLZT. We were further hampered by the lack of data on the electrical and physical properties of each group of material we received. It is recommended that a program of material testing be initiated to identify those properties of PLZT which most affect the operation of the BDC; the data from these tests to be correlated with the data from the electro-optic testing of BDC's fabricated from the same material. In this manner, the PLZT properties may be specified more closely to the supplier, and better and more consistent operation of PLZT BDC's should result.

A most important development of this contract was the discovery of two new modes of operation of the BDC; the edge-effect and differential phase modes. The differential

RADIATION
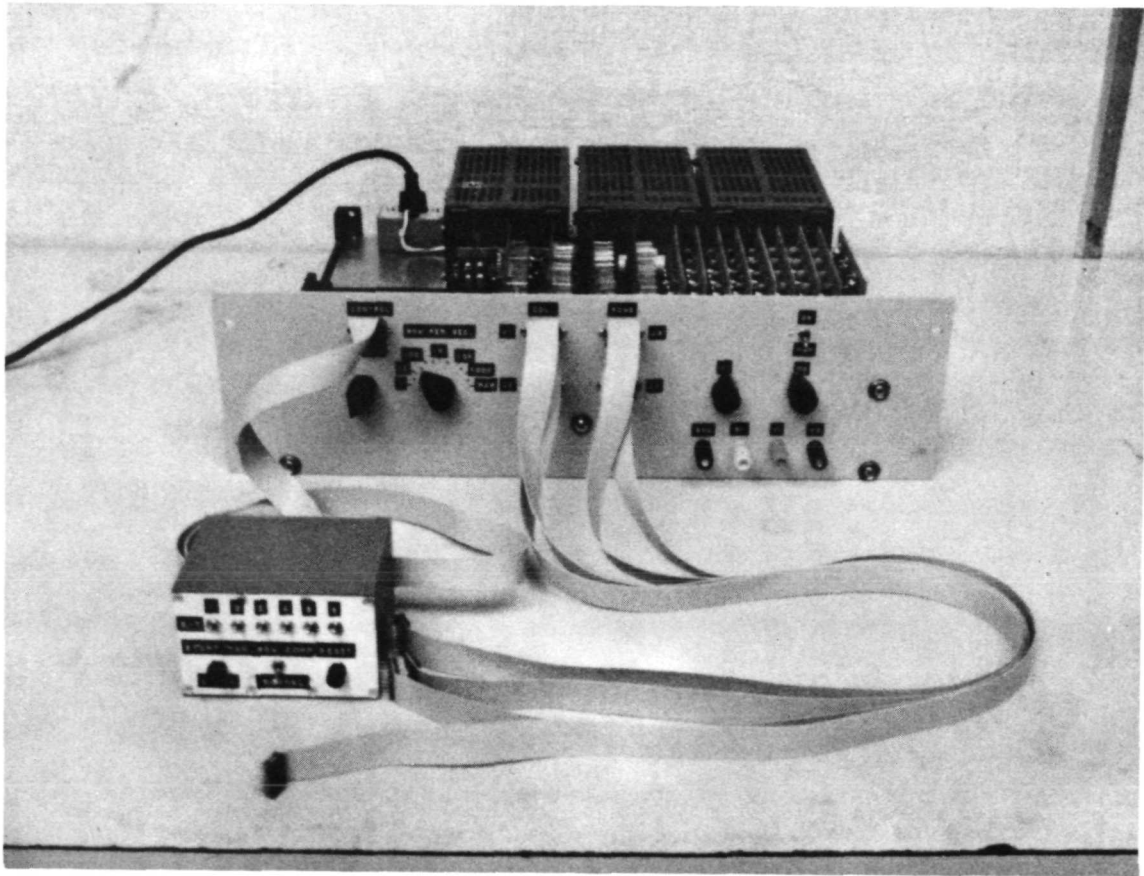
A DIVISION OF HARRIS INTERTYPE CORPORATION

Figure 3-22. Special Test Electronics for 32 x32 BDC's

phase mode particularly offers the promise of more uniform and reliable performance. The differential phase and the strain-bias modes of operation should continue to be investigated as the two most likely modes of BDC operation in the memory system.

The fabrication of 32 x 32 element BDC's with 0.5 mm x 0.5 mm elements on 1.0 mm centers has progressed to the point that only minor technical problems remain. The 128 x 128 element BDC's with 150 μm x 150 μm elements on 250 μm centers will require other techniques of electrode interconnection. To this end, we should fabricate 32 x 32 element devices on 250 μm centers, and perfect the interconnection techniques on these devices before returning to 128 x 128 element array fabrication.

RADIATION
A DIVISION OF HARRIS INTERTYPE CORPORATION

SECTION IV
PHOTOPLASTIC RECORDING MATERIALS
4.1 Introduction

Significant improvements were made during the contract period in the photoplastic recording materials and techniques. Corona charging has been replaced by a technique using a plane electrode parallel to the thermoplastic surface. With this device, charging is rapid and uniform, and is achieved with one-tenth the corona voltages. Improvements in materials have extended the lifetime of the thermoplastics to over one-thousand·record-erase cycles; the diffraction efficiency and signal-to-noise ratio remain high throughout. The latent image problem has been alleviated by modification of the erasure procedure.

The 5 x 5 hologram array has been expanded to 20 x 20, with 1 mm holograms on 1.5 mm centers. The array is organized into 20 strips each containing 20 hologram locations. Adoption of parallel plane charging led to a slightly more compact fixture to hold the hologram array; in addition, the photoplastic recording material is completely enclosed.

4.2 Operational Techniques

The 5 x 5 hologram array and fixture suffered from nonuniform charging. We conducted several experiments to investigate more fully the nature of the charge distribution obtained from a fixed corona device. To determine the uniformity of charge distribution over an area comparable to the overall photoplastic array, we fabricated a special aluminum test plate with built-in shielded probes and a simple corona discharge device. The probes, spaced at 6 mm intervals along the center of the plate, could alternately be connected to a picoammeter to measure the corona current. The corona device was the usual thin wire surrounded by shield with a slit along one side.

We conducted experiments to measure the effect of corona potential and location on the corona current to the plate. Most of our measurements were performed with an uncoated test plate; some tests were conducted on a plate coated with an insulating layer, but these were subsequently discarded because of excessive attenuation of the corona currents.

In the first experiment, the charging device was placed 50 mm in front and parallel to the top edge of the plate. With the shield at zero volts, the input to the corona device was varied from 5000 to 6660 volts, and induced current was sampled perpendicular to the charging wire. Figure 4-1 shows the results obtained for five levels of input voltage.

In the second experiment, the input to the corona device was maintained at 6250 volts and the shield at zero volts. The charging device was aligned with the top edge of the plate but at a distance varying from 1.2 cm to 7.5 cm. Figure 4-2 shows the results for five different distances. Although the charge distribution is more uniform at greater distances, the charge density is too low for optimum hologram recording. The decrease in corona current caused by moving the corona device away from the plate can be partially offset, however, by enlarging the opening slit in the corona shield.

In another experiment, we raised the potential of the shield with respect to the test plate. The corona voltage was maintained at 5000 volts and the shield at 0, 300, and 600 volts; the corona device was set at approximately 2 cm in front and 1 cm above the top of the plate. Figure 4-3 shows that the charge distribution is not significantly affected by variation of the shield potential. Rotating the corona device so that the slit in the shield points toward the bottom of the plate generally reduced the level of the corona current but did not affect the distribution over the plate.

We concluded from these tests that, only by locating the corona device several centimeters from the array, could we expect adequate charge uniformity. Obtaining sufficient charge density remained a problem, however. In an alternative approach, we
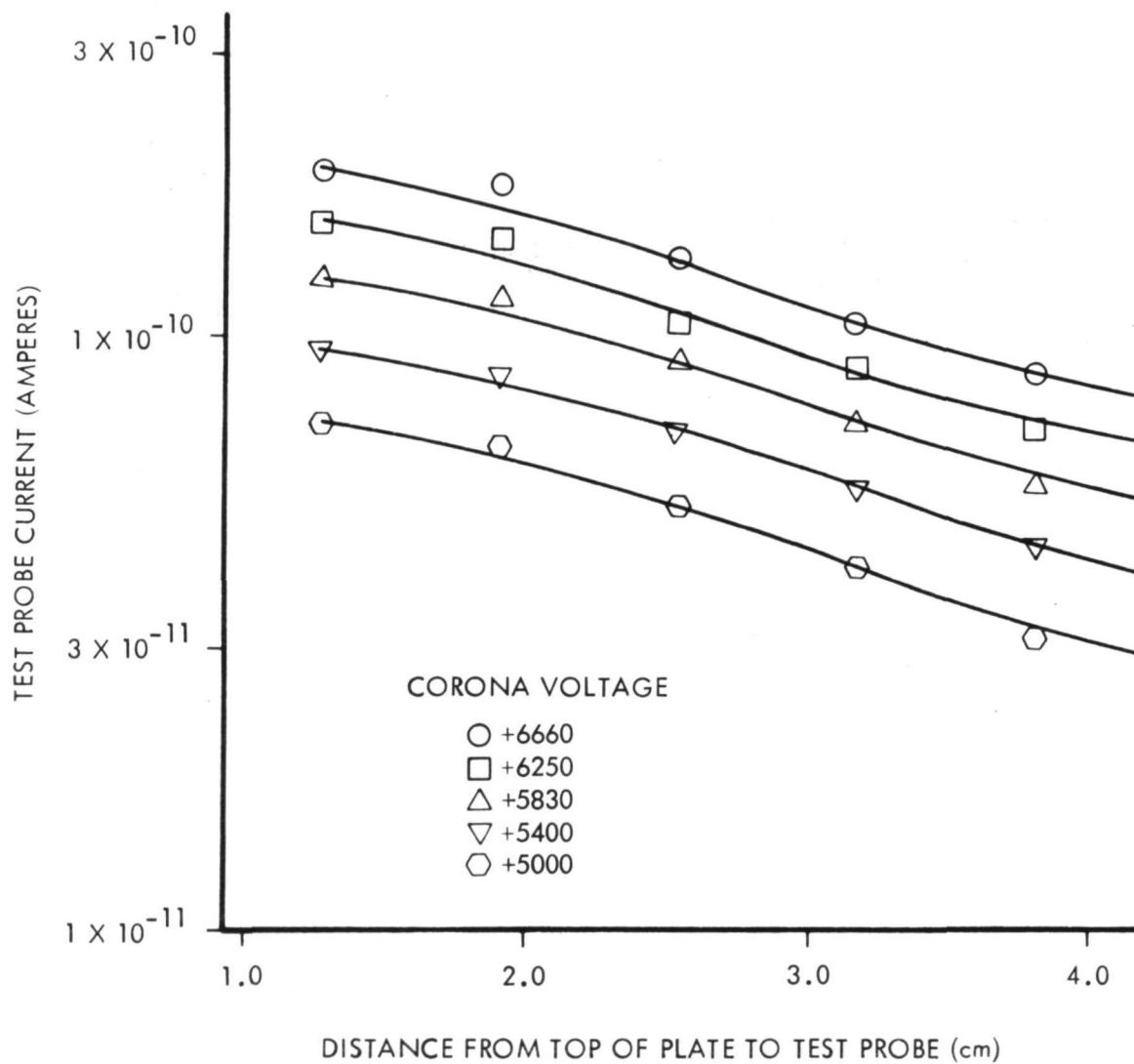
Figure 4-1. Sampled Charging Current as a Function of Distance
from Test Plate Top for Various Corona Voltages

RADIATION
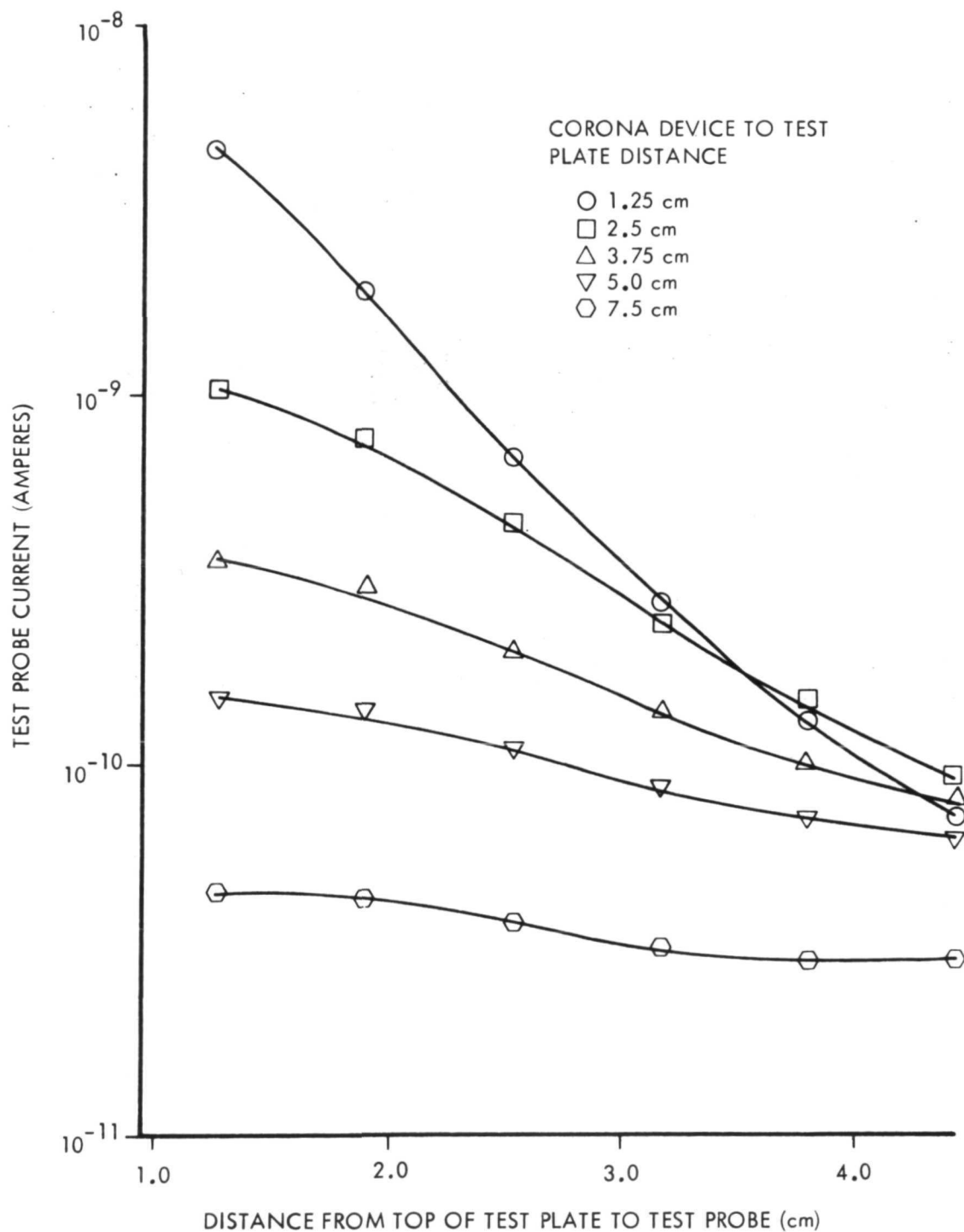A DIVISION OF HARRIS - INTERTYPE CORPORATION

Figure 4-2. Sampled Charging Current as a Function of Position on the
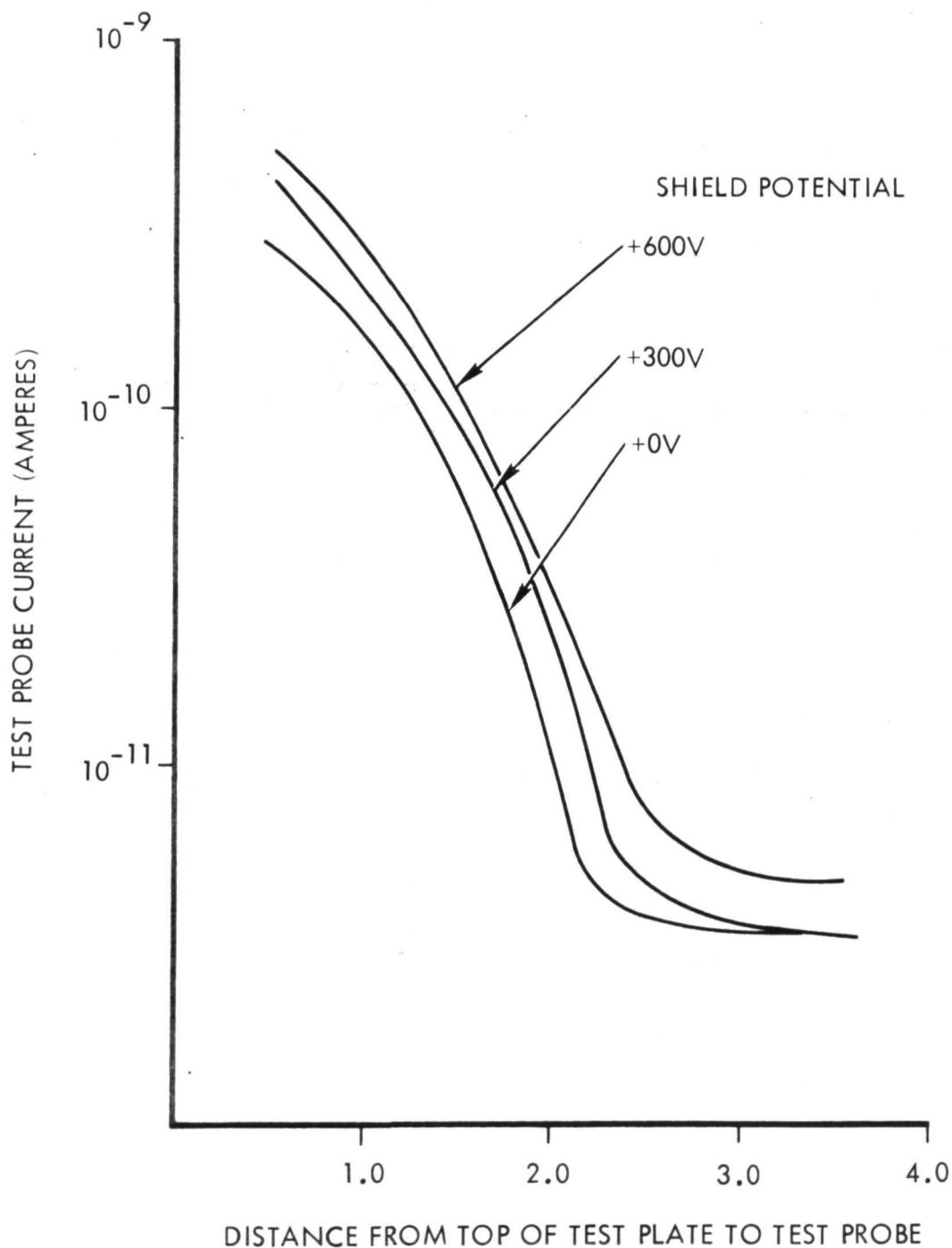Test Plate for Various Distances Between Corona Device and
Test Plate.

Figure 4-3. Charging Current as a Function of Position on the
Test Plate for Various Shield Potentials

conducted experiments to demonstrate whether a grid placed in near contact with the photoplastic device could improve the charge uniformity over relatively large surfaces. We anticipated that if the grid was maintained at a constant potential of several hundred volts above the ground plane, the thermoplastic surface potential would be limited to the same value. This potential limitation would improve our control of the charging process, prevent thermoplastic breakdown due to overcharging, and improve the charge uniformity over large areas.

In these experiments, the grid was a flat copper sheet with 3 mm diameter holes spaced at 5 mm intervals and the corona charging device was the conventional thin wire surrounded by a shield. The results did not agree with our expectations in that the photoplastic surface potential was not uniform, and the thermoplastic layer degraded excessively after only a few record-erase cycles. These problems may have been due to excessively large holes in the screen and to excessive corona voltages that were needed to record holograms with moderate efficiencies. Nevertheless, this did not appear to be a promising solution to the problem of uniform charging.

A much more attractive solution is to charge the thermoplastic surface from an electrode parallel to and several μm above the thermoplastic. This technique has the potential of charging a large area rapidly and uniformly without moving parts, and with one-tenth the previous voltages. Figure 4-4 shows the configuration of the new device. The air gap is typically 50 μm. To charge the thermoplastic surface, a positive voltage is applied to the upper electrode, with the lower electrode grounded. This voltage is capacitively distributed across the photoplastic materials and the air gap (the photoconductor acts as a leaky capacitor, with a variable resistance dependent on the illumination intensity). When the voltage across the air gap exceeds the breakdown voltage of the air, current flows, conducting charge to the surface of the thermoplastic. The surface potential of the thermoplastic rises until the voltage differential across the air gap is reduced to below breakdown, and charging ceases. The potential reached by
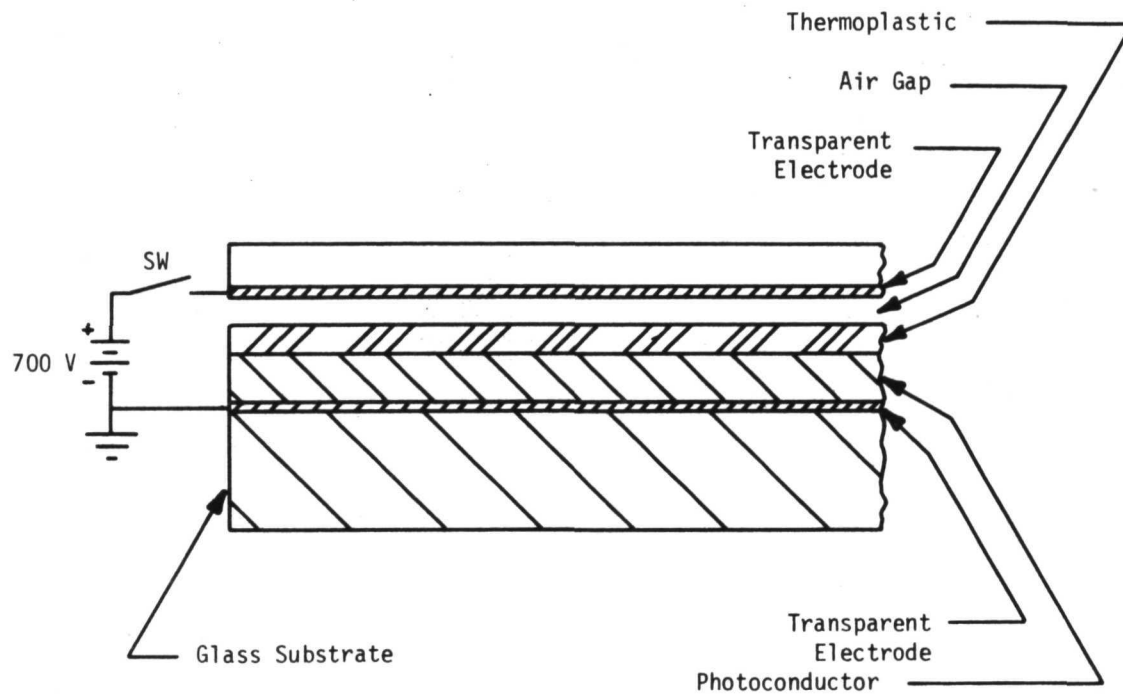
Figure 4-4. Configuration of New Charging Technique

the thermoplastic surface can be controlled by adjusting the amount by which the applied voltage exceeds the breakdown voltage.

Figure 4-5 shows a curve of thermoplastic surface potential as a function of applied voltage for a 50 μm air gap at atmospheric pressure. These data were obtained by increasing the applied voltage an incremental amount and measuring the surface potential with an electrometer; the thermoplastic was not erased between charging steps. The stepwise increase of the surface potential indicates that the breakdown voltage is greater than the voltage required to sustain breakdown, as expected in a gas discharge. Devices which were erased between cycles showed a linear relationship between surface potential and applied voltage since the surface potential was reduced to zero during erasure. The surface potential depends on the strength of the applied voltage and is essentially independent of the time it is applied.

The charge is extremely uniform across the surface of the array. The potential measured on the surface of a 30 millimeter square array following a 150 millisecond charging cycle is constant to within ±5%. Charging the surface for an additional 5 seconds did not change the potential values.

By monitoring the charging current with an oscilloscope, we were able to observe the duration and amplitude of the breakdown. We found that for a 0.3 cm^2 photoplastic device with approximately 60 μm spacing between the upper electrode and the thermoplastic surface, breakdown occurs from 100 to 800 ms after the voltage is applied. The duration of the breakdown itself is approximately 0.5 ms; during this time adequate charge is conducted to write a hologram.

The time lag from application of voltage to breakdown appears to be a result of the slow rise time (200 ms) of the applied voltage. We found that applying the charging voltage by discharging a capacitor with a time constant of approximately 1.5 ms, we could charge the thermoplastic surface in 4 ms.
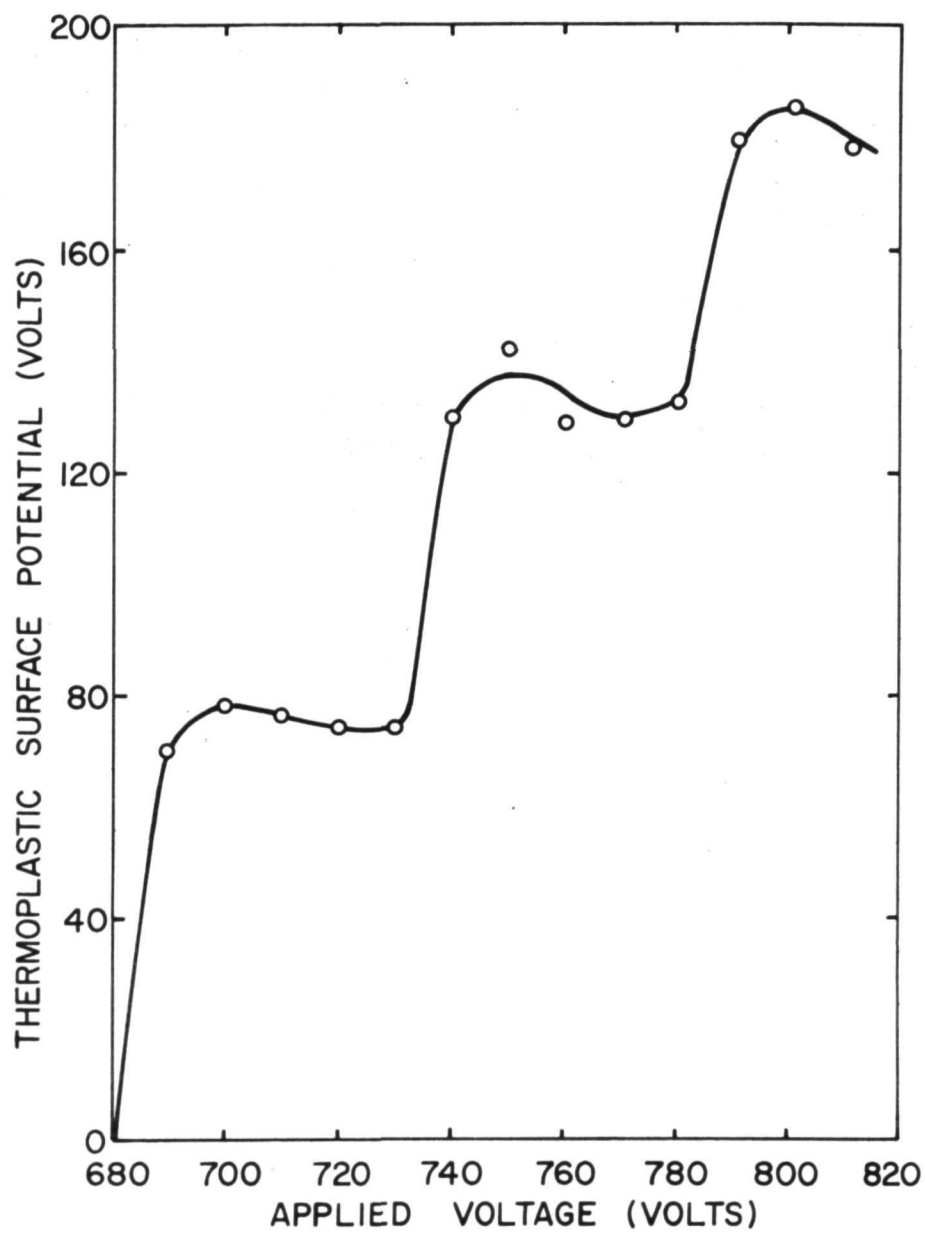
Figure 4-5. Plane to Plane Charging Characteristics

RADIATION
A DIVISION OF HARRIS INTERTYPE CORPORATION

4.3   Holographic Parameters

We measured certain holographic parameters of the photoplastic materials, including exposure sensitivity, diffraction efficiency, signal-to-noise ratio (SNR), and bandwidth. We also determined the sensitivity of diffraction efficiency and SNR to charging and to the development heat. These measurements were carried out with the standard polyvinylcarbazole/trinitrofluorenone (PVK/TNF) photoconductor. We used a highly stabilized ester resin as a standard thermoplastic for most of our photoplastic investigations because this material forms holograms of complex signals with efficiencies of several percent and can be cycled several hundred times with little degradation. Although other thermoplastic materials were capable of greater cycling, they formed less efficient holograms or were less readily available.

To determine exposure sensitivity and diffraction efficiency, we recorded a series of plane wave gratings at several reference-to-signal beam-, or K-ratios. Figure 4-6 shows curves of diffraction efficiency as a function of exposure for K-ratios of 1, 4, 10, and 40. The peak diffraction efficiency is 10 percent occurring at an exposure of about 60 microjoules/cm^2. At K = 1, the material has a very broad response, with a nearly constant efficiency over four orders of magnitude of exposure.

We measured diffraction efficiency and SNR as a function of exposure for holograms of a diffusely illuminated signal. This signal was a 2 cm x 2 cm square with a 1 cm x 1 cm opaque square in the center. The geometry was adjusted to give an information packing density of approximately 2.5 x 10^6 bits/cm^2. Holograms were recorded at a wavelength of 633 nm and a K-ratio of five. Typical results are shown in Figure 4-7; the SNR reaches a peak of 16.5 dB at an exposure of 20 microjoules/cm^2, with a diffraction efficiency of 1.6 percent. At the peak diffraction efficiency of 3.8 percent, the SNR has decreased to 11.5 dB. The 1.6 x 10^6 bits/cm^2 packing density for the holograms on the test breadboard system at NASA/MSFC will provide a SNR approximately 2 dB better than shown in Figure 4-7.
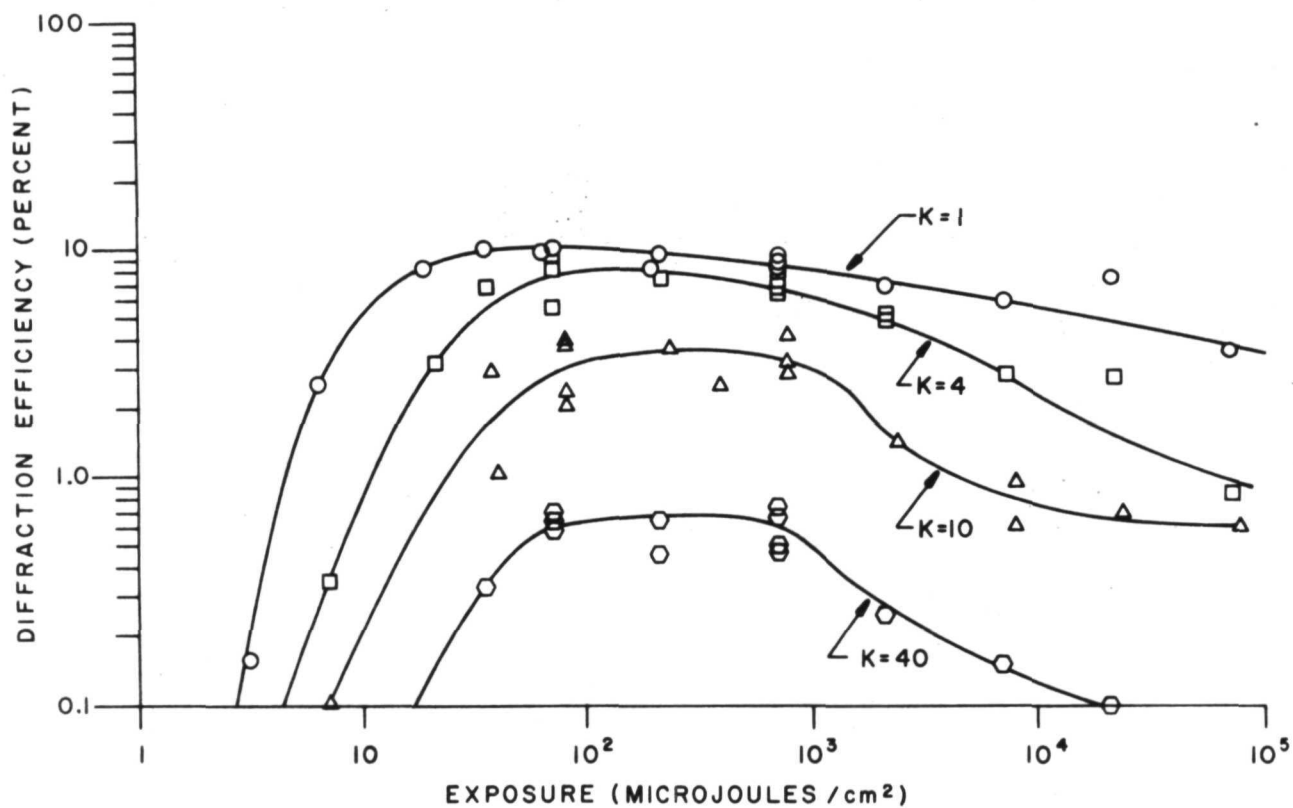
Figure 4-6. Diffraction Efficiency as a Function of Exposure for Plane Wave Gratings Recorded in Photoplastic

RADIATION
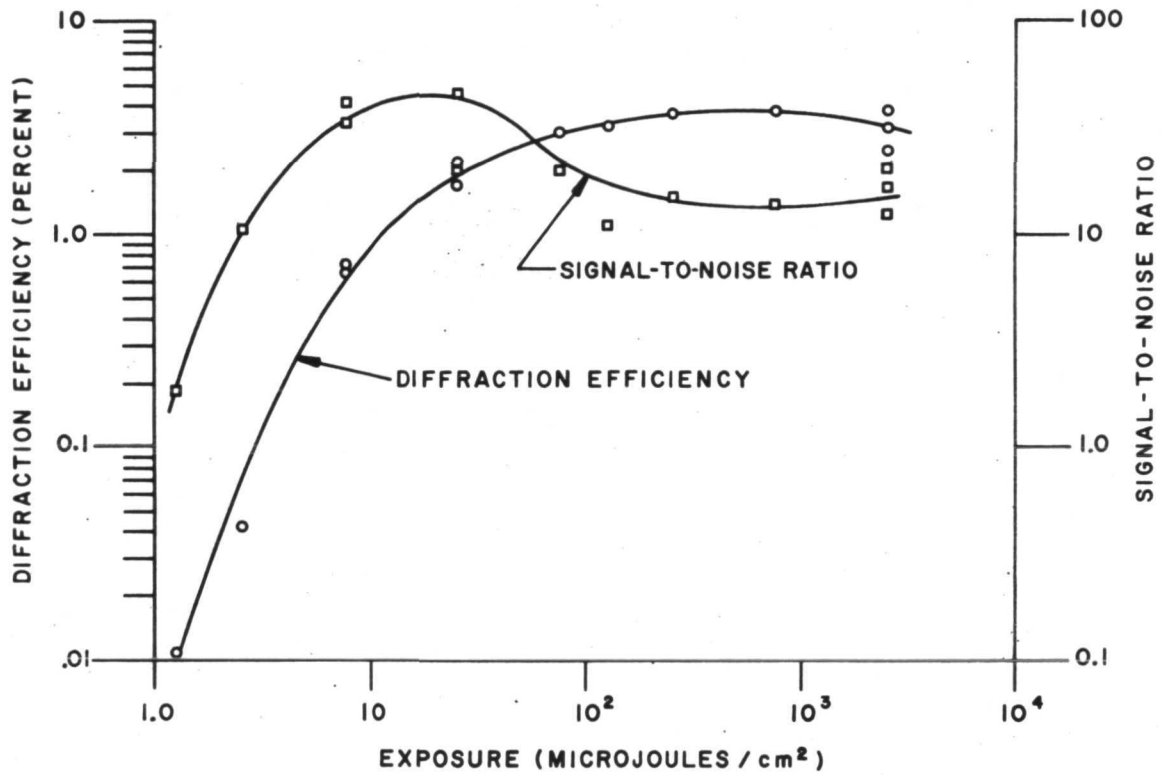A DIVISION OF HARRIS INTERTYPE CORPORATION

Figure 4-7. Diffraction Efficiency and Signal-to-Noise Ratio as a Function of Exposure for Photoplastic Hologram

We also measured the frequency response of photoplastic samples coated with the stabilized ester resin. This is shown in Figure 4-8, a curve of diffraction efficiency plotted as a function of spatial frequency for plane wave gratings recorded with various angles separating the beams. The thickness of the thermoplastic coating was approximately 0.4 µm. The curve illustrates the bandpass nature of the photoplastic device. The center frequency is about 850 lines/mm with a bandwidth of ±250 lines/mm.

The holographic response of the photoplastic materials varies slowly with exposure; it is much more sensitive, however, to the heat input in the development step. This is indicated in Figure 4-9, which shows the variation of diffraction efficiency and SNR with heat input. The heat input was varied by changing the power applied to the device; the development time was fixed at 130 ms. The data indicate that a change of 6 percent from the optimum voltage reduces the efficiency by 50 percent. We also found that the SNR peaks with the hologram slightly underdeveloped.

Figure 4-10 shows the variation of diffraction efficiency and SNR with corona potential. Although these data were obtained with corona charging, similar results are expected for parallel-plane charging.

4.4 Materials

We investigated the properties of four thermoplastics: The highly stabilized ester resin; a terpolymer of styrene, octyl methacrylate, and decyl methacrylate; a vinyl-toluene copolymer; and a hydrogenated form of the vinyl-toluene copolymer. These materials had somewhat varying characteristics; however, they all met the design goal of 500 record-erase cycles. We tested the cycling capabilities of the thermoplastics by recording and erasing holograms repetitively and periodically measuring the diffraction efficiency and SNR. These parameters began to decrease after several hundred to several thousand record-erase cycles.
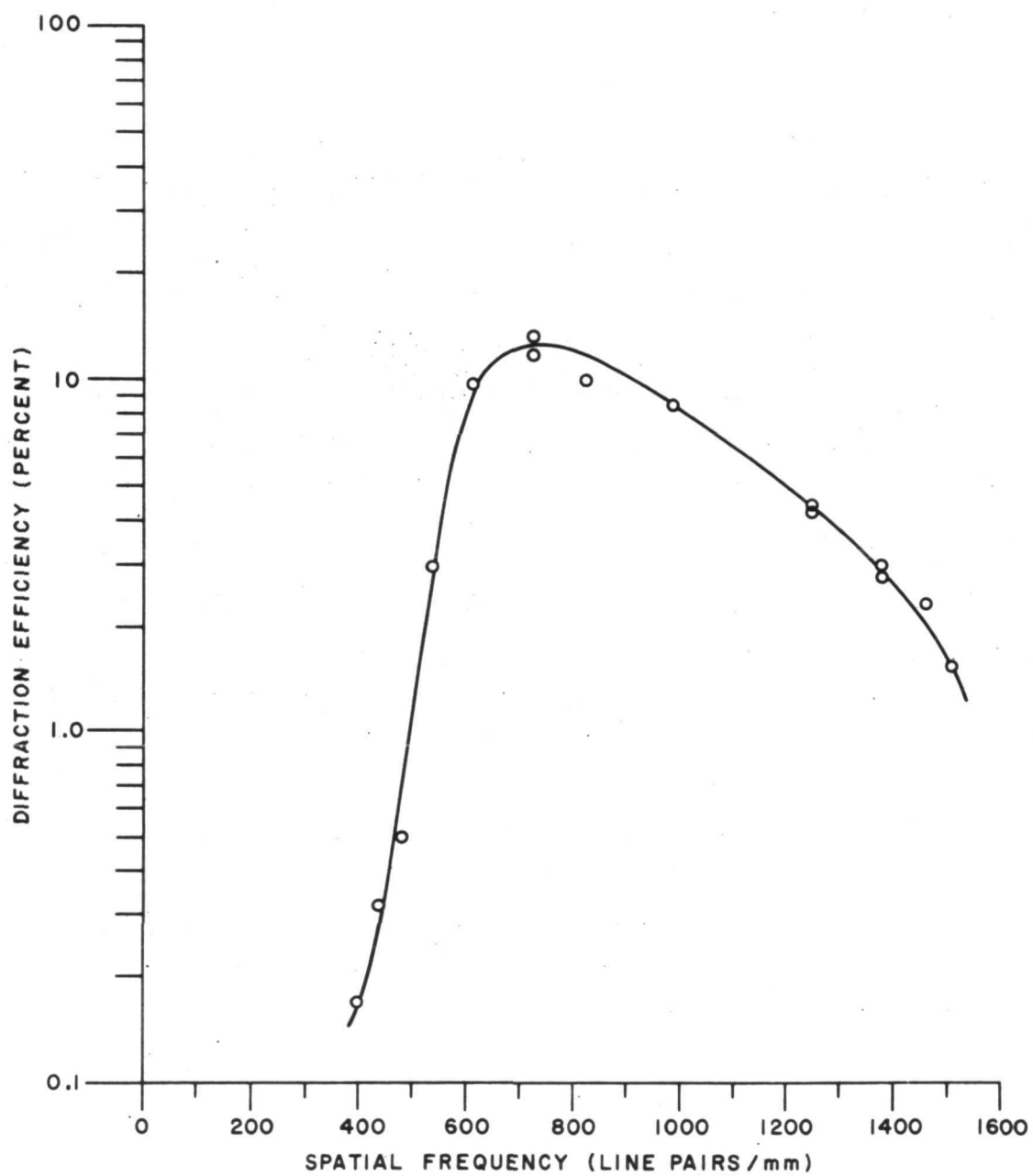
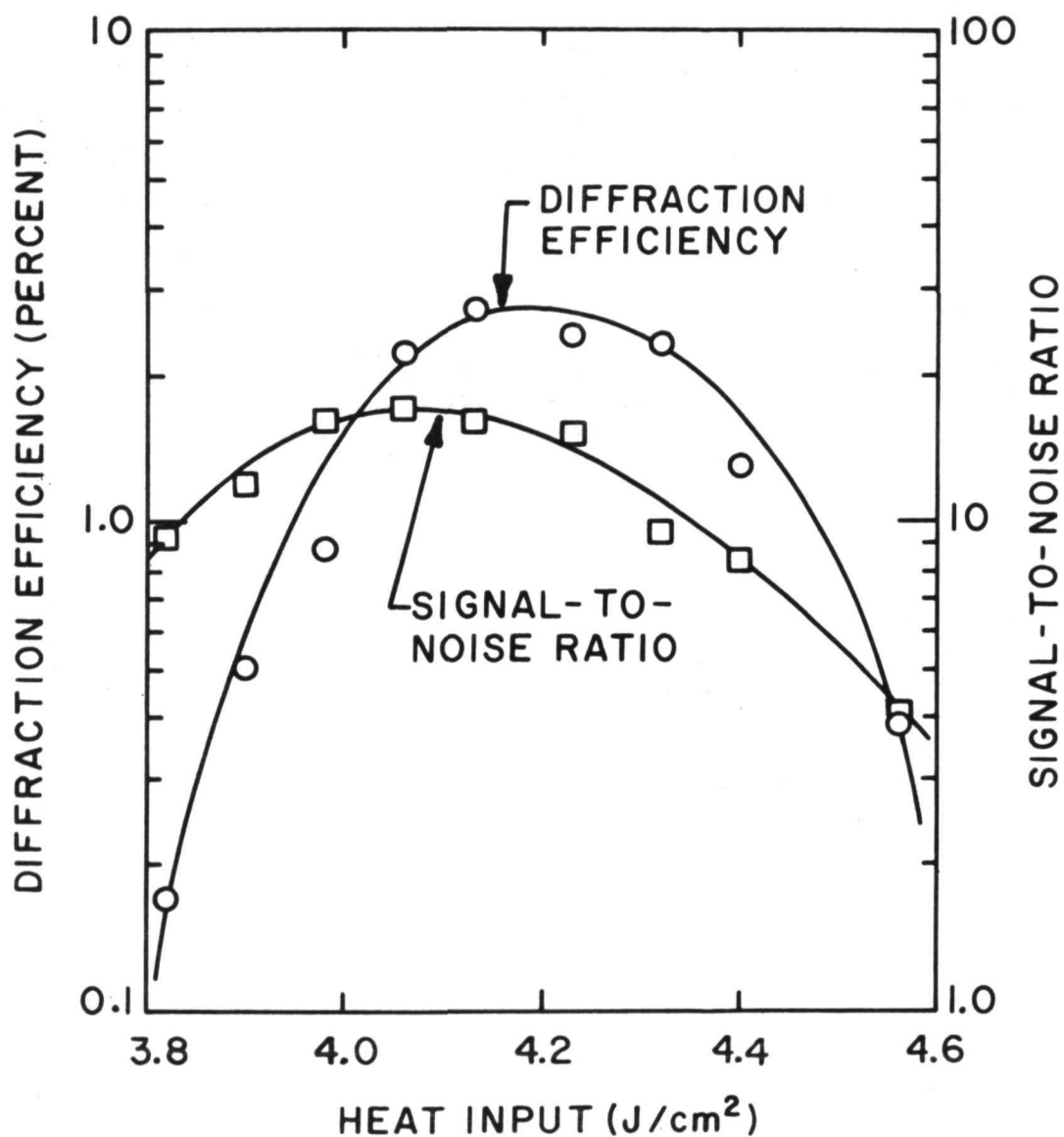Figure 4-8. Spatial Frequency Response of Photoplastic

Figure 4-9. Effect of Heat Input on Diffraction Efficiency
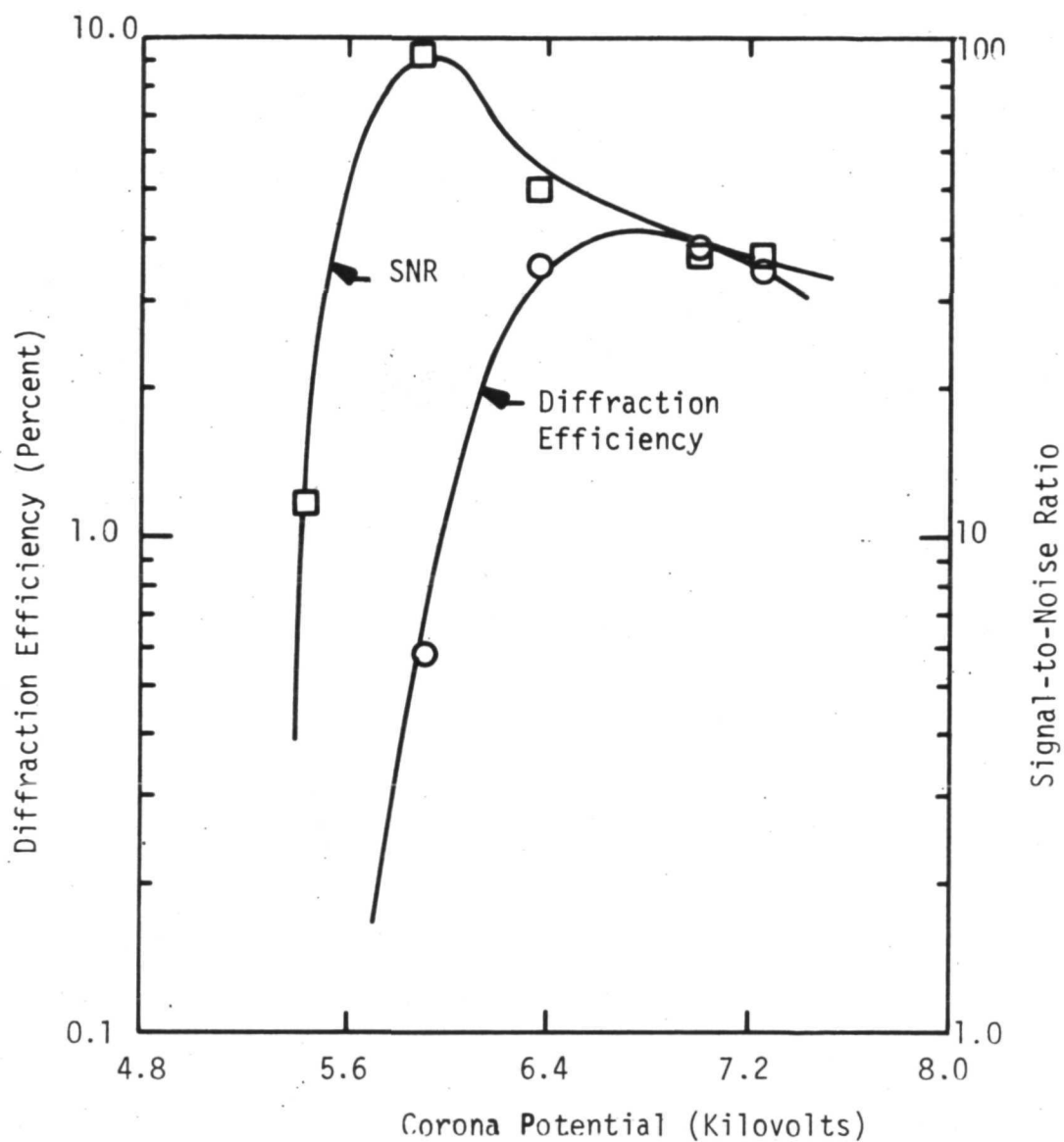and Signal-to-Noise Ratio

Figure 4-10. Effect of Corona Potential on Diffraction Efficiency
and Signal-to-Noise Ratio

We found that ozone generated by the charging system is a source of thermoplastic degradation. To determine this, we fabricated a special cell that enclosed the photoplastic and corona devices; input and output valves allowed the introduction of any desired gas so that the photoplastics could be tested with different environments. We tested a conventional photoplastic sample, coated with the ester resin thermoplastic, in a flowing nitrogen atmosphere and in nonflowing air.

With nonflowing air, we observed very rapid degradation of the thermoplastic. This degradation first appeared after about ten record-erase cycles as an increase in softening temperature. By the twentieth cycle, the softening temperature was increasing more rapidly and the diffraction efficiency began to decline significantly. We attribute the rapid degradation in air to ozone generated by the corona discharge. Unlike our standard photoplastic recording system, the special test cell concentrated the ozone to levels that led to rapid deterioration of the enclosed photoplastic device.

By comparison, the photoplastic materials were cycled well over a hundred cycles in a nitrogen atmosphere, with no apparent change in the softening temperature. However, the diffraction efficiency was relatively low. We suspect that this reduction is due in large part to the different charge transport mechanism in nitrogen and to some extent to lower recording intensity modulation since the holograms were recorded while the nitrogen was flowing.

Similar results were obtained with parallel-plane charging, although the comparison here was between air and argon, in both cases nonflowing. The diffraction efficiencies were comparable in this case, however. We conclude that if ozone is allowed to concentrate by the geometry of the charging apparatus, the lifetime of the thermoplastic will be relatively low. In the case of parallel-plane charging, the discharge region is enclosed, requiring the use of an inert atmosphere to prevent the premature degradation of the thermoplastic. Corona charging can be used in a relatively open geometry in which the concentration of ozone is minimized; most of our lifetime testing was carried out in this manner.

In working with several thermoplastics, we observed that some appear to accept charge more readily than others. We investigated the charge acceptance of the materials more fully by comparing the surface potential reached by each thermoplastic for a given amount of corona charging. Figure 4-11 shows the surface potential as a function of corona voltage for three thermoplastics. The methacrylate/styrene terpolymer has the greatest charge acceptance; 15 percent greater corona voltage is required to charge the vinyl-toluene copolymer to the same potential. Since the charge acceptance tends to increase at elevated thermoplastic temperatures, the thermoplastics were maintained at room temperature for these measurements.

The stabilized ester resin thermoplastic formed holograms with good diffraction efficiency and SNR. Figure 4-12 shows curves of diffraction efficiency and SNR as functions of the number of record-erase cycles for the ester resin when it was charged with the usual corona discharge device in air. The response is constant to about 200 record-erase cycles, after which it decreases until at 1000 cycles, the response is down by nearly 5 dB. Figure 4-13 shows the improvement realized by employing parallel-plane charging in an argon atmosphere. Here, the response was constant for 3000 record-erase cycles, at which time cycling was discontinued due to equipment problems. For this test, a small photoplastic device was placed within an argon filled cell; the argon pressure was maintained at several psi above atmospheric. The windows of the cell caused the low SNR by scattering and reflecting the incident light. The SNR of the hologram itself is higher, and in the case of the memory array, the two plates that form the parallel-plane photoplastic device are filled with argon and sealed, eliminating the need for the extra windows used in the lifetime tests. Although the holographic response was constant over the 3000 record-erase cycles, the softening temperature of the thermoplastic increased approximately 20 percent. We attribute the increase to crosslinking of the thermoplastic molecules, which causes a more sluggish response of the thermoplastic.
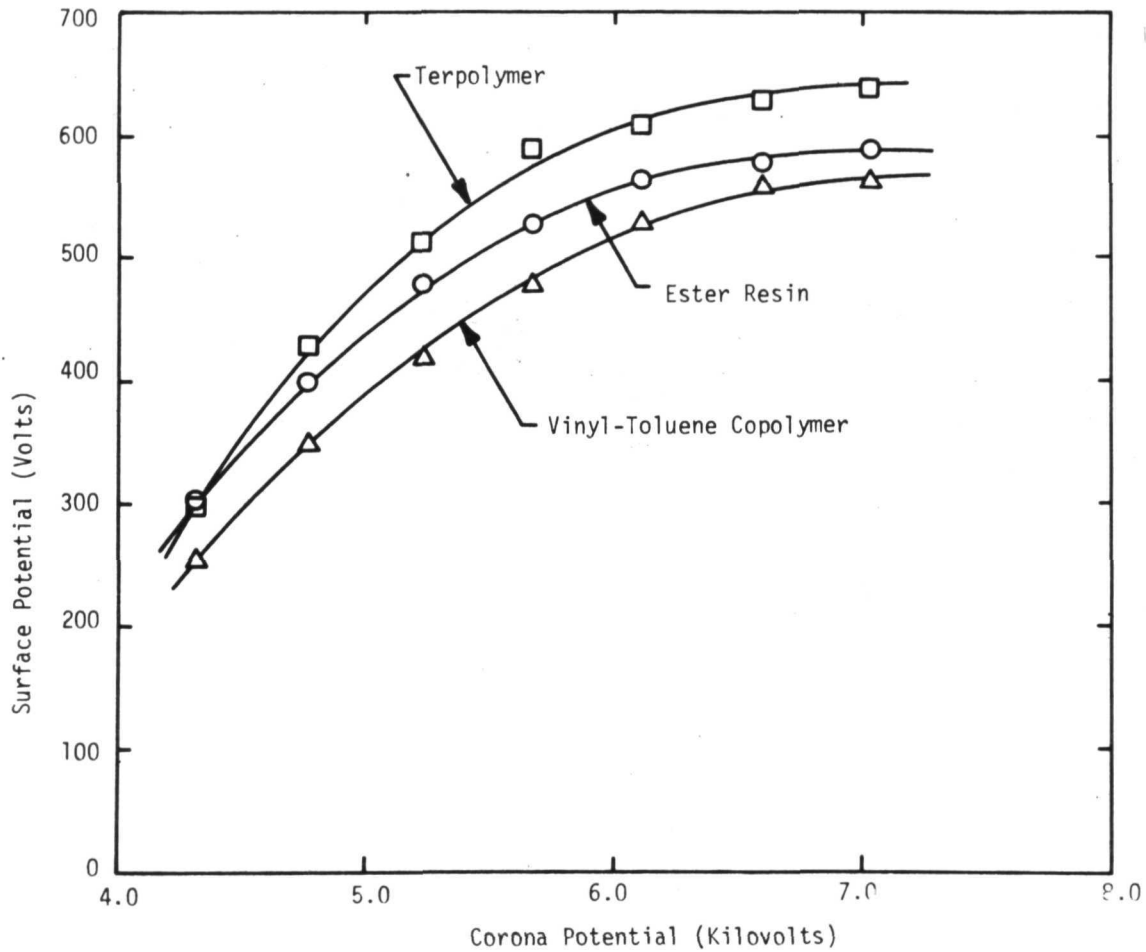
Figure 4-11. Charging Characteristics of Three Thermoplastics

RADIATION
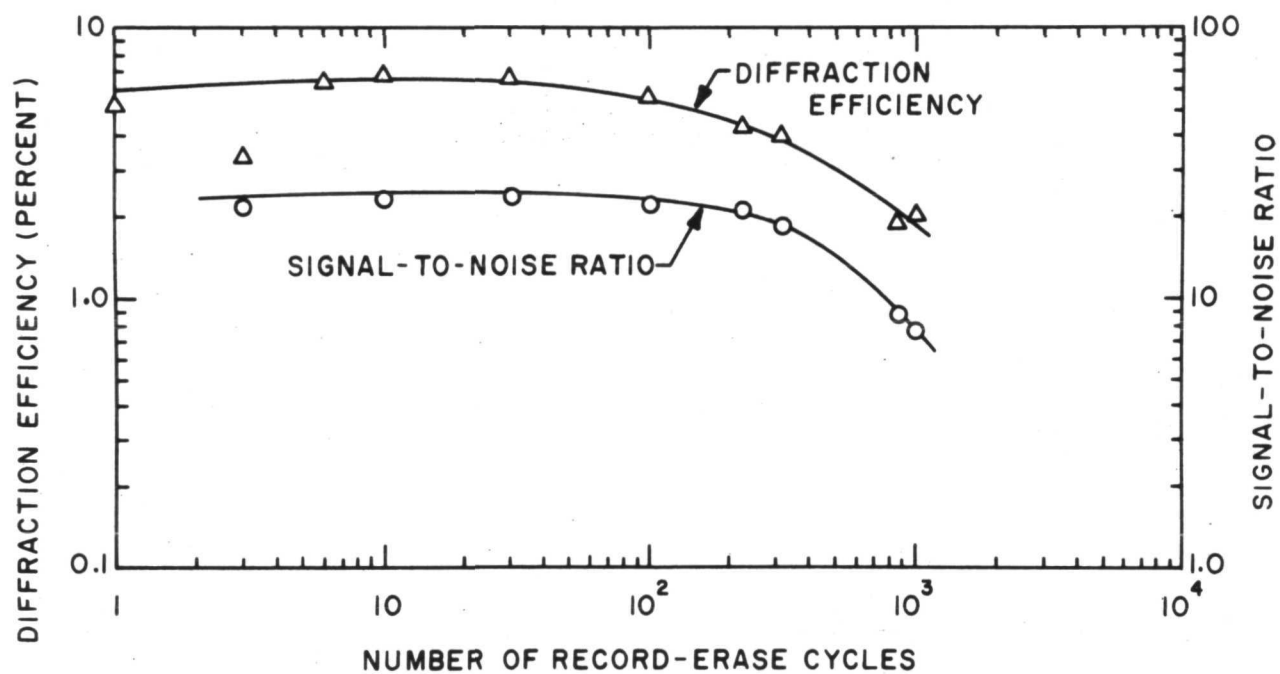A DIVISION OF HARRIS INTERTYPE CORPORATION

Figure 4-12. Cycling Characteristics of Ester Resin
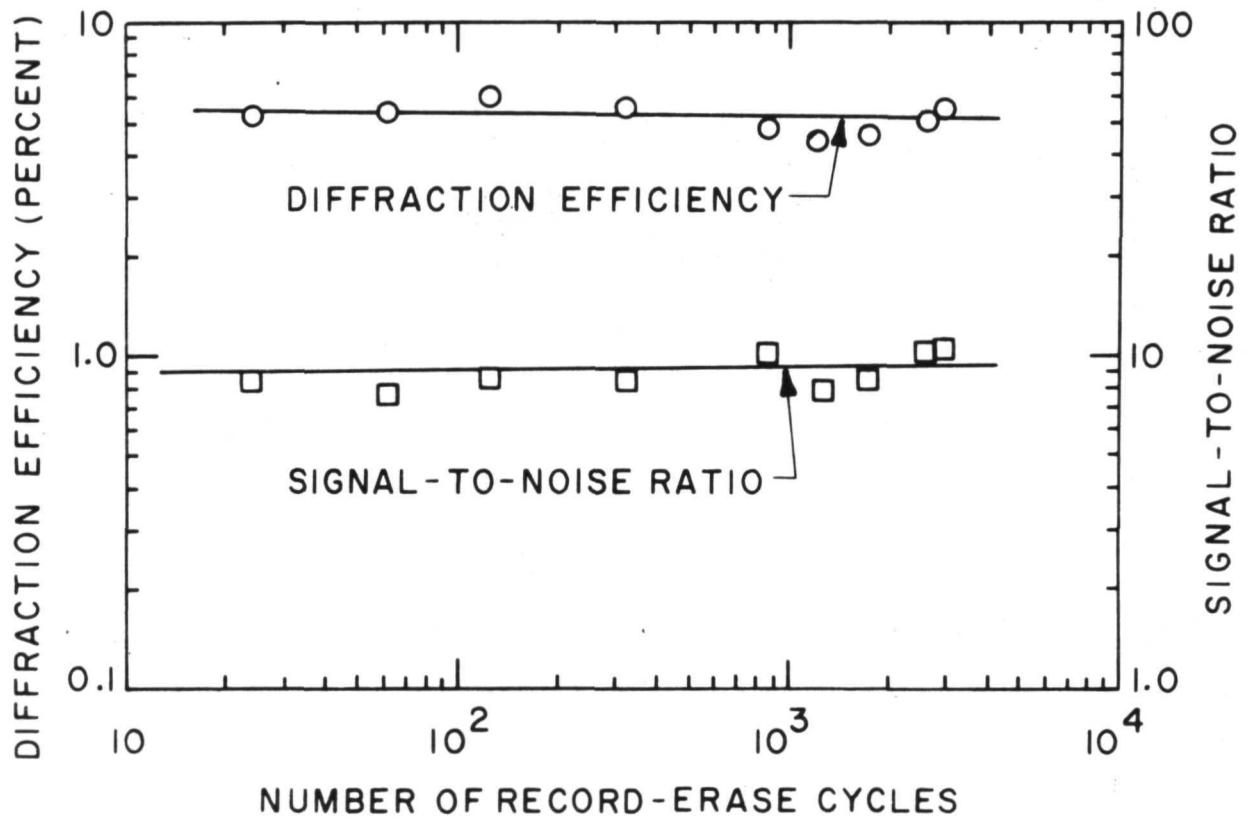with Corona Charging in Air

Figure 4-13. Cycling Characteristics of Ester Resin with Parallel-Plane Charging in Argon

The terpolymer of styrene, octyl methacrylate, and decyl methacrylate also formed holograms with good diffraction efficiency and SNR. The holographic response of this material over 4500 record-erase cycles is shown in Figure 4-14; charging was in air with the usual corona discharge device. Unlike the ester resin, the terpolymer maintained a constant softening temperature throughout the test. Coatings of this material are more difficult to prepare, however, and in one case the thermoplastic slowly deteriorated in the dipping solution.

The vinyl-toluene copolymer formed holograms with lower diffraction efficiency but with very high SNR. This is illustrated by Figure 4-15 which shows the holographic response for 3000 record-erase cycles with corona charging in air. The low diffraction efficiency may be due in part to the low charge acceptance of this thermoplastic, as shown in Figure 4-11. At lower diffraction efficiencies (about 0.1 percent), the lifetime is better; under these conditions, this material has withstood 8600 record-erase cycles with little deterioration except for crosslinking which caused the softening temperature to rise. Figure 4-16 shows photographs of the reconstructed image after 1500, 7500, and 8600 record-erase cycles. As is evident from these results, there is no significant decrease in SNR as the number of cycles increases. Figure 4-17 shows successive reconstructed images from one sample, demonstrating that it is possible to record and read out successive holograms with little or no interaction between them. The images were obtained from 7504, 7505, 7506 and 7507 cycles; the effect of latent imagery is negligible even after such a large number of cycles.

A hydrogenated form of the vinyl-toluene copolymer formed holograms with higher efficiencies and exhibited similar cycling characteristics. Figure 4-18 shows the holographic response for 9300 record-erase cycles of a photoplastic device coated with this thermoplastic. This cycling test was carried out with corona charging in air.

The photoconductor used in these experiments was polyvinylcarbazole (PVK) sensitized with trinitrofluorenone (TNF) at a weight ratio of 1 part TNF to 10 parts PVK.
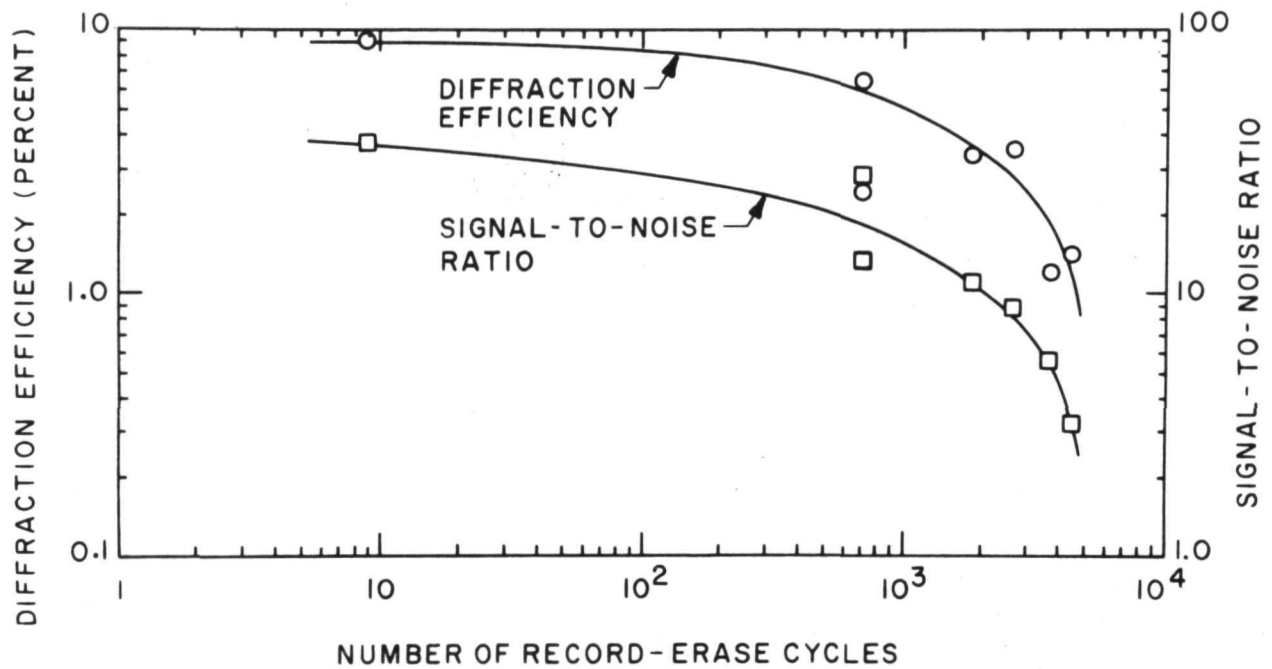
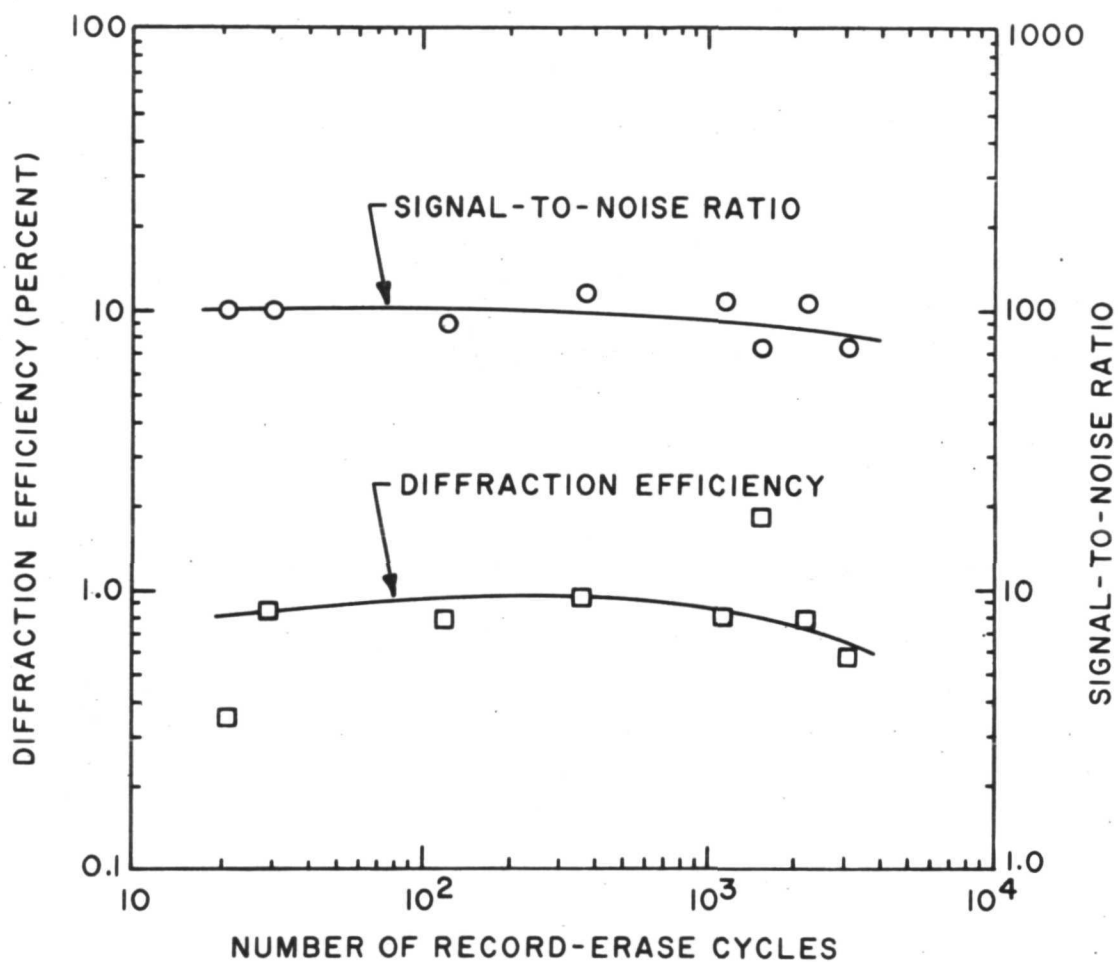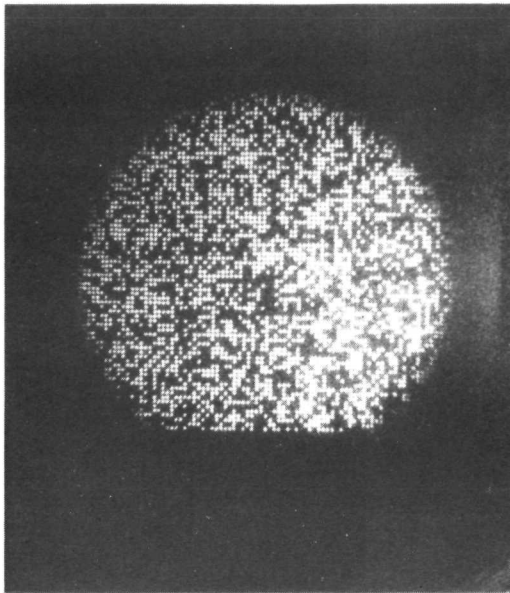Figure 4-14.   Cycling Characteristics of Terpolymer with Corona Charging in Air
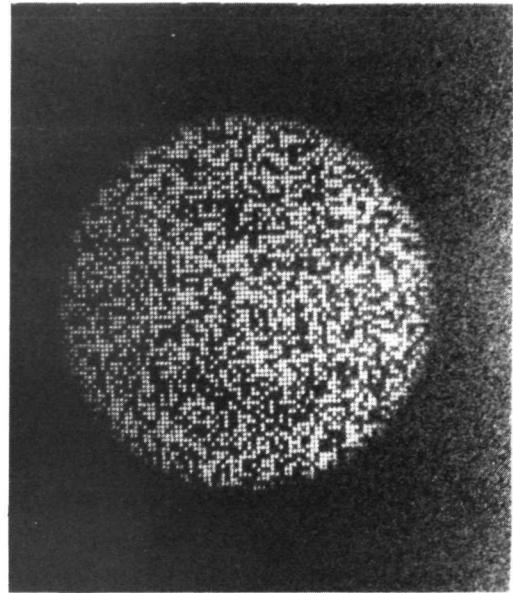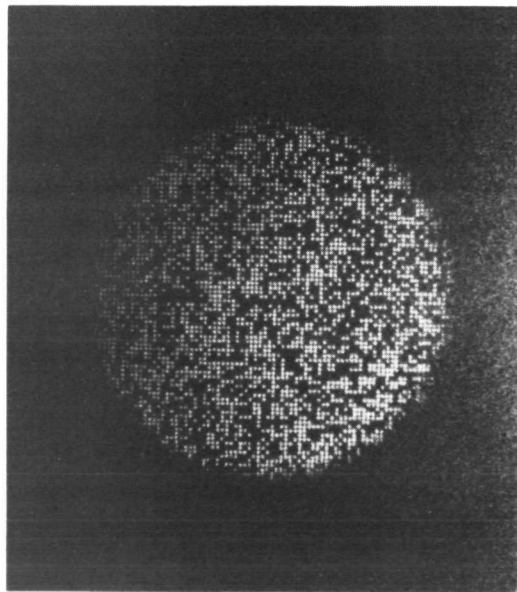
Figure 4-15. Cycling Characteristics of Vinyl Toluene Copolymer with Corona Charging in Air

1500

7500

8600

Figure 4-16. Photographs of Reconstructed Images from
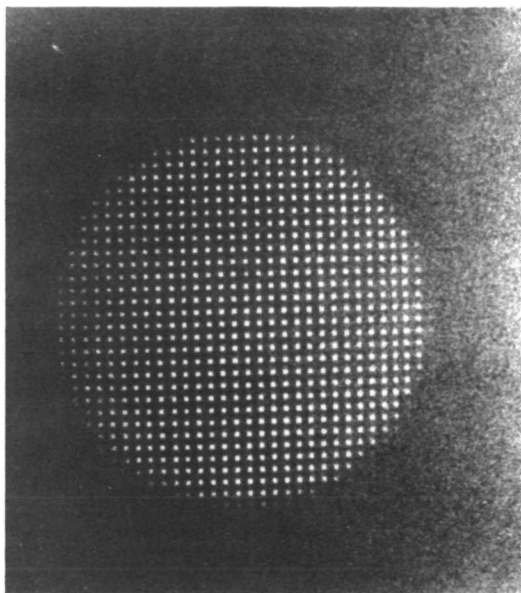Holograms after 1500, 7500 and 8600 Cycles
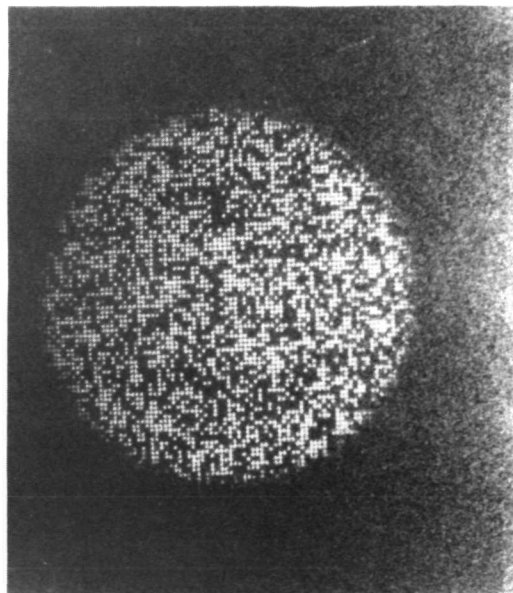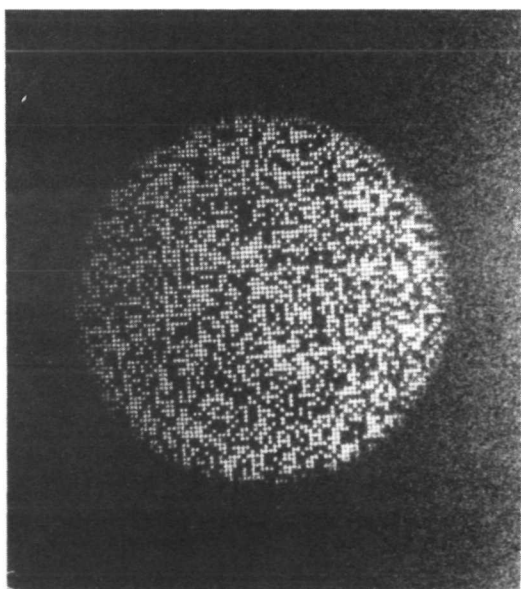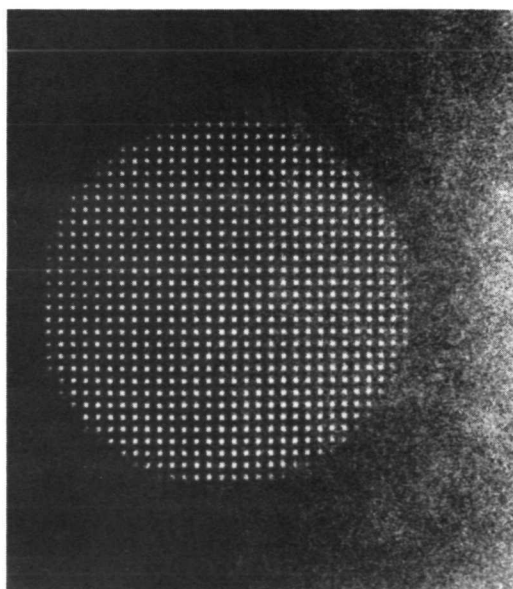
RADIATION
A DIVISION OF HARRIS INTERTYPE CORPORATION

7504

7505

7506

7507

Figure 4-17. Photographs of Reconstructed Images from Holograms
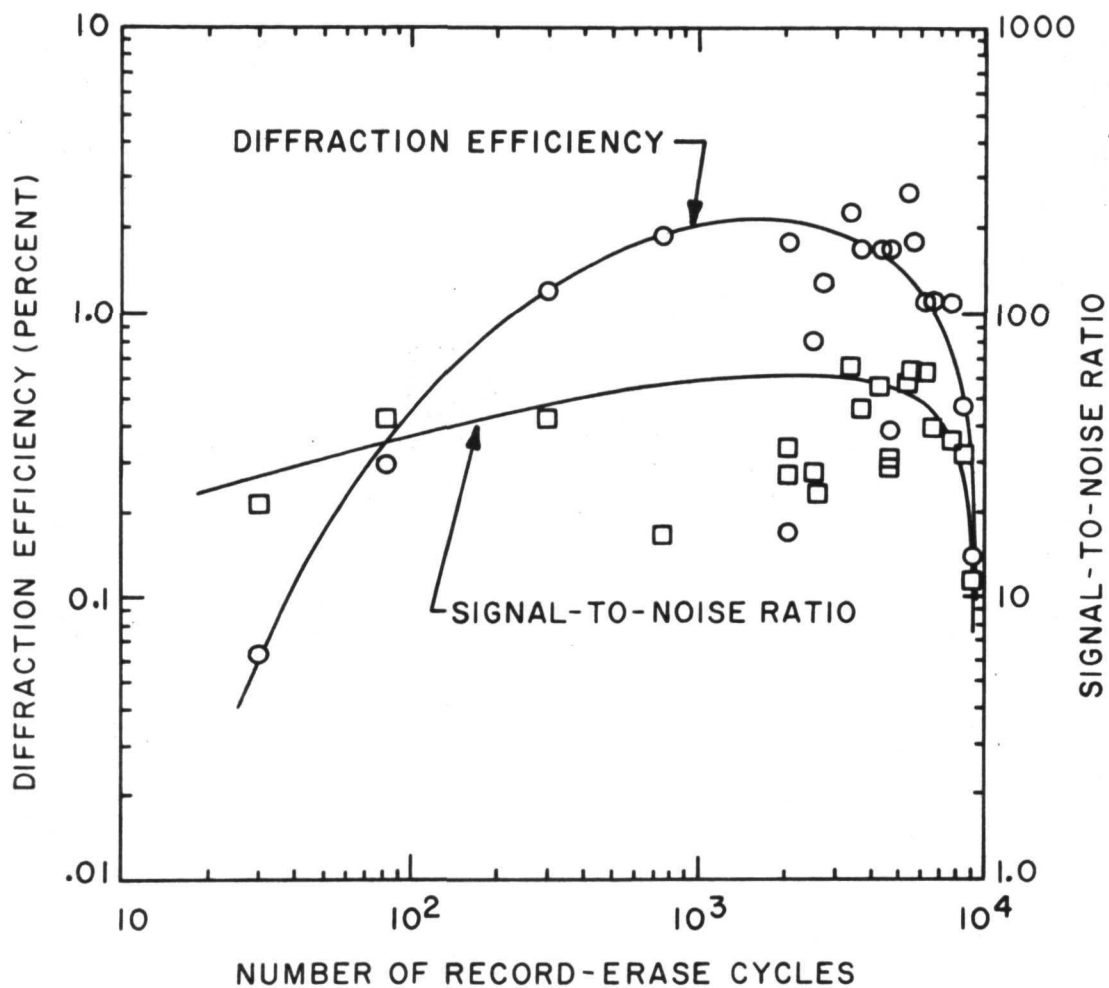after 7504, 7505, 7506 and 7507 Cycles

Figure 4-18. Cycling Characteristics of Hydrogenated Vinyl Toluene
Copolymer with Corona Charging in Air

The major investigations involving the photoconductor were directed toward discovering the cause and techniques for prevention of latent images. The latent (or hidden) image is an image of a previously erased hologram that reappears after simply recharging and redeveloping the photoplastic device. It is undesirable because its appearance in subsequent holographic recordings obscures the desired information and reduces the SNR of the reconstructed image. Under certain conditions, its intensity is comparable to that of the original diffracted image. Although we have not succeeded at completely eliminating the latent image, we have managed to reduce its intensity to low levels.

We believe that the latent image is the result of immobilized, or sluggish, electrons in the bulk region of the photoconductor. The mobility of electrons in PVK-TNF is a function of the TNF concentration, and at the concentration we normally use, is three orders of magnitude less than the hole mobility.[14] The immobilized electrons drift extremely slowly across the photoconductor layer so that they are likely to be present in sufficient numbers after a hologram is erased to interfere with the subsequent recording by causing some modulation of the charge distribution. Thus, measures which tend to increase the electron mobility should lead to a reduced latent image intensity.

There are several possible techniques for raising the electron mobility. Raising the temperature of the photoconductor increases the mobilities of both holes and electrons; this can be accomplished by increasing the length of the erase pulse. Illuminating the photoconductor with light of uniform intensity prior to erasure, generates enough hole-electron pairs to overwhelm the existing immobilized electrons and decrease the variation in their distribution. Finally, by increasing the TNF concentration, we can increase the electron mobility. For example, doubling the usual TNF concentration increases the electron mobility by an order of magnitude.

To test our hypothesis and the techniques for eliminating the latent image, we carried out a number of tests with plane wave gratings recorded on a photoplastic device. The device was coated with our standard materials: PVK sensitized with TNF at a ratio of 10 parts by weight PVK to 1 part TNF for the photoconductor, and the ester resin thermoplastic. Measurements were made for a reference-to-signal beam ratio of unity at an offset angle of 20 degrees and a wavelength 633 nm.

Figure 4-19 shows the effect of erasure time (and, thus, the temperature reached during erasure) on the magnitude of the latent image. The quantities plotted in the curve are defined as follows:

$$\text{Relative latent image intensity} = \frac{\text{Latent Image Intensity}}{\text{Original Diffracted Image Intensity}}$$

$$\text{Normalized Erase Time} = \frac{\text{Erase Time}}{\text{Development Time}}$$

The same voltage amplitude was used for development and erasure; only the length of the heating pulses was varied. Figure 4-19 also shows that the intensity of the latent image is affected by the corona potential. As can be seen from the figure, a sufficiently long erasure time can reduce the relative latent image intensity to less than one percent. This represents a brute force approach and is likely to hasten deterioration of the device due to thermal degradation of the thermoplastic. Figure 4-20 shows the effect of uniformly illuminating the photoconductor before and during erasure. The illumination reduces the latent image intensity by more than an order of magnitude, and significantly reduces the erasure time required to reduce the relative latent image intensity to one percent.

We found that doubling the TNF concentration decreased the latent image intensity by about an order of magnitude (as well as increasing the sensitivity by the same amount).
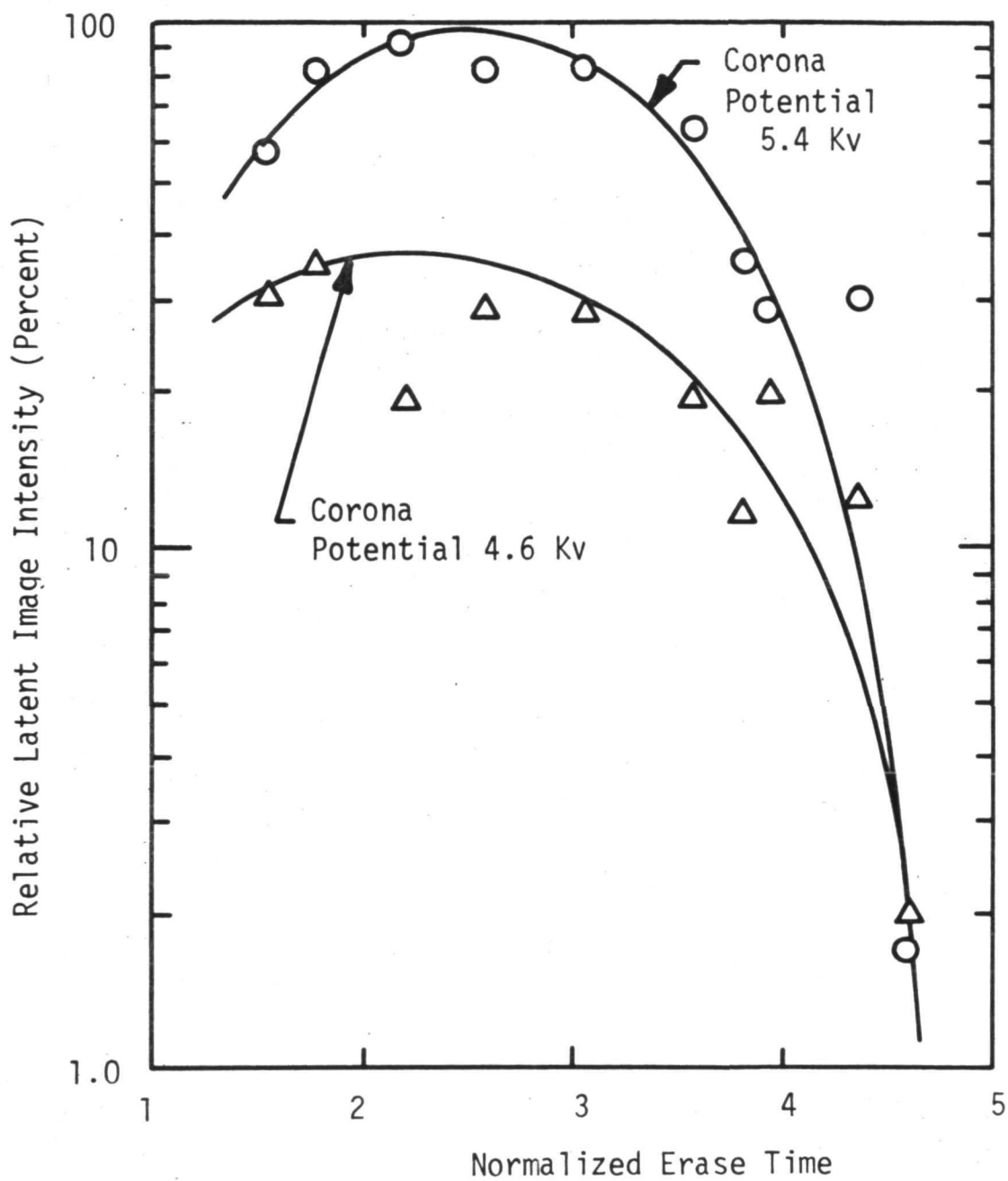
RADIATION
A DIVISION OF HARRIS INTERTYPE CORPORATION

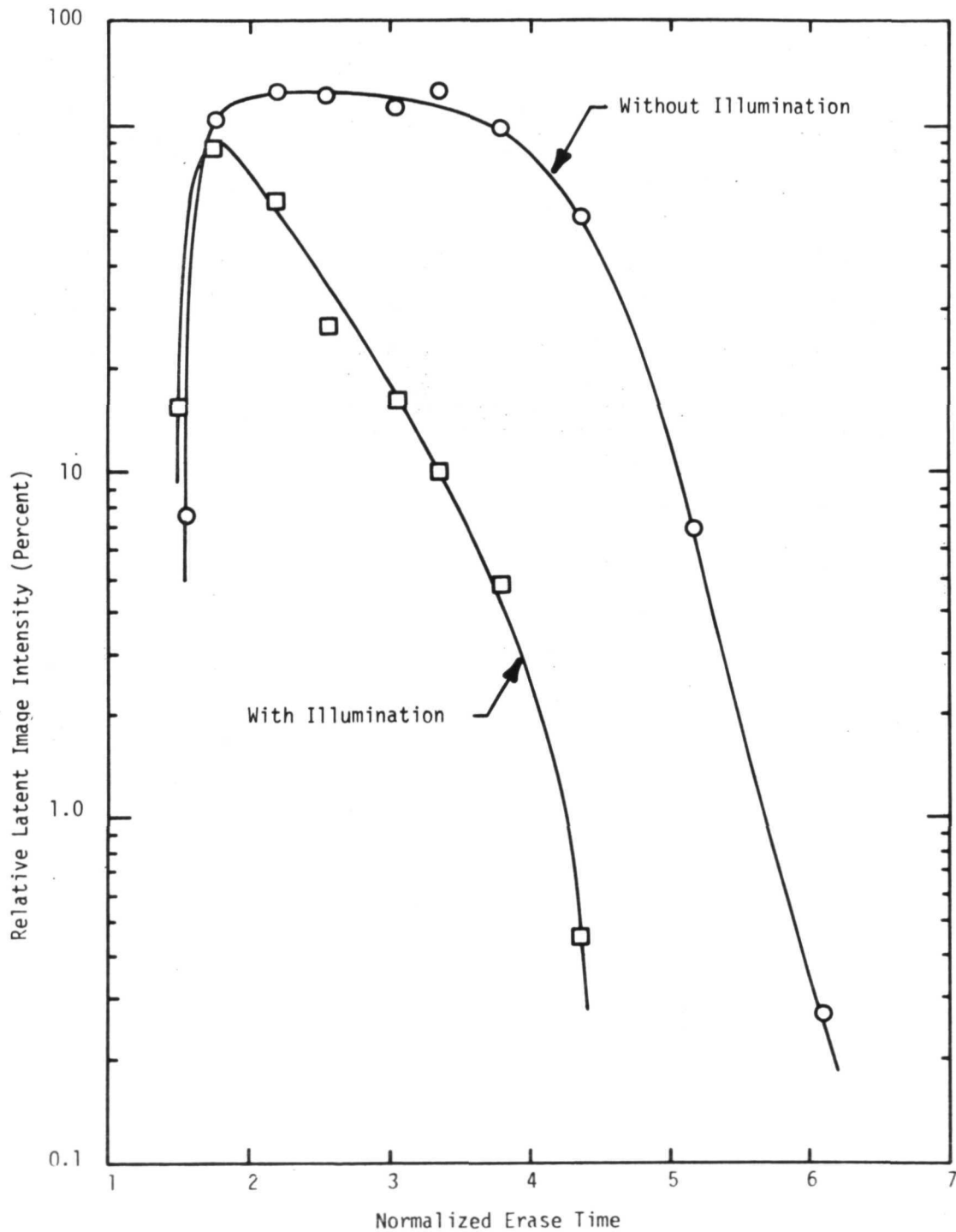Figure 4-19. Effect of Erase Time on Latent Image Intensity

Figure 4-20. Effect of Illumination on Latent Image Intensity

4.5 Mounting Fixture and Hologram Array

We designed and fabricated a new mounting fixture to take advantage of the parallel-plane charging technique. This permitted a slightly more compact fixture, using approximately one-tenth the voltage required for corona charging. In addition, the high voltage is completely enclosed, permitting safer operation of the system. The volume between the hologram array and the charging plate is evacuated and filled with argon prior to use. The argon atmosphere not only extends the life of the thermoplastic, but also eliminates such troublesome variables as ambient relative humidity and dust conditions. Electrical connection to the hologram plate electrodes is made with pressure point contacts; these are also enclosed by the fixture. Figure 4-21 shows a cross-section of the new mounting fixture; a photograph of the fixture is shown in Figure 4-22.

The photoplastic array is a submatrix array with holograms recorded on each submatrix. The submatrix is a 30 mm long, narrow rectangular strip on which a group of 20 holograms are individually recorded but simultaneously developed or erased. A photograph of the array and electrode layout is shown in Figure 4-23.

The hologram arrays were fabricated by the Hybrid Microelectronics Laboratory of Radiation. The spotting silver electrodes of the previous arrays were replaced with electrodes of nickel, copper, and gold. Because the new electrodes are thinner (less than 1 μm), variations in the photoplastic coating thickness near the electrode edges are minimized. The fabrication procedure begins with detergent cleaning of the indium oxide coating on a glass plate. Electroless nickel is deposited on the indium oxide, for mechanical adhesion, followed by a layer of electroplated copper for high electrical conduction. The active area is then masked with photoresist and the electrode pattern is etched in the copper, nickel, and indium oxide. The hologram locations are formed by removing the copper and nickel from the indium oxide strips. Finally, a thin gold layer is deposited over the copper to prevent oxidation.
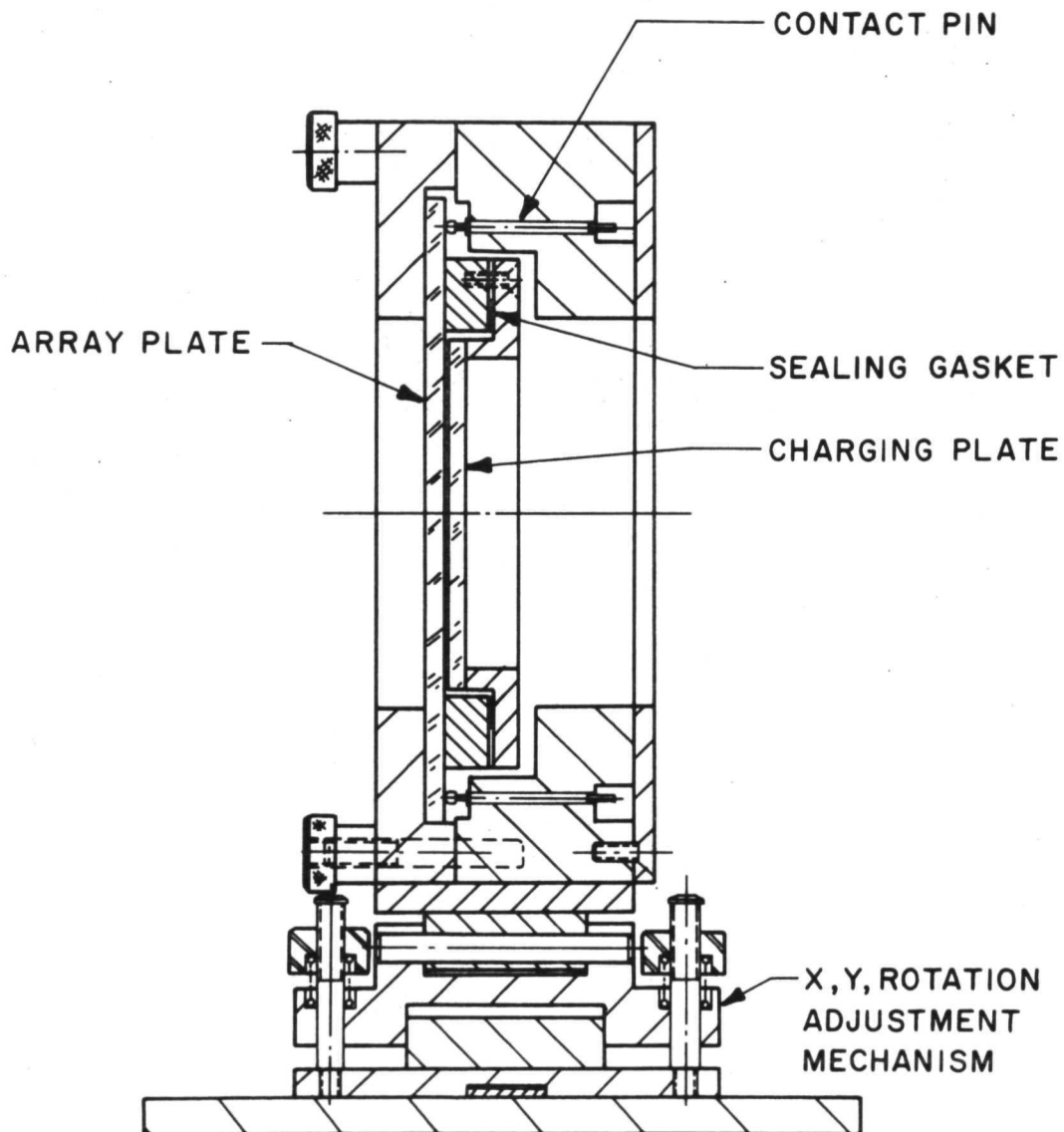
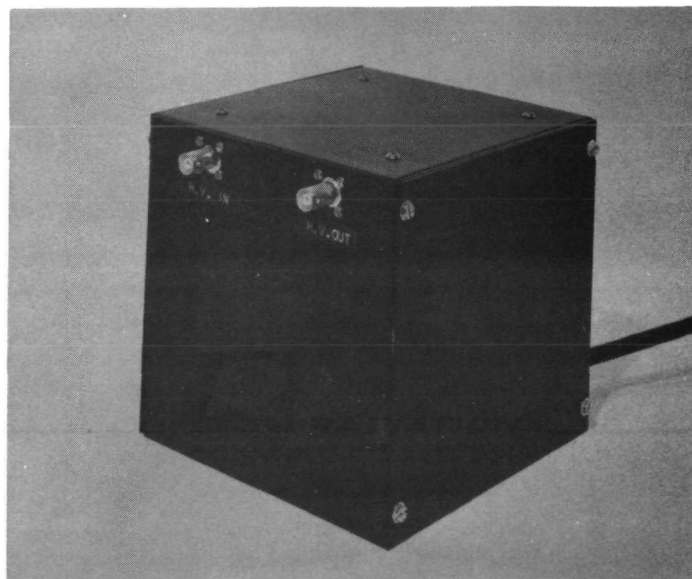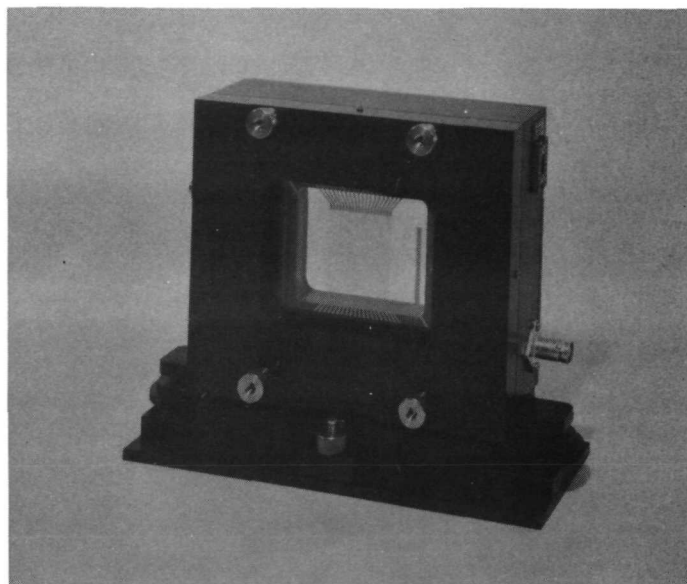Figure 4-21. Mounting Fixture for Hologram Array

Figure 4-22. Photoplastic Mounting Fixture With Array (Top)
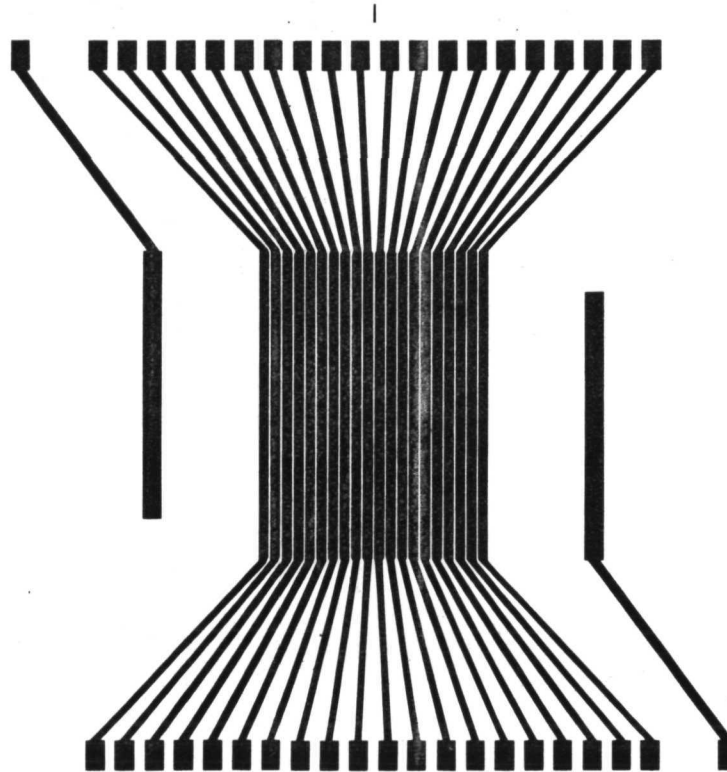High-Voltage Charging Unit (Bottom)

Figure 4-23. Hologram Strip and Electrode Configuration. The Outer
Two Electrodes Make Contact to the Charging Plate.

The rectangular strips are placed on 1.5 mm centers to be compatible with the present optical design of the test-bed system. The strip has finite dimensions and during a heat pulse there is a temperature gradient at the edges. Therefore, the edges of the strip are lower in temperature than the central portion and the hologram is developed only in the central portion of the strip. The strip width was selected to provide a 1 mm region of uniformity. A second edge effect occurs during erasure and affects the region adjacent to the pad being developed. During the longer erase heat pulse, the lateral heat flow in the glass substrate can cause a region outside the pad to reach the development temperature and form a permanent band of frost. The frost appears as a narrow band outside the strip running parallel to the edge of the strip. The lateral heat flow in the glass substrate can be reduced by applying the same thermal energy in a shorter time period. If the heat pulse is narrowed and increased in amplitude, the edge effects are reduced, allowing a larger useful aperture on the same center spacings. Therefore, the array was fabricated using 1.4 mm wide strips on the 1.5 mm center-to-center spacing; tests demonstrated that the edge effects were reduced to tolerable levels. Figure 4-24 is a photograph of the permanent frost pattern formed in the gap between the array strips by a short erase pulse; the lines represent the strip edges which are 100 µm apart. The frost does not reach the edges of the 1 mm hologram aperture located within the strip.

The diffraction efficiency, signal-to-noise ratio and uniformity of holograms recorded along a strip were evaluated. Using a charging wire and shield corona, we obtained diffraction efficiencies of 5 percent. However, perturbations in charging, exposure and heating caused a 3 dB variation in diffraction efficiency along a 30 mm strip. This random variation is shown in Figure 4-25, which is a plot of diffraction efficiency as a function of hologram location in a typical 30 mm strip.
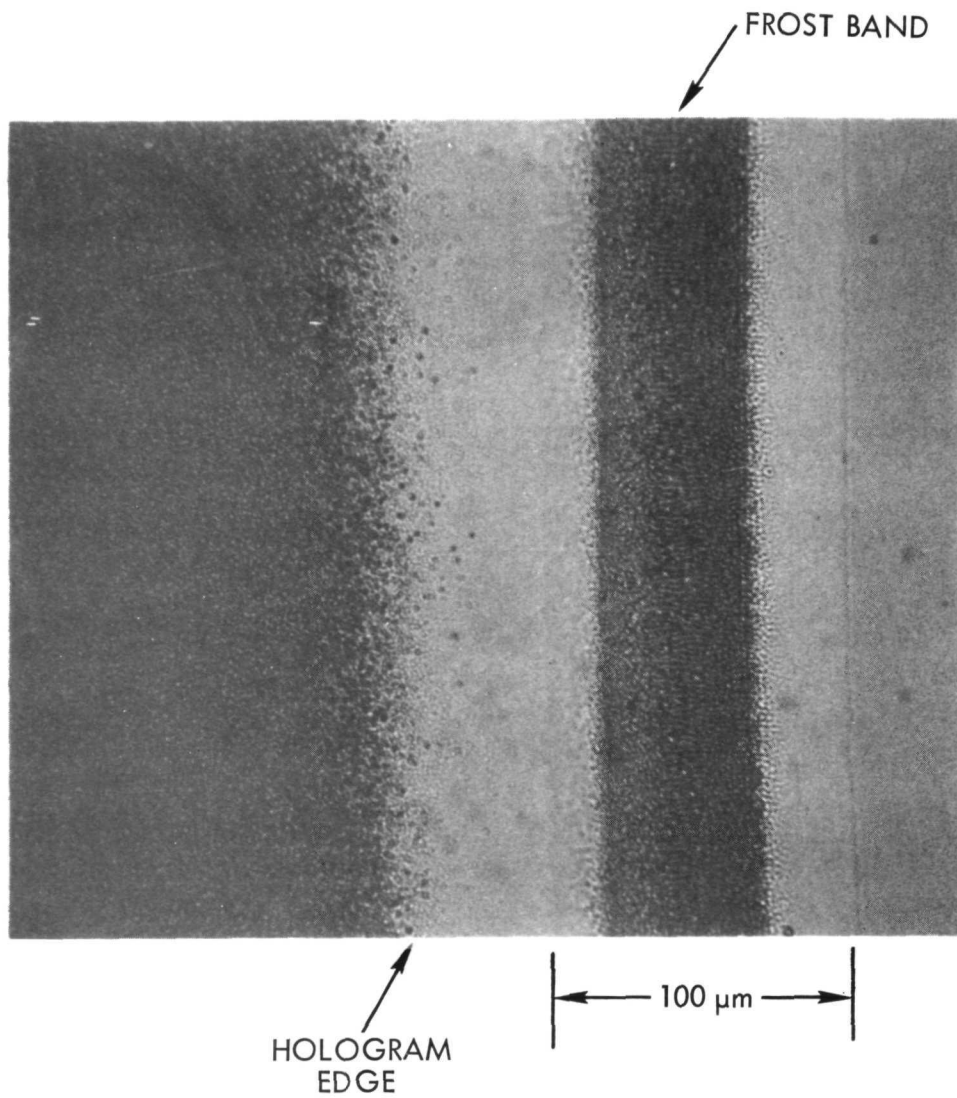
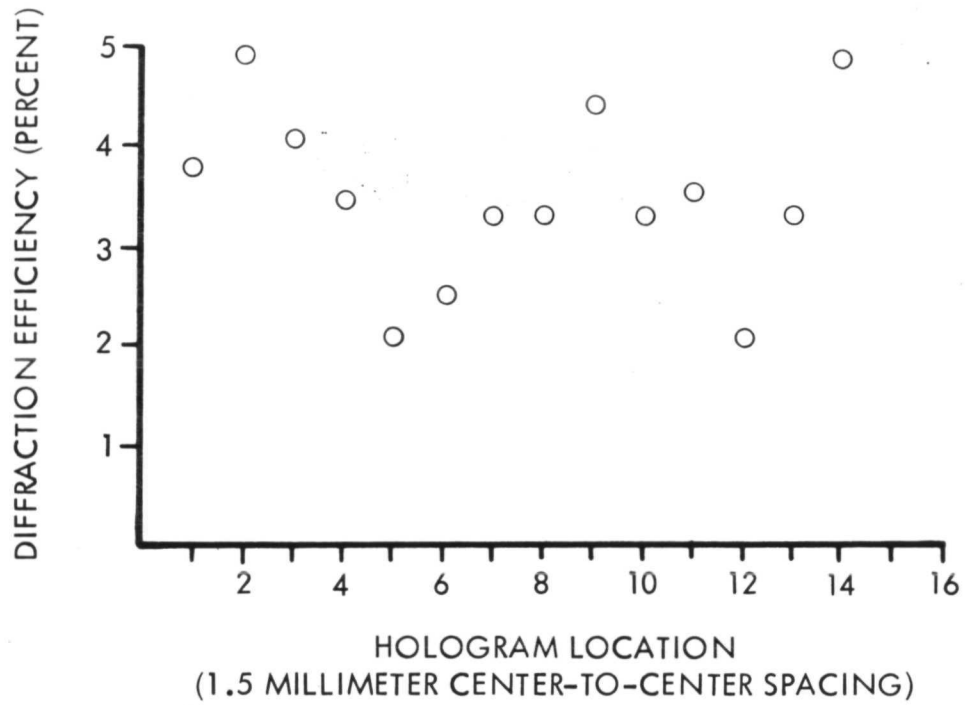Figure 4-24. Thermal Edge Effects in Strip Holograms

RADIATION
A DIVISION OF HARRIS · INTERTYPE CORPORATION

Figure 4-25. Diffraction Efficiency of Strip Hologram

We reconstructed 128 x 128 bit pattern images from near Fourier transform holograms that were recorded on strip arrays located approximately 2 mm behind the transform plane. Figure 4-26 is a photograph of a reconstruction from a 1.4 mm wide strip. The hologram was reconstructed with a 1 mm diameter beam with a wavelength of 488 nm. The SNR of the image is greater than 10 dB, as shown in Figure 4-27 which is a photomultiplier scan of the hologram reconstruction shown in Figure 4-26.

4.6 Photoplastic Array Drive Electronics

We describe the high voltage and the hologram array heater control circuit below.

4.6.1 <u>High Voltage Control Circuit</u>. - In order to facilitate a parallel-plane charging technique, we built a new high voltage switch and power-supply to replace the existing Hipotronics supply. Figure 4-28 shows the circuit which uses a relay as the switching element. A relay was chosen since it can operate in 1 to 2 mS which is compatible with other times in the system and furthermore it has switch voltages up to 5000 V giving it considerable operational advantages over semiconductor switches. The circuit interfaces with the controller as before via P76 but requires an input from a high voltage power supply. The power supply provided is a Hewlett-Packard 6515A supply which offers a regulated variable voltage output between 0 to 1600 V and gives a greater degree of flexibility and regulation than Hipotronics supply.

4.6.2 <u>Hologram Array Heater Control Circuit</u>. - An improved technique of heating the hologram pads has been developed. Instead of heating the pads with ac, dc is used to
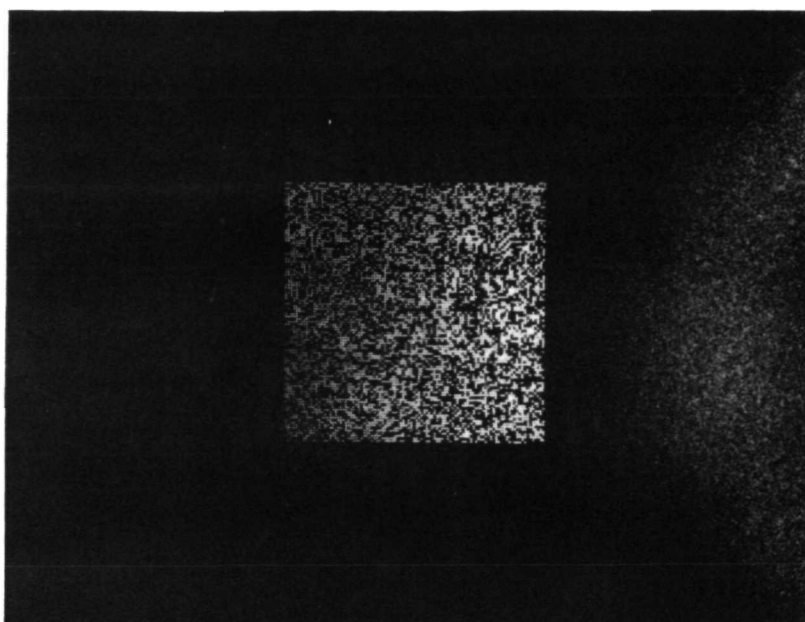
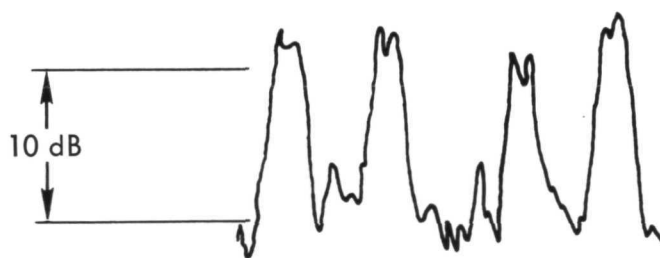Figure 4-26. Reconstruction from 1.28 mm Hologram

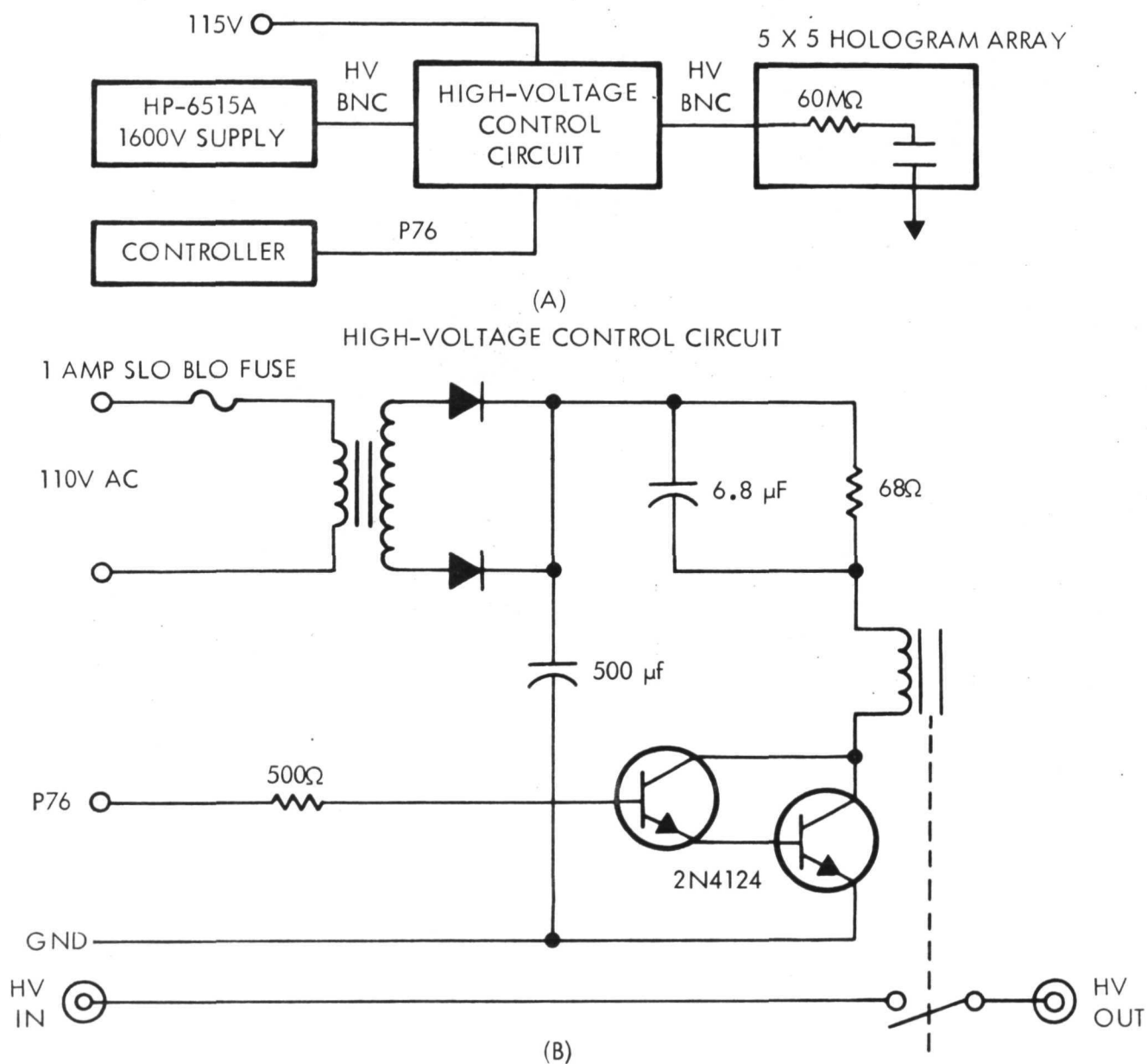Figure 4-27. Photomultiplier Scan of Reconstructed Bits

Figure 4-28. Block Diagram of High-Voltage Charging Circuit (A)
With Schematic of High-Voltage Control Circuit (B)

eliminate the half cycle uncertainty associated with switching of the ac. The half cycle uncertainty occurs during switching: it is necessary to wait for the line voltage to reach a zero point of its cycle before the triac can be turned off, limiting timing resolution to 8 ms. A further improvement has been to ground each pad and the corona shield, ensuring a low impedance path to ground preventing an undesired charge buildup on the hologram array.

The circuit is shown in Figures 4-29a and 4-29b. Figure 4-29a is a simplified equivalent circuit demonstrating the switching technique. The series switch S1 is an override control which ensures that, in the event of a programmer error, the pads cannot be overheated. PS No. 1 and PS No. 25 are the 25 pad switches. Each of the 26 switches are controlled from the computer interference unit in such a way that only one pad can be on at a time. The time that each pad switch is on is controlled by the program.

Since each switch design is identical, only one will be described in detail (see Figure 4-29b). Power is applied to pad No. 1 when series switch S1 and transistors TR1 and TR2 are all conducting. Switch-on occurs when the output of the 75450 driver goes high, turning on TR1. The collector current in TR1 is limited by the 150-ohm resistor to 12 mA which is sufficient to saturate TR2 with a collector current of 150 mA. Since TR2 is a PNP transistor, the supply voltage can be varied over a large range TR2 remaining in saturation and most of the supply voltage reaching the pads. During the "off" period, TR2 is cut off by the 2.7K ohm resistor in the voltage line V and the diode in the emitter circuit. Line V_1 is a common line to all the following pads further ensuring that all open switches are "hard off."

These modifications ensure a reliable, accurate and repeatable method of controlling the heating process.
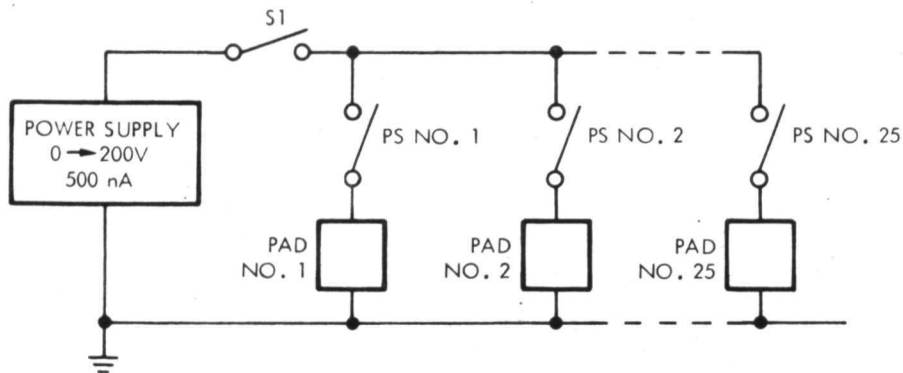
A. EQUIVALENT CIRCUIT OF HEATER CONTROL
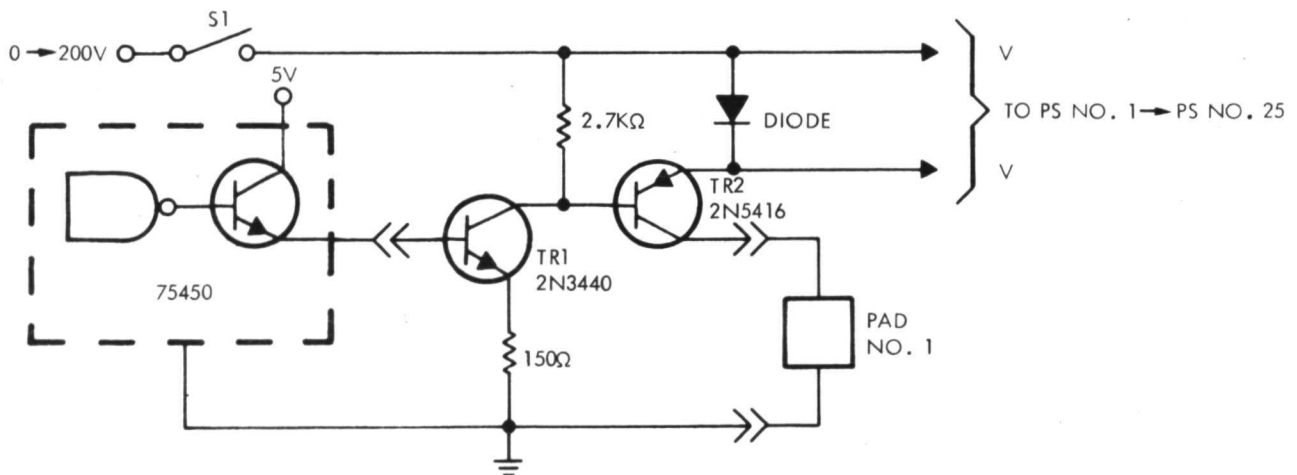
B. DETAILED CIRCUIT OF PAD SWITCH PSI

Figure 4-29. Control Electronics

SECTION V
MATERIAL DEVELOPMENT

There are three major tasks under the material development, continuing validation of the thick phase material computer model, fabrication of a holographic optical element, and monitoring of Battelle holographic material programs. During the first task we compared the experimental data from thick plastic holographic materials we are developing with the computer model. This task was very limited as few thick materials are available from which to obtain experimental data.

During the second task we fabricated two holographic elements which can be used to replace the 5 x 5 or the 20 x 20 lenslet array on the breadboard memory system.

During the third task we monitored the efforts of Battelle in developing a cis-trans isomer or a doped lithium niobate material for holographic read/write/erase memory applications.

5.1 Thick Phase Model Validation

In the previous contract[1] we wrote a computer program to indicate the performance of the holographic recording material. We classified the recording material as a thin material or a thick material. For each of the categories we further divided them into absorptive or phase type material. The classification for thin or thick materials is not based entirely on the physical thickness of the material, since the same material can be regarded as thick or thin depending on how it is used. The criterion for determining the thickness of the recording material is given by a parameter Q defined by Kogelnik[15] as

$$Q = 2\pi\lambda d/n_o\Lambda^2$$

where λ is the wavelength of the laser beam, d is the physical thickness of the material, n_o is the refractive index of the material, and Λ is the spacing between the fringes recorded on the hologram. According to Kogelnik, a hologram recorded on a recording

material is a thick hologram only when Q is larger than 10. For example, the physical thickness of Kodak 649F emulsion is $16\mu m$. If a hologram is recorded with a $1\mu m$ fringe spacing using an He-Ne laser, the parameter Q is approximately 40. Therefore, the hologram recorded on a $16\mu m$ emulsion under these conditions is actually a thick holo-gram. On the other hand, if the fringe spacing Λ is $2.5\mu m$, the hologram will be a thin one. This indicates that we can carry out the experimental study of thin and thick holograms using the same type of recording material, as long as we choose the fringe spacing Λ properly.

In the previous contract, we performed a series of experiments on the Kodak 649F emulsion, using it both as an absorptive and as a phase recording material. When it is used as phase material we remove the silver in the emulsion and sensitize the relatin with ammonium dichromate according to a technique described by Chang.[16] After exposure and development, the resulting hologram has very little absorption; the information is carried as variations in the optical path length in the emulsion. The experimental results are then approximated by equations that form the basis for our film model. The film model is then put in a subroutine program called XFILM.

During this contract year we investigated the holographic response from thick phase recording materials. We are developing thick plastics that can be made sensitive to visible light in the blue-green region of the spectrum. Specific examples are poly-methylmethacrylate (PMM), cellulose acetate butyrate (CAB), and polyvinyl acetate (PVA). The best known sensitizer for these polymers is p-benzoquinone (PBQ) which provides excellent response from 450-520 nm. These photosensitized polymers have excellent optical properties and essentially no scattering. Hence, they represent a close approximation to ideal thick phase hologram recording media.

From the experimental result we find that the performance of the material investi-gated can also be predicted by the computer program we wrote for the last contract. The only difference is in the exposure sensitivity of the recording material. The exposure sensitivity of the experimental material is about a factor of 50 less sensitive than the

dichromated gelatin we used in the last contract. Because the material is still in the development stage, we feel that it is not worthwhile at this time to take into account of this thick phase material in our previous computer program.

If we are interested to find out the holographic response of this thick phase material at an exposure level of E_o, we must first convert the exposure into the equivalent exposure for the dichromated gelatin for which our computer program is written. Using the factor of 50 in the difference in exposure sensitivity between the two recording materials, the equivalent exposure for dichromated gelatin is equal to $E_o/50$. Hence, to find out the holographic response of this thick phase material at $E_o = .2J/cm^2$, we simply type in the equivalent exposure of $400\mu J/cm^2$ for the dichromated gelatin in our program. The following example will illustrate how the computer program can be used. The following statement is given to the computer.

    & INPUT W = .0005, FILM = 1.E6, K=1

    EX = 4000, REF = 30, ITYPE = 'PHASE', PFILM = :T.&

Note that EX times 50 is the time exposure for the thick phase material. The computer printout is

    FILM TYPE=PHASE

    DIFFRACTION EFFICIENCY=14.83 PERCENT

    SIGNAL TO NOISE RATIO=170.21

    EXPOSURE=4000.00 MICROJOULES/CM*CM

    REFERENCE TO SIGNAL BEAM RATIO=1.00

    PACKING DENSITY=0.10E+07 BITS/CM*CM

    WAVELENGTH=0.000500 MM

    CARRIER FREQUENCY=1.000.0000 LINES/MM

For the parameters used, the diffraction efficiency of the thick phase material at $E_o = .2J/cm^2$ is about 14.83 percent.

RADIATION
A DIVISION OF HARRIS INTERTYPE CORPORATION

5.2 Holographic Optical Elements

A number of lenslet arrays were constructed using holographic techniques in a preliminary effort to provide uniform, efficient illumination for the block data composer. Each element of the lenslet arrays was a holographic zone plate recorded on dichromated gelatin. Dichromated gelatin was selected for its good cosmetic quality and high diffraction efficiency capability. The recording parameters selected were a bending factor Q of 1 (plano-convex lens) together with a prescribed offset angle (θ) of 60 degrees. One lenslet array contained 25 elements in a 5 x 5 matrix. The lenslets were on 5.5 mm centers and had a focal length of 12.5 mm with a 5 mm diameter. A 20 x 20 array was constructed with each element on a 1.5 mm center and with a focal length of 3 mm and a diameter of 1.5 mm. Overall efficiency of the lenslet arrays was about 60 percent.

To fabricate the lenslet arrays we used the experimental setup shown in Figure 5-1. An argon laser beam was divided into two parts to form a typical holographic interferometer. The reference beam was expanded into a uniform, well-collimated plane wave while the signal beam was first collimated and then converged with a Baush and Lomb f/2 (100 mm) Super Baltar Lens to form an approximately ideal point source. The interference of reference and signal waves subsequently formed a zone plate when used to expose a dichromated gelatin plate. A limiting aperture fixed the size of each zone plate and prevented unwanted exposure in neighboring areas. The dichromated gelatin plate was transported between exposures an exact distance by means of indexed translation stages. To prevent back scatter and reflections due to air/glass index mismatch, a layer of optical black lacquer was painted on the glass substrate of the gelatin layer after dichromation.

The lenslet arrays were fabricated from gelatin layers sensitized with ammonium dichromate. The procedure used to prepare and process the dichromated gelatin is given in Table 5-1. Note that the gelatin layer is obtained by removing the silver salts from Kodak 649F spectroscopic emulsions. Considerable care must be exercised in both the preparation and processing of dichromated gelatin in order to obtain satisfactory
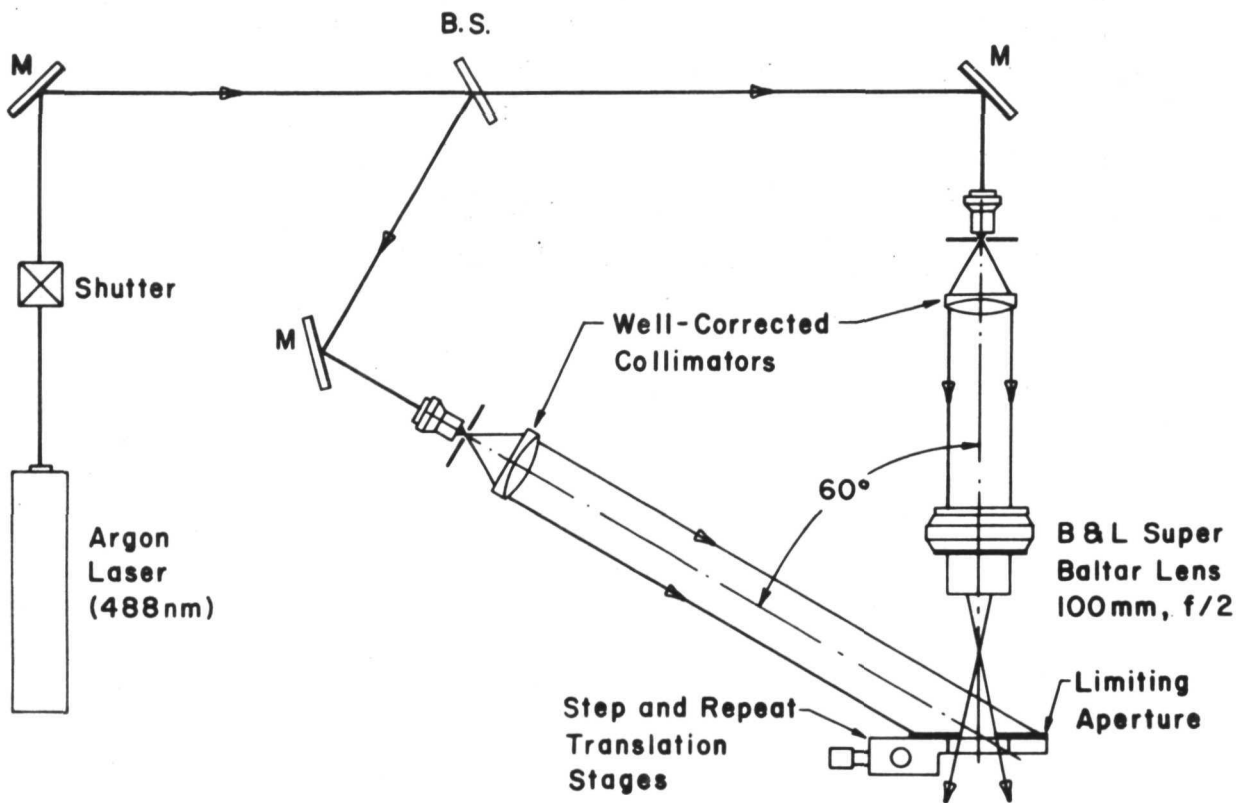
Figure 5-1. Experimental Setup

RADIATION

A DIVISION OF HARRIS INTERTYPE CORPORATION

TABLE 5-1.   DICHROMATED GELATIN PREPARATION AND PROCESSING

Preparation*

1.   Fix in Part A of Kodak Rapid Fixer - 10 minutes.

2.   Wash with running water at 90°F for 15 minutes.
     Start at 70°F and raise temperature at 2.5°F per minute to 90°F.

3.   Stand in air 1 minute.

4.   Rinse in distilled water with 2 drops per liter of Photo-Flo 600
     for 30 seconds.

5.   Dry completely in room environment.

6.   Soak in room temperature water for 2 minutes.

7.   Harden in both Part A and Part B of Rapid Fixer for 10 minutes.

8.   Wash for 15 minutes at 70°F in running water.

9.   Rinse in Photo-Flo solution for 30 seconds.

10. Dry overnight at room temperature.

11. Soak plates for 5 minutes in 5% ammonium dichromate solution with
     2 drops per liter of Photo-Flo 600.

12. Wipe ammonium dichromate off glass side of plates.

13. Dry at room temperature.

Processing

1.   Develop in a 0.5% solution of ammonium dichromate for 5 minutes.

2.   Bathe in Kodak Rapid Fixer for 5 minutes.

3.   Water rinse for 10 minutes.

4.   Soak in a 50/50 solution of water and isopropyl alcohol for 3 minutes.

5.   Soak in 100% isopropyl alcohol for 3 minutes.

6.   Free air dry.

* Start with Kodak 649F plates.

holograms. Primary advantages of the procedures outlined in Table 5-1 are consistency of results obtained for holographic reconstruction parameters and good cosmetic quality. An obvious disadvantage is the time required for preparation. After drying the processed gelatin layer at room temperature and humidity, it was protected from damage with a glass cover plate cemented in place with an optical lens bond.

Dichromated gelatin layers are volume phase media that exhibit a net increase in thickness after processing. Typically, there is a thickness increase in the order of 10 to 20 percent. The practical effect of the layer swelling is to generate Bragg angle mismatch and aberrations. The reason is that the swelling modifies the actual recording parameters due to fringe rotation. As a consequence, the average reference and signal beam angles appear changed, as does the recording wavelength. To compensate for this effect, the hologram must be repositioned to satisfy the apparent Bragg condition. This restores maximum diffraction efficiency, but creates significant aberrations over the reconstructed wavefront. In addition, the original construction geometry is not recovered, which in the present case is of primary importance.

The cause of the swelling is not well understood. A reasonable hypothesis is that the naturally hygroscopic gelatin entraps a small amount of water (highly polar substance) by means of vander Waal forces. The residual water is apparently in excess of that removed by the final alcohol rinse. Other unknown factors may also be involved.

Regardless of cause, it appears that post baking may provide a solution to this problem. This procedure is to record a zone plate at maximum efficiency, and then to reposition interferometrically. The zone plate is then rotated to determine the apparent Bragg angle. The angular rotation is a measure of the amount of layer swelling. The sample is then baked for a fixed time and the Bragg angle change is measured. By repeating this procedure a number of times, we expect to determine the amount of post baking required for a minimum layer swelling.

Further study of dichromated gelatin is recommended for a number of reasons. First, dichromated gelatin holograms can be nearly 100 percent efficient. Second, since there

RADIATION

A DIVISION OF HARRIS INTERTYPE CORPORATION

are no scattering centers and no absorption in the visible spectrum, dichromated gelatin holograms have low noise and excellent cosmetic quality. Finally, dichromated gelatin layers are relatively thin and, hence, angular orientation sensitivity is low enough to provide a reasonable working field. This is important, for example, when a laser beam must be directed over a small angular field to provide uniform BDC illumination of approximately constant irradiance. Although dichromated gelatin holograms are affected by extremes in relative humidity, this problem can be solved by protective overcoating techniques.

5.3 Battelle

Battelle's efforts to develop cis-trans material of doped lithium niobate as holographic materials were monitored during the program. Funding to Battelle by NASA-Langley ended and work on these materials was temporarily suspended at the end of 1972. The background, summary, and recommendations by Battelle are included here.

5.3.1 <u>Background</u>. - The present program is devoted to the development of materials suitable for use in high-speed, high-capacity holographic computer memories. Two classes of optical read/write/erase materials have been studied, cis-trans isomers and ferroelectrics. The rationale for this choice of materials was established under a previous study done by Battelle-Columbus Laboratories under subcontract to Radiation, under NASA Contract No. NAS8-26672 which was funded by NASA-MSFC. These studies were directed toward the identification of those classes of material which had the potential of being developed to the point of utility in the MSFC system. Due to the high-bit density required, multiple hologram recording was indicated. This, in turn, dictated the use of thick-phase holograms. The present work was carried out with an awareness of the MSFC requirements, although the MSFC system is not the sole motivation for advancing the state-of-the-art of optical memory materials.

5.3.2 <u>Summary</u>. - During the contract period, Battelle-Columbus has investigated the potential of certain cis-trans isomers and doped $LiNbO_3$ for the holographic read/write/erase memory application. The cis-trans work involved the photochemical investigation of a number of potential materials as well as specific molecular engineering efforts on α-methylstilbene and its derivatives. These efforts resulted in an increase in Δn, and, thereby, in potential recording utility, of an order of magnitude.

The work on $LiNbO_3$ was directed toward a preliminary investigation of the dynamics of the writing process. Several samples and a variety of writing conditions were investigated. An unexpected and as yet unexplained improvement in material behavior with continued recycling was observed. In addition, some effort was devoted to an analysis of the physical conditions under which several current theories of the "optical damage" process are valid.

5.3.3 <u>Recommendations</u>. - The research on the use of cis-trans isomers of stilbene during the past 12 months has indicated that such a system may prove ideal for high-speed, high-capacity holographic memories. The substantial progress achieved, in spite of the fact that some significant technical details have not as yet been investigated, suggest that the proposed system requirements can be met. During this program an order of magnitude improvement in sensitivity has been realized, so that useful sensitivities are being approached. Thus, we recommend that in light of these advances research with cis-trans isomers be continued at Battelle-Columbus.

In the realm of inorganic, erasable phase materials, $LiNbO_3$ is clearly the most promising compound. However, several problems still exist, most notably its lack of sensitivity. Continued work should be done on the ferroelectrics to better understand the writing mechanism and to develop materials with characteristics tailored for specific applications.

REFERENCES

1. "Optical Read/Write Memory System Design, Final Report," Prepared under Contract No. NAS 8-26360 by Radiation (February 1971).

2. H. H. Hopkins and V. V. Rao, Optica Acta, 17, 497 (1970).

3. "Updated Optical Read/Write Memory System Components, Second Quarterly Report," Prepared under Contract No. NAS 8-26672 by Radiation (September 1972).

4. "Updated Optical Read/Write Memory System Components, First Quarterly Report," Prepared Under Contract NAS 8-26672 by Radiation (June 1971).

5. "Optical Read/Write Memory System Components, Final Report," Prepared under Contract No. NAS 8-26672 by Radiation (February 1972).

6. G. H. Haertling and C. E. Land, J. Am. Cer. Soc., 54, 1-11 (1971).

7. C. E. Land and P. D. Thatcher, Proc. IEEE, 57, 751-768 (1969).

8. J. R. Maldonado and A. H. Meitzler, IEEE Trans. on Elec. Devices, ED-17, 148,156 (1970).

9. P. D. Thatcher and C. E. Land, Paper 31/2 presented at the 1971 Western Electronic Show and Convention, August 24-27, 1971.

10. H. N. Roberts, Appl. Optics, 11, 397-404 (1972).

11. J. R. Maldonado and A. H. Meitzler, Proc. IEEE, 59, 368-382 (1971).

12. W. D. Smith and C. E. Land, Appl. Phys. Lett., 20, 169-171 (1972).

13. N. Uchida and T. Ikeda, Jap. J. Appl. Phys., 6, 1079-1088 (1967).

14. W. D. Gill, "Drift Mobilities in Amorphous Charge-Transfer Complexes of Trinitrofluorenone and Poly-n-vinylcarbazole," J. Appl. Phys., 43, 5033 (1972).

15. H. Kogelnik, "Coupled Wave Theory for Thick Hologram Gratings," B.S.T.J. 48, 2909 (1969).

16. M. Chang, "Dichromated Gelatin of Improved Optical Quality," Appl. Opt. 10, 2550 (1970).

APPENDIX A

ANALYSIS OF SCATTERING MODE PLZT BDC

A consideration of contrast ratios achievable with the scattering mode under various system constraints is presented in this section.

Assume that scattered light from an elemental region of the PLZT (from a small $d \times d = d^2$) has a power distribution in watts/steradian given by,

$$P(\theta) = P_o \cos^m \theta \tag{A-1}$$

where m is the integer and P_o is obtained from normalizing conditions. Suppose the PLZT device is illuminated by a wave of intensity U in watt/mm^2 so that an amount of power Ud^2 is incident on the element under consideration. Refer to Figure A-1. Neglect reflection and absorption losses for this simplified analysis. The power incident on the element must therefore equal the total power in the scattered region to the right of the element. For the two dimensions (x and y) transverse to the optical axis, we must use solid angles to account for all of the scattered light power. However, circular symmetry about z is assumed. We can therefore write,

$$Ud^2 = \int P(\theta) \, d\Omega$$

hemisphere to the right

$$= \int_0^{\pi/2} (P_o \cos^m \theta)(2\pi \sin \theta \, d\theta)$$

$$Ud^2 = \frac{2\pi P_o}{m+1} \tag{A-2}$$

The normalizing condition is expressed in Equation (A-2) for the constant P_o in Equation (A-1). We assume $d \ll f$, $d \ll D$, $a \ll f$. The angle θ_a is defined by,

RADIATION
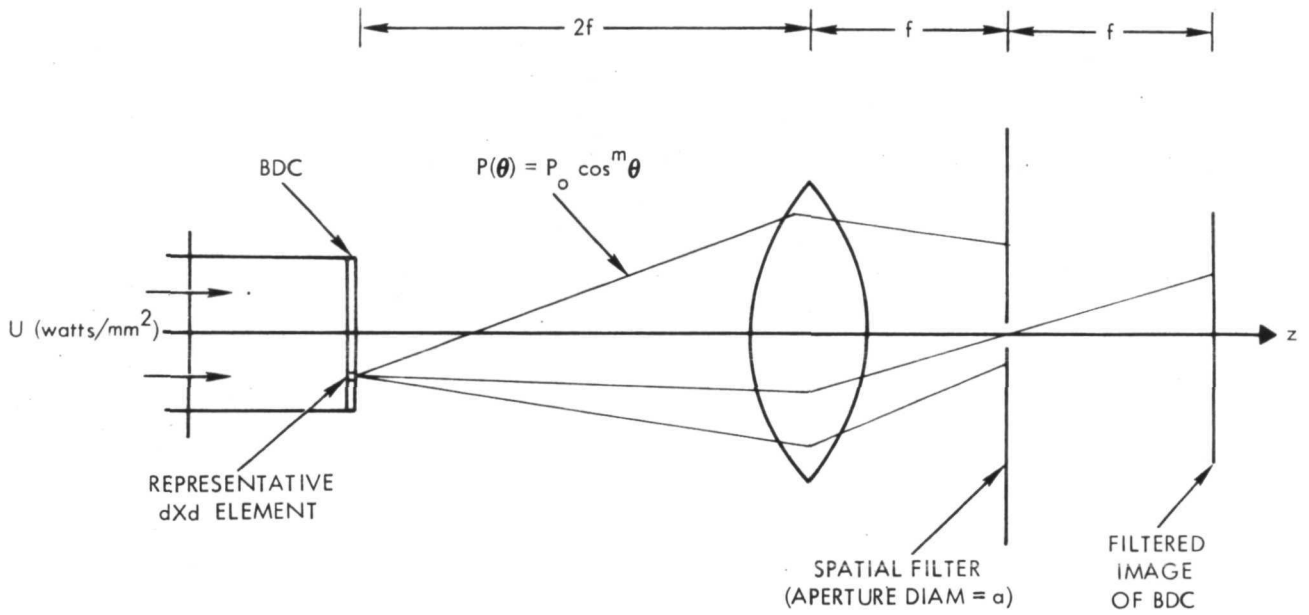A DIVISION OF HARRIS · INTERTYPE CORPORATION

Figure A-1.   Spatial Filtering Arrangement for BDC With Scattering
Mode PLZT

$$\tan \theta_a = \frac{a/2}{f}$$

$$\tan \theta_a \approx \theta_a,$$

and is the angular aperture of the physical aperture of diameter a in the back focal plane of of the lens. The power transmitted through the aperture from the d x d element for a scattering profile $P(\theta)$ from the element is,

$$\bar{P}_a = \int_0^{\theta_a} (P_o \cos^m \theta)(2\pi \sin \theta \, d\theta)$$

$$\bar{P}_a = \frac{2\pi P_o}{m+1} (1 - \cos^{m+1} \theta_a). \tag{A-3}$$

The power transmitted in the absence of scattering is simply,

$$\bar{P}_o = Ud^2 = \frac{2\pi P_o}{m+1}, \tag{A-4}$$

assuming that $a > f\lambda/d$ (so that the main lobe of the power spectrum of the d x d element is transmitted). The contrast between these two states is,

$$R = \frac{\bar{P}_o}{\bar{P}_a} = \frac{1}{1 - \cos^{m+1} \theta_a} \tag{A-5}$$

For $\theta_a \ll 1$ and $m/2 \, \theta_a^2 \ll 1$ we can write

$$1 - \cos^{m+1} \theta_a \approx \frac{m+1}{2} \theta_a^2 \tag{A-6}$$

and get

$$R \approx \frac{2}{m+1} \left(\frac{1}{\theta_a^2}\right) = \frac{8}{m+1} \left(\frac{f}{a}\right)^2 \tag{A-7}$$

Taking $a = cf\lambda/d$ and $c \geq 1$, we can get,

$$R \approx \frac{8}{m+1} \left(\frac{d}{c\lambda}\right)^2. \tag{A-8}$$

In the experiment to measure contrast described by Smith and Land of Sandia, they used $\theta_a = 2^\circ = 0.035$ radians and obtained $R \approx 500$ at polarization saturation. These values in Equation (A-7) indicate that $m \approx 12$.

It may be unreasonable to assume no scattering in the ON state. A more realistic relationship for contrast might be,

$$R' = \frac{1 - \cos^{n+1} \theta_a}{1 - \cos^{m+1} \theta_a}. \tag{A-9}$$

where a large value of $n + 1$ applies to low residual ON state scattering levels. It is clear that a low value for m and a high value for n are desired.

For the holographic memory system, a spatial filtering state will be required. The lens array for signal beam spreading may have to be placed in an image plane of the BDC (after spatial filtering). If signal beam deflection is used, the spatial filtering aperture size will have to be increased to pass deflected unscattered light; the contrast will be correspondingly reduced. The system configuration and the important tradeoffs would be significantly affected with the scattering mode.